Contributions to Geophysics and Geodesy Vol. 50/1, 2020 (1–32)

Edge detection, depth estimation and 3D-inverse modelling of the Red Sea and Zagros gravity anomalies using the gravity data extracted from EGM2008 Geo-potential Model

Ali AMJADI[1], Bahram AKASHE[1,*], Mohammad ARIAMANESH[2], Mohsen POURKERMANI[3]

[1] Department of Geophysics, North Tehran Branch, Islamic Azad University, Tehran, Iran; e-mail: amjadi.gp@gmail.com, akashebahram@gmail.com

[2] Department of Geology, Payam Noor University, Tehran, Iran; e-mail: aryamanesh.geo@gmail.com

[3] Department of Geology, North Tehran Branch, Islamic Azad University, Tehran, Iran; e-mail: Mohsen.Pourkermani@gmail.com

Abstract: Using geophysical methods and measuring physical properties of subsurface rocks are good solutions for investigating the subsurface structures and exploring underground buried resources (such as oil, gas, water, minerals, etc.). This research investigates the anomaly sources of Zagros and the Red Sea by using the derivative filters, regularized filters, analytic signal, local-phase filter, 3D-inverse modelling with the Li-Oldenburg method. For this purpose, these filters are first applied to artificial models to determine the capability of each of these filters, a comparison also will be made between edge detection filters and finally applied to the real gravity of Zagros and Red Sea regions (taken from the EGM2008 Global Model). The overall result is that the effective depth of the sources of gravity anomalies of the Red Sea is approximately 200 km, and incoherently, up to a depth of 300 km. The effective depth of the Zagros anomalies sources is also about 180 km and since then it has continued inconsistently up to 400 km.

Key words: gravimetry, Li-Oldenburg inverse modelling, edge detection, analytic signal, local-phase filters, 3-D modelling

1. Introduction

The convergence of Arabian Plate and Central Iranian micro-continent is

*corresponding author: e-mail: akashebahram@gmail.com

accompanied by numerous folding and fault systems and tectonic features created an index which is named Zagros fold- thrust belt. South East and West border of Arabian plate with Africa is the oceanic divergent boundary covered by the Gulf of Aden and the Red Sea, respectively.

Changes caused by various anomalies of the Earth's crust can lead to the formation of linear structures at the Earth's surface called the lineaments. Understanding these anomalies is used as an important factor in studying the tectonic status of each region. Some of these anomalies are buried by younger sediments and cannot be traced back to the surface; in this case geophysical methods can be used to identify hidden structures. One of these methods is the use of gravity data (*Ariamanesh and Mahmoudpour, 2012*).

Today, the effort to identify the buried structures and access to the subsurface resources has expanded widely, and geophysics is one of the tools to identify these structures. Using geophysical methods and measuring the physical properties of subsurface rocks are good solutions for investigating subsurface structures and exploring buried underground resources (such as oil, gas, water, minerals, etc.). To achieve this goal, using different edge and depth estimation filters, 2D and 3D modelling, are the most successful methods of interpreting geophysical data, which the result is a better understanding of subsurface structures such as source shape, amount of the depth, surface extent, deep stretching, etc. Determining these parameters has a direct and significant impact on future decisions, which can be effective in cost management. This research investigates the gravity anomaly sources of Zagros and the Red Sea by using the derivative filters, analytic signal, local-phase filter, 3D-inverse modelling with the Li-Oldenburg method.

There are two main purposes in this inversion method: in the first approach, the purpose of inversion is to determine the source geometry, and in the second approach, the purpose is to detect the density contrast of the mass in question with the surrounding environment. This method includes a multi-component objective function that is flexible enough to produce a variety of models and can be corrected for models that do not conform to geological structures. For this purpose, these filters are first applied to artificial models to determine the capability of each of these filters and finally applied to the real Zagros and Red Sea gravity data (taken from the EGM2008 Global Model).

2. Geologic and tectonic setting of the Zagros

The Zagros mountain belt results from the closure of the Neotethys oceanic domain and the collision of the northern margin of the Arabian platform with the microplates of central Iran, accreted to the southern margin of Eurasia during the Mesozoic (e.g. *Besse et al., 1998*). The Zagros orogenic belt is bounded to the northwest by the East Anatolian left-lateral strike-slip fault (EAF) and to the southeast by the Oman Line (OL) (*Falcon, 1969*), which is here considered to be a transform fault inherited from the opening of Neo-Tethys (*Alavi, 1994*).

The fold and thrust belt on the Arabian Plate is a result of deformation of the Zagros Orogenic Belt (ZOB) passive margin sediments that have been caused by continental collision (*Alavi, 1994; Ghasemi and Talbot, 2006; Horton et al., 2008; Allahyari et al., 2010; Saccani et al., 2013*).

The Zagros were traditionally classified by distinctive lithological units and structural styles into four NW trending tectonometamorphic and magmatic belts (Fig. 1). These are bounded by defects on a regional scale such as the Main Zagros Thrust (MZT), High Zagros Fault (HZF) and Mountain Front Fault (MFF) (*Del Chiaro et al., 2019; Agard et al., 2005* and references therein). The presence of negative isostatic anomaly near the Zagros main thrust (*Synder and Barazangi, 1986*) and seismic evidence with focal depths greater than 50 km in the ISC and USGS prove subduction of the Arabian plate beneath central Iran (*Nowroozi, 1971*).

Berberian (1995) described tectonic developments of this region as a platform phase in the Paleozoic, rifting in the Permian and Triassic, forming inactive continental margins (with seafloor spreading to the north-east) in the Jurassic and Early Cretaceous, subduction to the northeast and ophiolite and radiolite deposition in the late Cretaceous, and finally the continental-continental collision and shortening during the Neogene.

Today, their effects appear on or near the surface of the Earth as thrust faults. It can be said that the Zagros basement is about 25 to 50 km thickness (*Gies et al., 1984*).

Based on *Dehghani and Makris (1984)*, under the main Zagros fault (high Zagros), gravity anomalies reach to a minimum (−230 mgal), and in this area, the Iranian crust thickness 50 to 55 km has the highest thickness, which is attributed to the compressive process associated with the opening of the Red Sea.

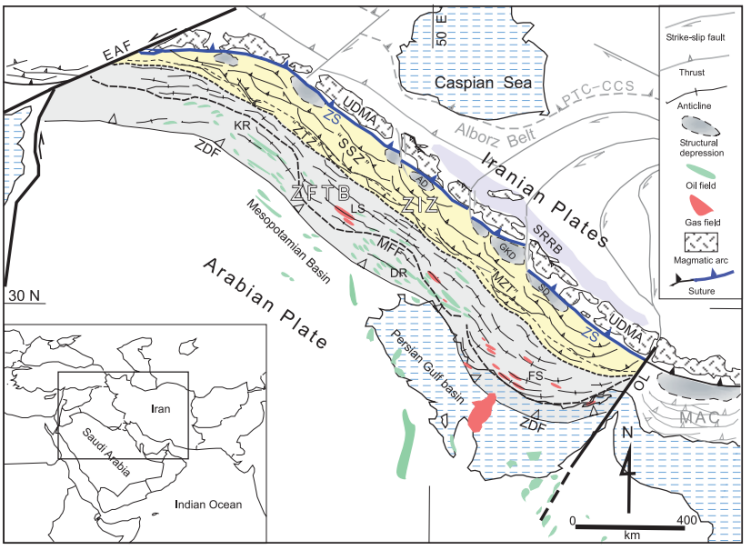

Fig. 1. Subdivisions of the Zagros orogenic belt. Abbreviations: AD – Arak depression; DR – Dezful recess; EAF – East Anatolian Fault; FS – Fars salient; GKD – Gav Khooni depression; KR – Karkuk recess; LS – Lorestan salient; MAC – Makran accretionary complex; MFF – "Mountain front flexure"; "MZT"– "Main Zagros Thrust"; OL – Oman Line; PTC-CCS – Paleo-Tethyan continent-continent collisional suture; SD – Sirjan depression; SRRB – Saveh-Rafsanjan retroforeland basin; "SSZ" – Sanandaj-Sirjan zone; "ZTZ" – Zagros thrust zone; UDMA – Urumieh–Dokhtar magmatic assemblage; ZDF – Zagros deformational front; ZFTB – Zagros fold-thrust belt; ZIZ – Zagros imbricate zone; ZS – Zagros suture. Hydrocarbon fields of the region, oil in green and gas in red, are shown (*Alavi, 2007*).

3. Geologic and Tectonic setting of the Red Sea

The Red Sea, an enclosed body of water that lies between 30° N and 12° 30′ N, is about 1,932 km long and 280 km in width (*Morcos, 1970*). The narrow southern Strait of Bab-al- Mandab (29 km in width) is the boundary between the Red Sea and the Gulf of Aden. The Red Sea is one of the youngest oceanic zones on earth and was created by slow seafloor spreading. Together with the Gulf of Aqaba-Dead Sea transform fault, it forms the western boundary of the Arabian plate, which is moving in a north-easterly direction. The plate is bounded by the Bitlis Suture and the Zagros fold belt and subduction zone to the north and north-east, and the Gulf of Aden

spreading centre and Owen Fracture Zone to the south and southeast (*Rasul and Stewart, 2015*) (Fig. 2 modified after *Stern and Johnson, 2010*).

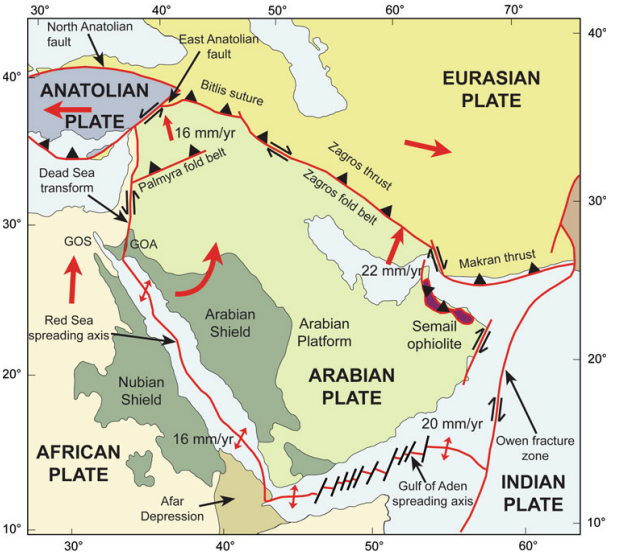

Fig. 2. Main tectonic features of the Arabian Peninsula and surrounding areas (modified after *Stern and Johnson, 2010*).

According to *Swartz and Arden (1960)*, with the onset of Pliocene, marine sediments were deposited in the Red Sea due to the influx of water from the Indian Ocean into the Red Sea, meanwhile due to the uplift of the Suez Canal, the connection between the Mediterranean Sea and the Red Sea has been severed. The Red Sea Rift System is one of the world's largest active rift systems, which comprises a variety of rifting stages starting from initial faulting and advancing through several stages of continental rifting. It began about 30 million years ago, separating the western edge of the Arabian Plate from Africa (*Camp and Roobol, 1992*).

Sultan et al. (1993) have indicated that the Arabian and Nubian sections of the shield have remained as rigid plates during the Red Sea rifting, and the site of the present Red Sea has probably a zone of structural weakness in the late Precambrian, with the breakup and rifting controlled by pre-existing fault systems (*Makris and Rihm 1991; Bosworth et al., 2005*). A bathymetric and topographic map prepared from various sources is presented in Fig. 3 The sea is connected to the Arabian Sea and Indian Ocean via the

Gulf of Aden in the south through the narrow Strait of Bab-al-Mandab, which has a minimum with of only 30 km, where the main channel is about 310 m deep and 25 km wide at Perim Island (*Morcos, 1970*).

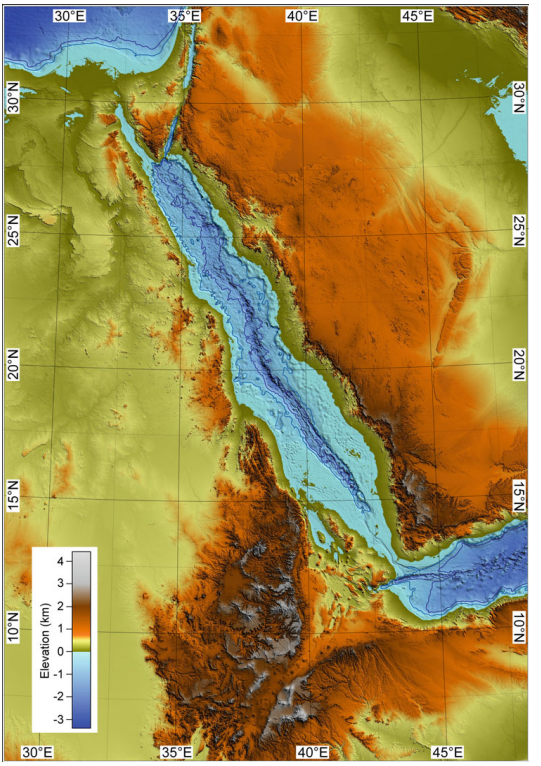

Fig. 3. Topography and bathymetric map. Bathymetric contours are at 500 m interval (Courtesy Marco Ligi).

The Red Sea has been opening since the Arabian plate broke away from the African plate about 24 million years ago (*Bosworth et al., 2005*). The rifting began with continental stretching and thinning and later progressed to sea-floor spreading. The rate of opening increases from about 7 mm/year in the northern Red Sea to roughly 16 mm/year in the south (*ArRajehi et al., 2010; Reilinger et al., 2015*). The present velocity of Arabia with respect to Eurasia increases from west to east along the Persian Gulf from 18 to 25 mm yr^{-1}, oriented about N10° E (*Madahizadeh et al., 2016; Sella et al., 2002, Walpersdorf et al., 2006*).

4. Research methods

4.1. The basics of the gravity method and the filters used in this research

Gravity surveying may be conducted on many scales, e.g., small scale prospecting, regional marine surveys and global satellite surveys (*Foulger and Peirce, 2007*). The fundamental equation used for mathematical treatment of the data and results is Newton's Law of Gravitation:

$$F = G\,\frac{m_1 m_2}{r^2}\,, \tag{1}$$

where F = force, m_1, m_2 = mass, r = separation distance, G is the gravitational constant ($6.67 \times 10^{-11}\,\mathrm{m^3 kg^{-1} s^{-2}}$).

The unit of measuring the acceleration of gravity is Gal ($1\ \mathrm{gal} = 1\ \mathrm{cm\ s^2}$). But in practice, a smaller unit called milligal is usually used. Acceleration of gravity is not exactly the same everywhere, but is controlled by several factors such as latitude, elevation, mass, topography, and ultimately geology of the area. Therefore, in order to obtain geological information, corrections such as free-air correction, Bouger, latitude and topography must be applied to the measured initial values. Gravity studies are used extensively in the investigation of large- and medium-scale geological structures (*Paterson and Reeves, 1985*).

4.2. Separation of regional and residual anomalies

Potential field data map (gravity and magnetic field) is the sum of the effects of sources with different density and magnetism at different depths which in other words, the result of survey is related to all anomalies in the region. In these maps, the effects of bedrock are characterized by mild and linear changes (*Doulati Ardejani, 2011*) which are called regional anomalies, and more surface anomalies are called regional or residual anomalies. Regional anomalies have low frequency and long wavelength, while, residual anomalies have high frequency and short wavelength.

In gravimetric studies, in order to clarify more surface anomalies such as mines and faults, the effect of regional anomalies such as bedrock should be excluded from the data (*Kolagari, 1992*).

4.2.1. Surface Trend Remove filter

One of the most flexible analytical techniques for determining the surface structures is the surface trend method (*Hinze, 1990*). In this method, the area field from observed values is approximated by the least squares method. This method is based on surface computation by mathematical method that best matches relate to the observed values (*Agah et al., 2004*).

4.2.2. Edge Estimation Filters

Potential field data has unique advantages in investigating lateral heterogeneity of geological masses, especially their edge position. When it comes to geological edge or boundaries, it mainly refers to the boundaries of faults, fractures, geological units, or rock units of varying density (*Hadadian, 2011*). Filtering the potential field data is a numerical processing that plays an important role in the modification and interpretation of magnetic and gravity data. Image processing can be mapped from image space to information space, which prepares the image for future analysis. This is done with a variety of filters, the main advantage of them is not the need to transfer data from one domain to another. Different types of filters specify distinct features (*Danaei et al., 2011*). Below we will review the most important Edge Detection filters.

4.2.2.1. Derivative filters

Derivative filters are one of the most widely used filters in interpreting potential field data and their role is to separate the residual anomalies from the regional ones and detect the edge. These filters include vertical derivative, total horizontal and directional filters (*Verduzco et al., 2004*). Vertical derivative magnitude at the edge place of the subsurface masses is zero and at the source is positive, and the horizontal derivative magnitude at the top of the subsurface mass edges is maximum and at the source is zero which this feature is used to detect the edge. Vertical derivative filter shows more obvious the edge and anomalies with increasing derivative order, but as it falls into the category of high pass filters, the available noise along with the surface anomalies are highlighted in the maps. For this reason, first and second order derivatives are more commonly used. As a solution of this noise

damping is an adapted low-pass filtering of the computed derivatives – e.g. by means of the concept of Tikhonov regularization (*Pašteka et al., 2009*). As mentioned, since the horizontal derivative is maximal at the up of the edge of the subsurface masses, it is more applicable to gravity data and it is less used in magnetic data because of the dipole nature of the anomalies.

4.2.2.2. Analytical signal filter

The analytical signal or full gradient is defined as the combination of horizontal and vertical derivatives of the potential field data. The maximum amount of analytical signal is placed on the edges of the mass. One of the points of the method is that the horizontal and vertical derivatives of a potential function are Hilbert transforms of each other. The Hilbert transform does not change the amplitude of the input function but changes its phase to 90 degrees. Consequently, Hilbert transforms of the horizontal derivative of the potential field data presents the vertical derivative of the data (*Nabighian, 1972*).

4.2.2.3. Local-phase filter

4.2.2.3.1. Tilt Angle filter

Tilt Angle filter is one of the local phase filters which is based on the ratio of the gravity field derivatives and examines the phase (angular) variations of the potential field derivatives. This filter is effective in balancing the amplitude of deep anomalies to surface anomalies and is not sensitive to the depth. In other words, tilt angle filter separates deep and shallow sources equally (*Miller and Singh, 1994*). Since the tilt angle filter has a direct relation with the vertical and a verse relation with the horizontal derivative, so at the edge of the anomaly, the tilt angle value is zero (*Cooper and Cowan, 2006*).

4.2.2.3.2. Hyperbolic Tilt Angle Filter

If the actual part of the hyperbolic tangent function is used instead of the tangent function in the calculation of the tilt angle, the edge of the

subsurface masses will be more extremely prominent. The minimum value of this filter will be located just above the edge of the mass. One of the most important advantages of this filter is it's insensitivity to existing noise (*Cooper and Cowan, 2006*).

4.2.2.4. Regularized Derivative Filter

Since vertical derivative filters are high pass filters, noises filed will be sharper. One way to stabilize higher derivative evaluation is the utilization of the Tikhonov regularization (*Pašteka et al., 2009*). In this method, regularized derivative filter minimized or optimized with the usage of classical calculations in the Fourier domain and optimum regularization coefficient calculated from C-norm function (*Pašteka et al., 2009*). Now figures of regularized derivative are presented.

4.3.1. Upward Continuation Filter

Upward continuation method of potential field data is widely used in geophysics. For example, this method is used to enhance and reveal deeper resource responses in places where shallow resources are also available. In this method, the potential field data from a datum level is mathematically imaged on the level surfaces above the main datum level. Thus, effects of the removed surface tracks and the effects of deep structures are clearly identified. In fact, with this method, anomalies with shorter wavelength removed and thus it reduces noise, and acts similar to a low-pass filter (*Reynolds, 1977*).

4.3.2. An introduction to Modelling

After performing geophysical measurements, correction, data processing, and separation of local anomalies from area anomalies, the important stage is interpretation. All geological, geophysical and other related data must be used in the interpretation process to obtain the best possible interpretation. The methods of geophysical data interpretation can be divided into three main groups, each approaching the purpose with logical but different processes:

4.3.2.1. Enhancing and data depiction

In this method, none of the model parameters are calculated, but the anomaly is processed and depicted in a way that makes some of the features of the source more salient and the overall interpretation easier. All of these methods can be used as complementary tools in modelling (*Blakely, 1996*). For example, a variety of edge detection methods fall into this category of interpretation of geophysical data.

4.3.2.2. Forward modelling

In the Forward modelling, based on existing geological observations or geophysical studies, an initial model for the anomaly is considered, the gravity effect of this model is calculated and compared with the observed gravity anomaly. In case of insufficient fitness, the interpreter modifies the parameters of the model so as to obtain the best fit between the effect of model gravity and the observed gravity anomaly. In fact, in this method, the characteristics of the model are determined by trial and error method (*Ebrahimzadeh Ardestani, 2010*).

4.3.2.3. Inverse modelling

In this method, the characteristics of anomaly source are calculated automatically or semi-automatically and using observed data. One of the most advanced methods of 3D inverse modelling is Li- Oldenburg's theory developed at British Colombia University in Canada and they used it as the basis of Grav3D software (*Jafarzadeh, 2015*). The main mathematical explanation of this theory is beyond the scope of this paper and for further reading, you can refer to more useful references (*Williams, 2008; Philips, 2001; Li and Oldenburg, 1998*).

4.4. Artificial data

To optimally use and apply a method, filter or algorithm and analyze the results in various geophysical methods, first, its application to artificial data with noise is examined. This method is used to check real data in an area,

based on the degree of concordance with the main response (*Jafarzadeh, 2015*).

In this section, to investigate the performance of different filters such as edge detection and inversion by Li-Oldenburg method in reconstructing multiple anomalies and with different depths, an artificial model consisting of two rectangular cubes in the north-west and south-east, with 15 up and 40 down m depth, and a rectangular cube in the northeast with 25 up and 50 down m depth is used which the density contrast of cubes with the surrounding environment is $2\,g/cm^3$. This artificial model was built using 216,000 cells of equal width and length of 5 metres and elevation of 2.5 metres (Fig. 4). For inversion, the gravity effect of these bodies was calculated on a regular square grid at 5 m intervals, yielding 3600 data points. To make the data appear realistic, Gaussian noise was added to the data by 2% (*Jafarzadeh, 2015*).

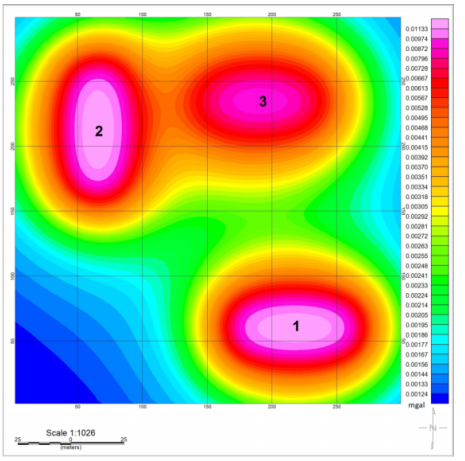

Fig. 4. Residual anomaly map derived from artificial model.

The results of applying the edge detection filters are presented below. All the numerical derivatives, entering into these derivative filters where calculated by means of the concept of regularized derivatives (*Pašteka et al., 2009*).

As can be seen in Figs. 8 and 6, the stretching of the anomalies is greater than in Fig. 4 and closer to the original form. Also in Fig. 7 that shows the horizontal derivative filter (the forming angle with the positive side of the

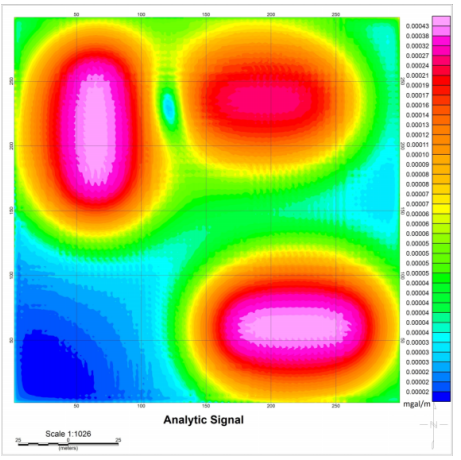

Fig. 5. Analytical signal filter.

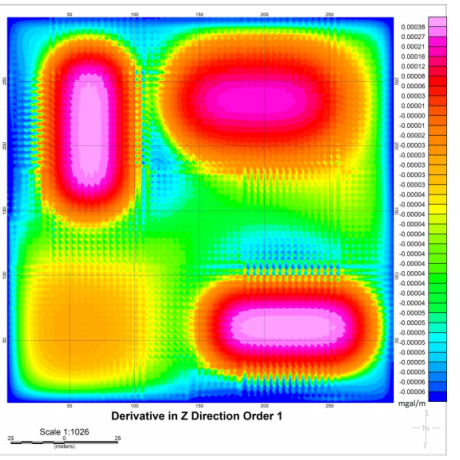

Fig. 6. Vertical derivative filter.

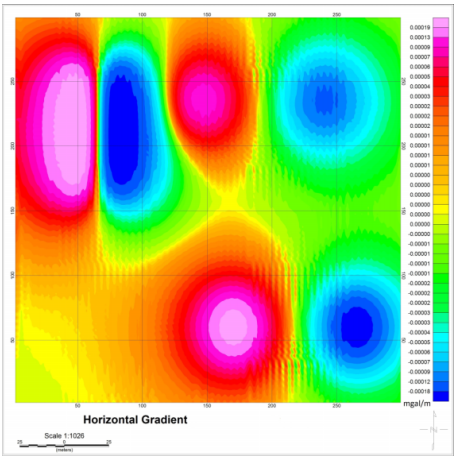

Fig. 7. Horizontal derivative filter.

X axis is zero), the anomalies stretch along the Y axis and receive a dipole character. It is important to note that in this filter, if the dipoles are closer to each other and stretch in a particular direction (not symmetrical), the main anomaly stretches in the same particular direction, but if the dipoles are symmetric and not close together, they stretch perpendicular to the angle with the X-axis. Figs. 8 and 9, which represent the tilt angles and the hyperbolic tilt angles, respectively, are well able to detect the edge of the

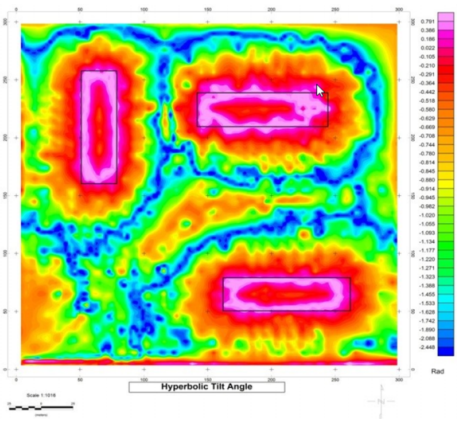

Fig. 8. Hyperbolic tilt angle filter.

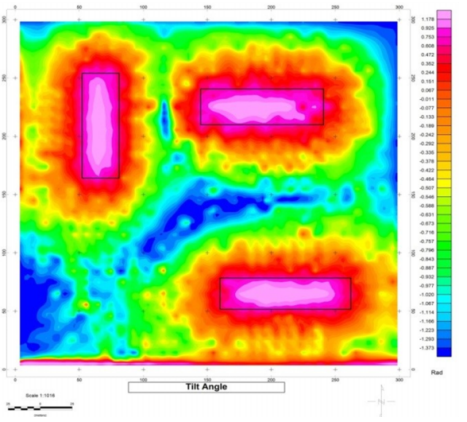

Fig. 9. Tilt angle filter.

anomalies. Now figures of regularized derivative are presented.

In the following, the validity of Li-Oldenburg 3-D inversion modelling method on artificial data is discussed. One of the advantages of this modelling method is that it is possible to include a variety of complementary area information (such as geological information, drilling, etc.) into the modelling so that the final model obtained is as close to reality as possible. Fig. 13 is a 3D view of the artificial model used, and Figs. 14 and 15 are im-

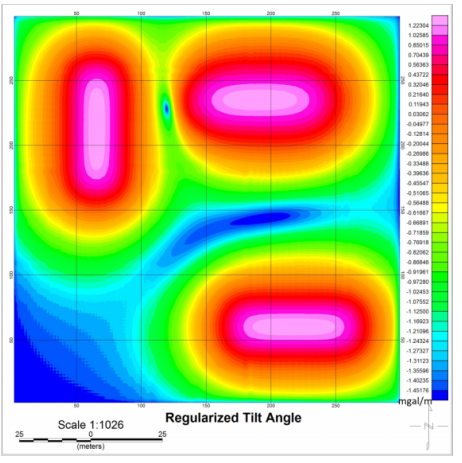

Fig. 10. Regularized tilt angle filter.

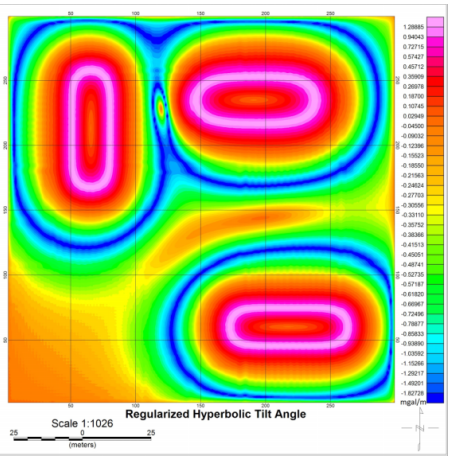

Fig. 11. Regularized hyperbolic tilt angle.

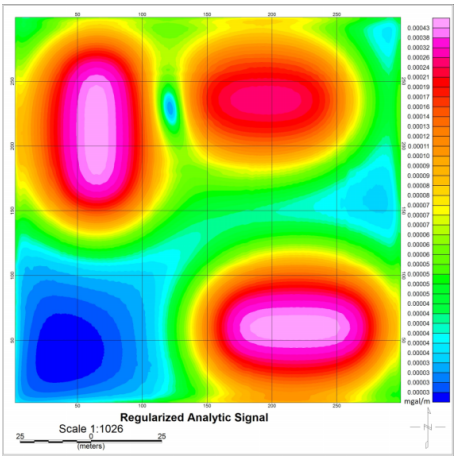

Fig. 12. Regularized analytical signal filter.

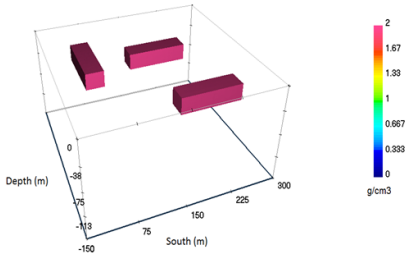

Fig. 13. 3D view of the compound artificial model.

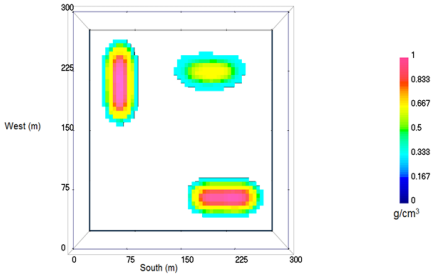

Fig. 14. Top view of artificial model inversion.

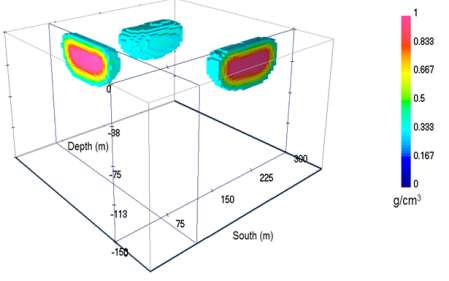

Fig. 15. Another view of artificial model inversion.

ages of the 3-D inversion that provide acceptable agreement with the original artificial model. Comparing figures of regularized derivative (Figs. 10–12) and simple mode of them, it is clear that regularized derivative mode has a much better performance and their noise significantly reduced.

4.5. Real data

4.5.1. Edge Detection of Zagros and the Red Sea Anomaly

The gravimetry data output (complete Bouger anomaly) obtained from the EGM2008 satellite for the Zagros and Red Sea regions is as follows (Figs. 16 and 17):

As can be seen from the above figures, the trend dominating these two regions is the lineaments in the form of maximum and minimum anomalies together from northwest to southeast. As previously described, gravimetric data maps are the result of regional and residual anomalies. To investigate and highlight the surface structures, we remove the effects of the regional anomalies whose results are shown in Figs. 18 and 19, using the Trend Remove filter. It is noteworthy that this filter and future filters were implemented in the Oasis Montaj software environment owned by Geosoft Company. Comparing Figs. 16 with 18 and 17 with 19, we find that the intense of the anomalies are increased, such as the central anomaly of Fig. 18 and the end of it in Fig. 19 (southeast) became more salient.

The complete Bouger maps or the surface trend remove map cannot be used properly to detect the edge or boundary of Zagros or the Red Sea anomalies. Edge detection filters are used to do this. All of these filters are applied on the complete trend removed Bouger map. Also here, we have used the computed numerical derivatives by means of the Tikhonov concept of regularization (*Pašteka et al., 2009*). It is important to note that the reason for applying several edge detection filters is to get the result closer to reality.

4.5.2. Edge detection of Zagros anomalies

Figs. 20, 21 and 22 are the maps obtained by applying Horizontal Gradient, Analytical Signal, and Derivative in Z direction Order 1 filters, respectively, to Zagros data. As is clear from the figures below, the boundaries of the

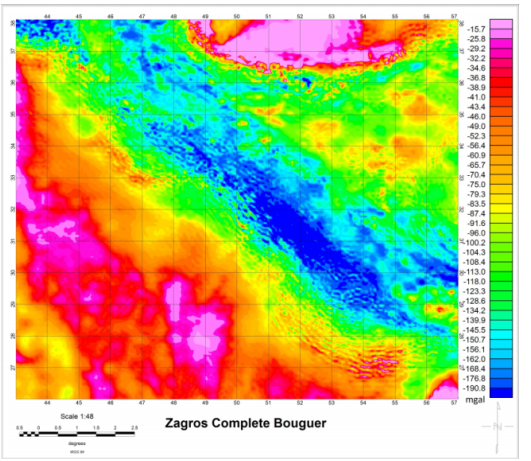

Fig. 16. Complete Bouguer anomaly map of the Zagros.

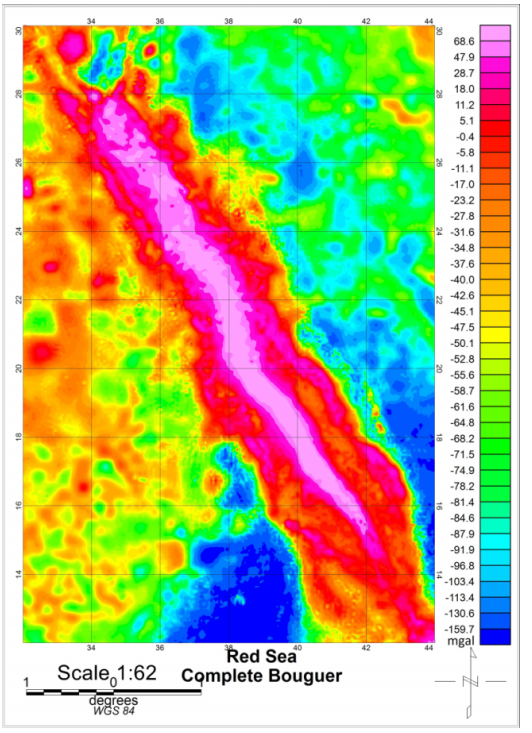

Fig. 17. Complete Bouguer anomaly map of the Red Sea.

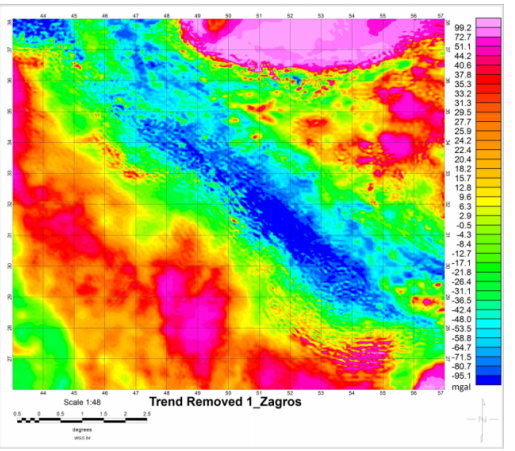

Fig. 18. Removing the first-order trend map of the Zagros.

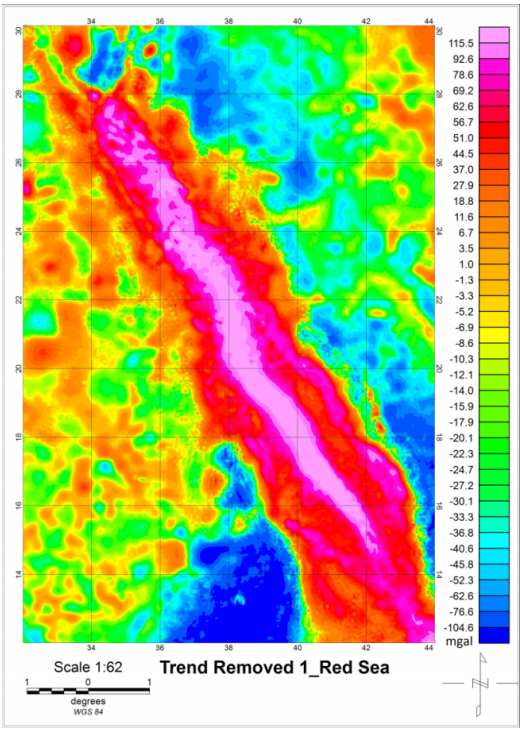

Fig. 19. Removing the first-order trend map of the Red Sea.

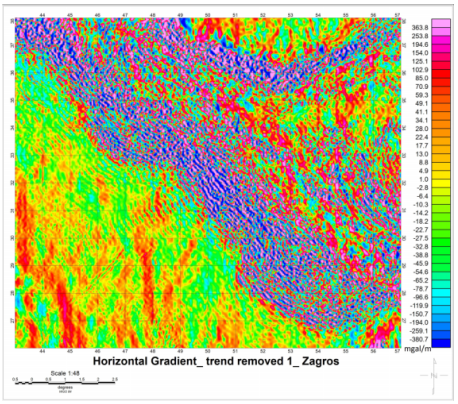

Fig. 20. Horizontal gradient filter map of the Zagros.

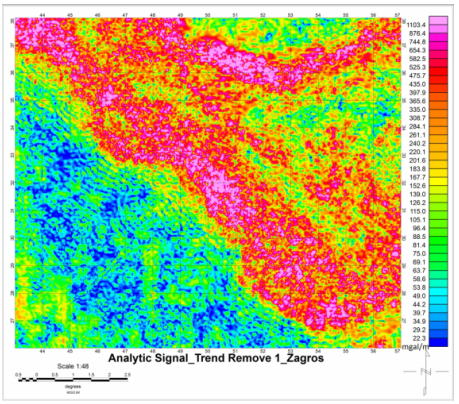

Fig. 21. Analytical signal filter map of the Zagros.

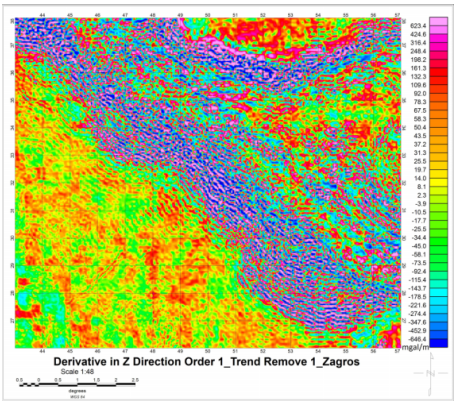

Fig. 22. First-order vertical derivative filter map of the Zagros.

maximum and minimum anomalies have been well characterized, and the reason for the colour change or anomalies resulting from the application of the analytical signal filter is its 90 degree phase change due to the nature of the filter (already explained). In these figures, the anomalies extend from northwest to southeast with indentations and densities.

Potensoft software including MATLAB codes was also used for further check and validate these filters (*Arısoy and Dikmen, 2011*) and the Tilt Angle and Hyperbolic Tilt Angle filters were applied to the data using this software, shown in Figs. 23 and 24.

As mentioned earlier, these filters highlight the edge of all relatively deep

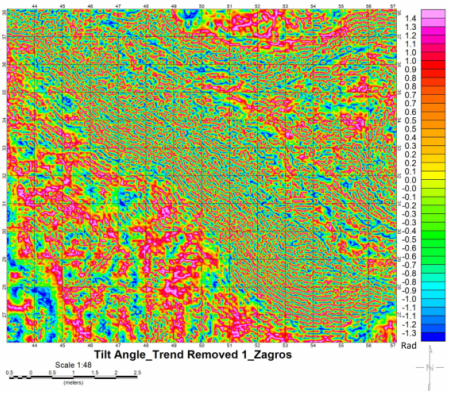

Fig. 23. Tilt angle filter map of the Zagros.

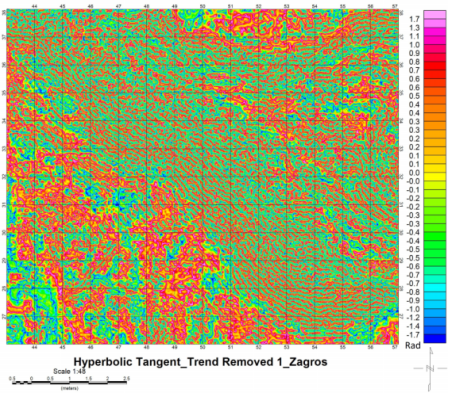

Fig. 24. Hyperbolic Tilt angle filter map of the Zagros.

and near surface anomalies because they lack depth sensitivity, as a result, the resulting maps are more crowded than previous filters; however, one can still see the structural difference of Zagros anomalies with the region containing Zagros. The conclusion is that these filters also confirm the results of the rest of the filters. Summary of the results of the above filters are shown in Fig. 25 and the anomalies continuation is marked with a black line. Comparing the results of these filters with this map gives more reliable results that will complement the geological data. Now we are testing regularized derivative filters (Figs. 26–30).

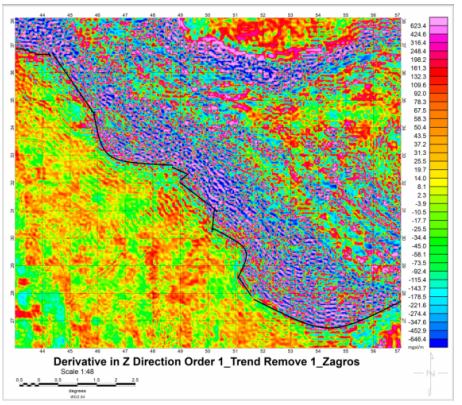

Fig. 25. Edge detection and continuation of Zagros anomalies with the black line.

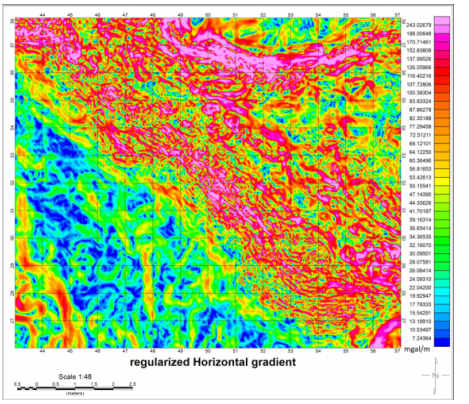

Fig. 26. Regularized horizontal gradient filter map of the Zagros.

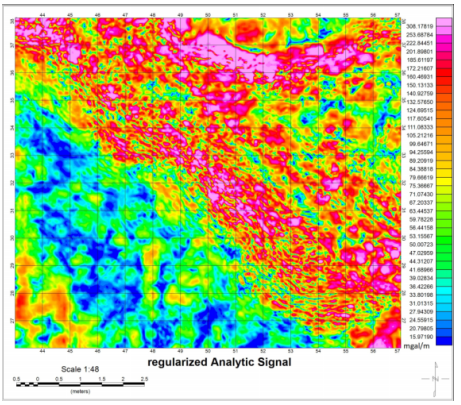

Fig. 27. Regularized analytic signal filter map of the Zagros.

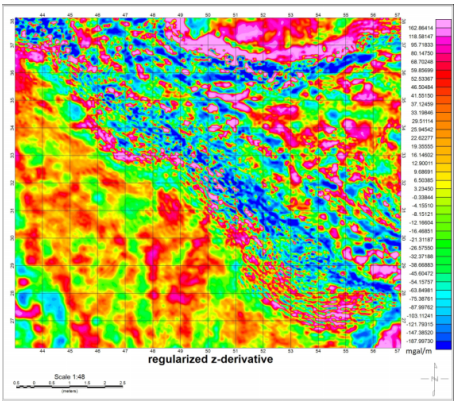

Fig. 28. Regularized first-order vertical derivative filter map of the Zagros.

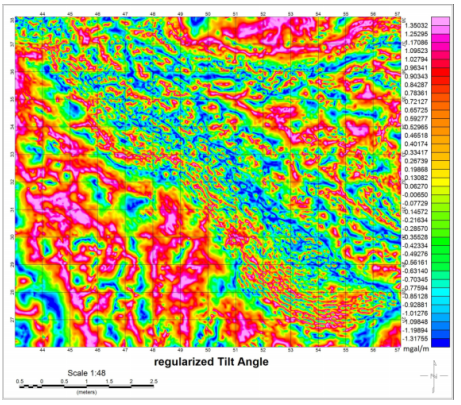

Fig. 29. Regularized tilt angle filter map of the Zagros.

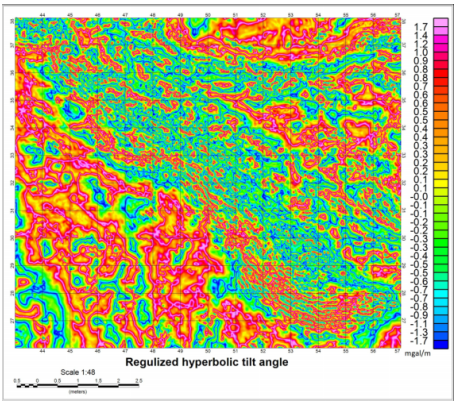

Fig. 30. Regularized hyperbolic tilt angle map of the Zagros.

As we have seen in these figures, regularized derivative filter has a much better performance.

4.5.3. Edge detection of the Red Sea gravity anomalies

Figs. 31, 32, and 33, respectively, show the maps obtained by applying horizontal gradient filters, analytical signal and first-order vertical derivative on the Red Sea data. In these figures, the edge of maximum and minimum

anomalies is also obvious, but more complex than the Zagros region. Figs. 34 and 35 are the results of applying tilt angle and hyperbolic tilt angles to the data. These filters also confirm previous results.

Figures 34 and 35 are the result of applying tilt angle and hyperbolic tilt angle filters to the data.

Summary of the results of the above filters are shown in Fig. 36 and the anomalies continuation is marked the black line.

Given that the data used are derived from gravimetric satellite, it is obvious that the satellite data is much less sensitive to ground-based data survey, so it cannot be expected to make all the anomalies visible. If more accurate gravimetric data (such as ground-based survey) are available, gravimetric method is a great way to identify small and large anomalies in the area. The overall result of the study of the two zones is that the Zagros and Red Sea gravity anomalies have one continuity (from northwest to southeast) with this difference which there is a greater overall slope in the Red Sea.

In the following the results of the implementing regularized derivative filters are presented and by comparing the Figs. 37 to 41 with the Figs. 32 to 36 again it is completely clear that regularized derivative filters have much better performance.

4.6. Inversion modelling of Zagros and the Red Sea gravity anomalies

Before proceeding further, it is important to note that since the EGM2008 satellite data output is in latitude and longitude, the UTM coordinate points need to be used in order to use the upward continuation filter. By converting the coordinates, the Zagros and Red Sea anomalies each fall into three zones. Red Sea anomalies are located in zones 36, 37 and 38 and Zagros anomalies are located in zones 38, 39 and 40 respectively. The most extensive zones (zones 37 for Red Sea and 39 for Zagros) were used to apply upward continuation filter and 3D modelling.

4.6.1. Red Sea gravity anomalies

This section presents the results of the inversion of the gravimetric data of the Red Sea anomalies using Grav3D software. The results of 3-D inversion

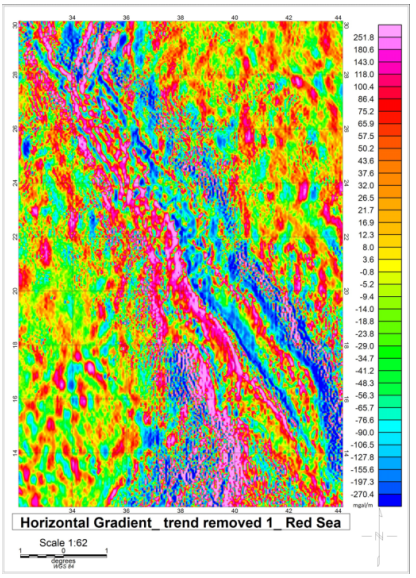

Fig. 31. Horizontal gradient filter map of the Red Sea.

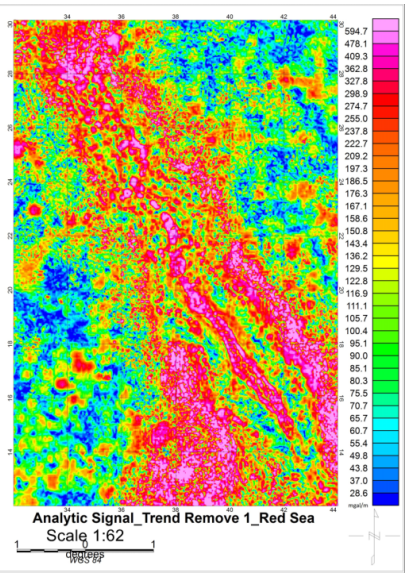

Fig. 32. The Analytical signal filter map of the Red Sea.

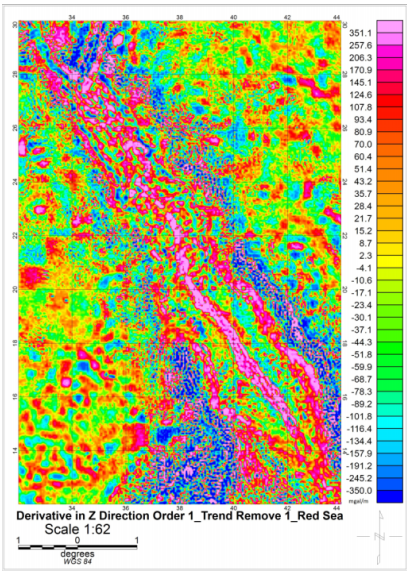

Fig. 33. First-order vertical derivative filter map of the Red Sea.

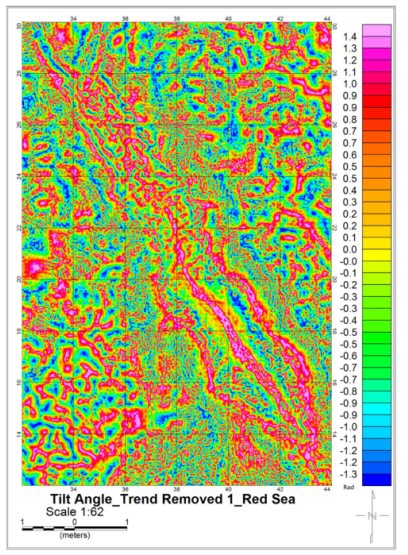

Fig. 34. Tilt angle filter map of the Red Sea.

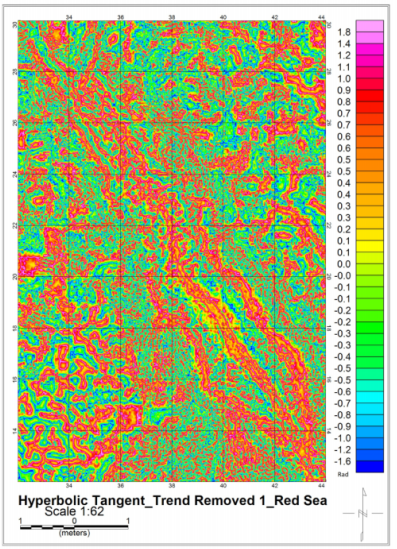

Fig. 35. Hyperbolic tilt angle filter map of the Red Sea.

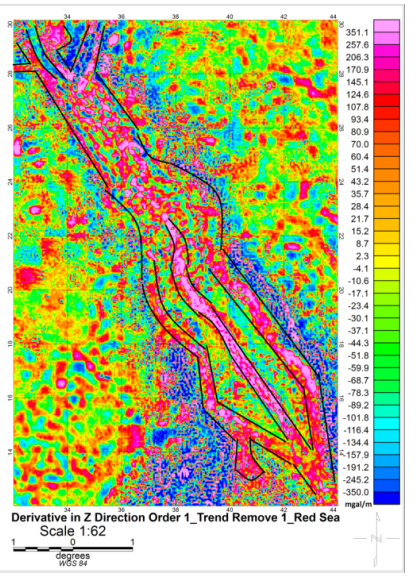

Fig. 36. Edge detection and continuation of Red Sea anomalies with black line.

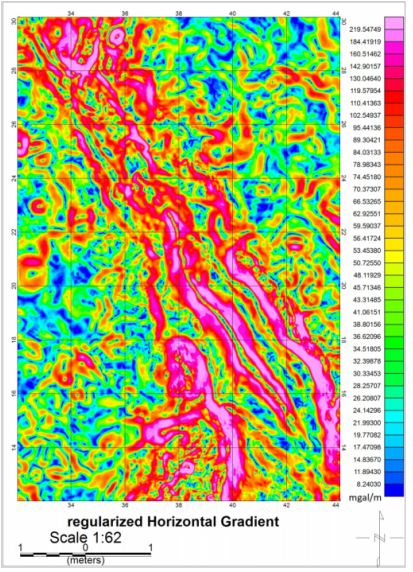

Fig. 37. Regularized horizontal gradient filter map of Red Sea.

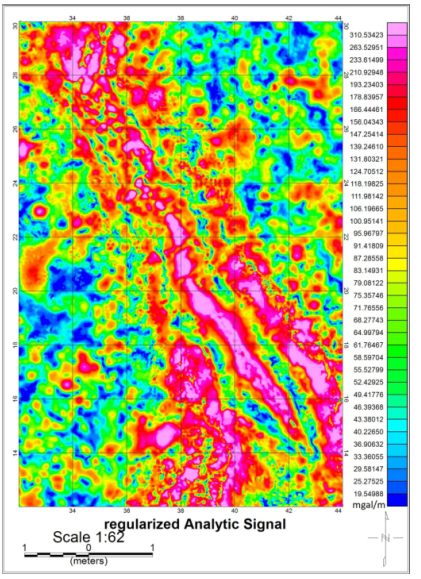

Fig. 38. Regularized Analytical signal filter map of Red Sea.

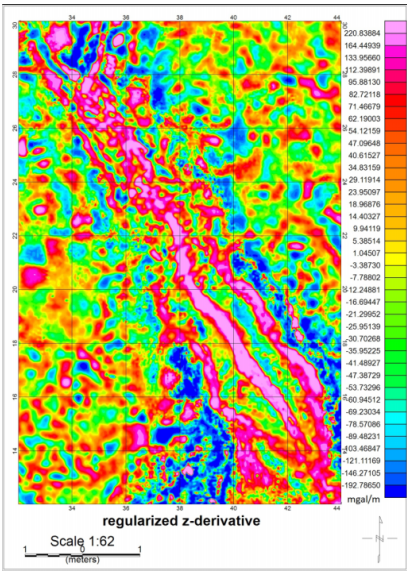

Fig. 39. Regularized vertical derivative filter map of the Red Sea.

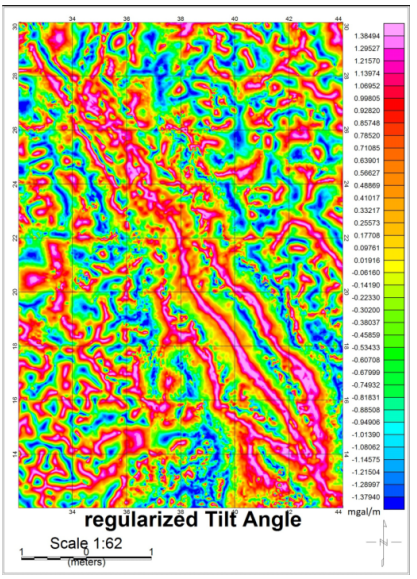

Fig. 40. Regularized tilt angle filter map of the Red Sea.

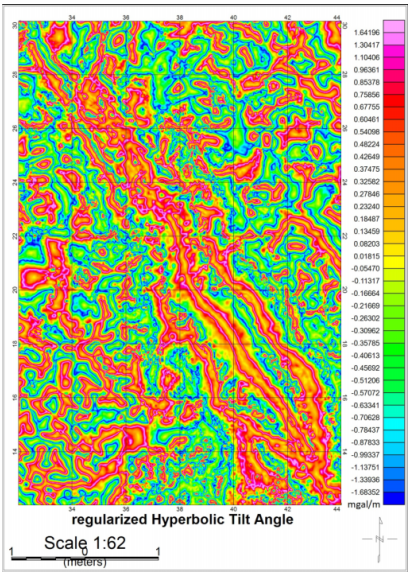

Fig. 41. Regularized Hyperbolic tilt angle filter map of the Red Sea.

are shown in Figs. 42 and 43, in which the main and secondary directions of the anomalies are well reconstructed. Fig. 44 shows the effective depth of the anomalies at 200 km from the surface and Fig. 45 confirms the anomaly ends at the 300 km. According to Fig. 36, the anomalous two-branch depth is lower than its original branch because these two branches continue to a depth of 100 km and then disappear (hence extending to a depth of 100 km).

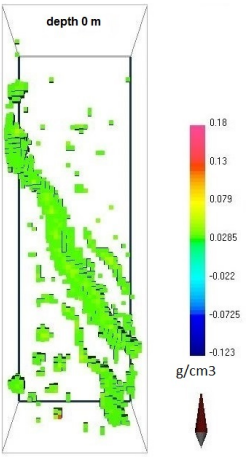

Fig. 42. Inversion of the Red Sea anomalies (top view).

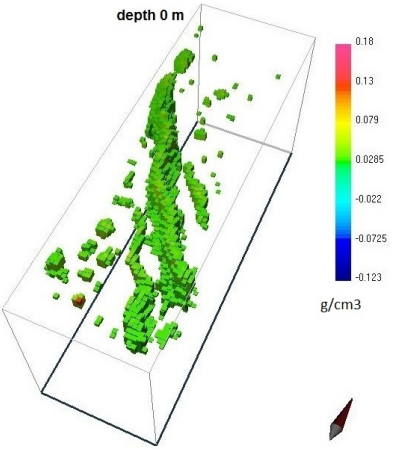

Fig. 43. Another view of Fig. 42.

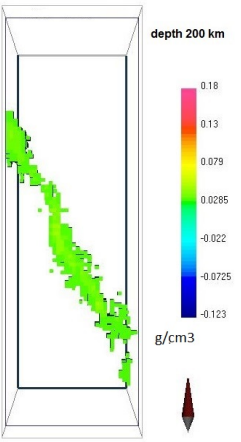

Fig. 44. Inversion at 200 km depth.

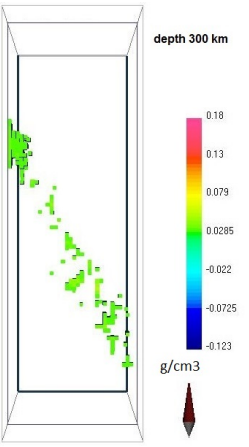

Fig. 45. Inversion at 300 km depth.

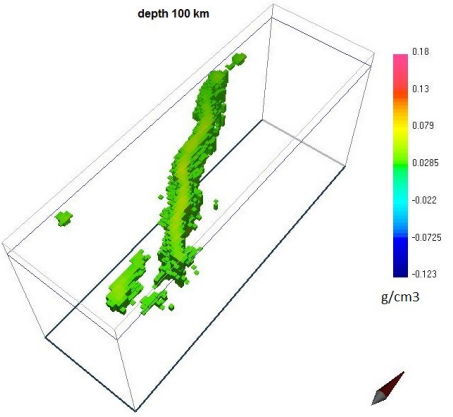

Fig. 46. Inversion of Red Sea anomalies at 100 km depth (to indicate the depth of sub-branches).

4.6.2. Zagros gravity anomalies

Figs. 47 to 50 show the inversion results. Fig. 47 shows a view from above and Fig. 48 shows another view of Zagros anomalies. According to Fig. 49, the effective depth of this anomaly is about 180 km and from the depth of 200 km, the anomalous root proceeds incoherently (Fig. 50) and it ends up at an approximate depth of 400 kilometres.

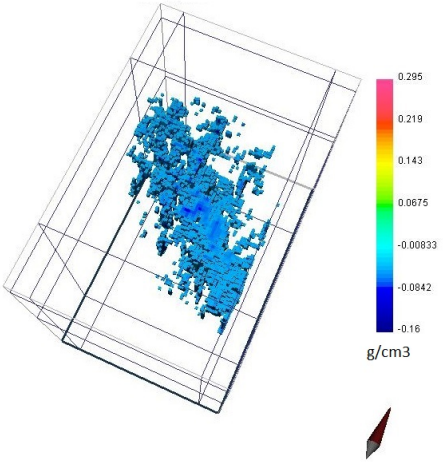

Fig. 47. Inversion of Zagros anomalies (top view).

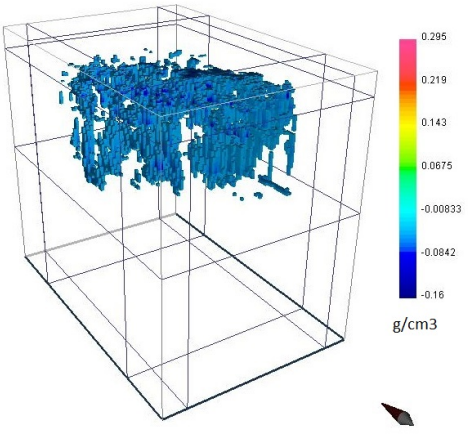

Fig. 48. Another view of Fig. 47.

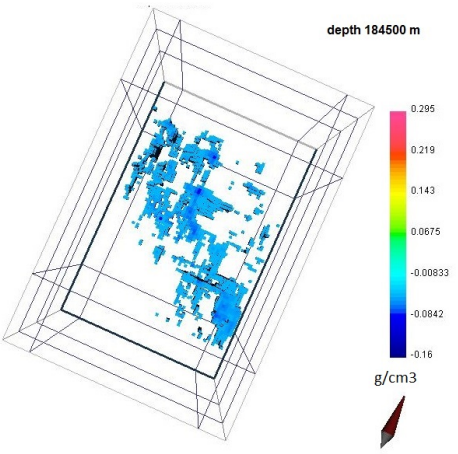

Fig. 49. Inversion at an approximate depth of 184 km.

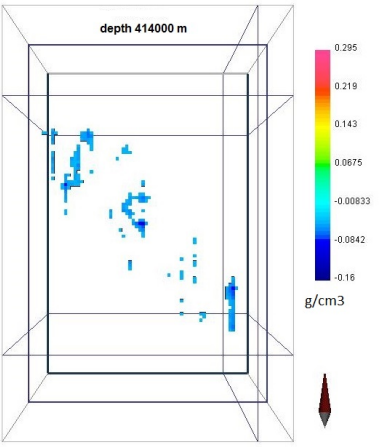

Fig. 50. Inversion at an approximate depth of 414 km.

5. Conclusion

In the case of Zagros gravity anomalies, the results of the edge detection filters indicate that the performance of the regularized derivatives with the elimination of the noise from the unregularized filters mode become an improvement in the results. Also these anomalies extend from northwest to southeast with indentations and reliefs. The general trend of this surface is in accordance with the geological trends of the area. The inversion results also show that the effective depth of this anomaly is about 180 km and after that, the anomalous root proceeds incoherently and it ends up at an approximate depth of 400 kilometres. In the case of anomalies of the Red Sea, applying edge detection filters revealed that this region is more complex than the Zagros region and these anomalies started from the north-western corner and led to many fractures to the centre, then divided into three main branches, which were again interconnected in the southeast corner, there is also a subway to the south for the western branch. These results are in line with the geological features of the Red Sea and the curvature direction and even the western branch path are well shown. Three-dimensional modelling also showed that the effective depth of these anomalies is 200 km from the surface and eventually end at about 300 km. Also the depth of the two

branches of this anomaly was lower than its main branch because these two branches continue to a depth of 100 km and then disappear.

References

Agah A., Doulati Aredejani F., Moradzadeh A., Tabatabaei Raeisi H., 2004: Integrating aerial and ground magnetic data to identify oil potentials in the Tabas area. 8th Iranian Geological Conference.

Agard P., Omrani J., Jolivet L., Mouthereau F., 2005: Convergence history across Zagros (Iran): constraints from collisional and earlier deformation. Int. J. Earth Sci., (Geologische Rundschau), **94**, 3, 401–419, doi: 10.1007/s00531-005-0481-4.

Alavi M., 1994: Tectonics of the Zagros orogenic belt of Iran: New data and interpretations. Tectonophysics, **229**, 3-4, 211–238, doi: 10.1016/0040-1951(94)90030-2.

Alavi M., 2007: Structures of the Zagros fold-thrust belt in Iran. Am. J. Sci., **307**, 9, 1064–1095, doi: 10.2475/09.2007.02.

Allahyari K., Saccani E., Pourmoafi M., Beccaluva L., Masoudi F., 2010: Petrology of mantle peridotites and intrusive mafic rocks from the Kermanshah ophiolitic complex (Zagros belt, Iran): implications for the geodynamic evolution of the neo-Tethyan oceanic branch between Arabia and Iran. Ofioliti, **35**, 2, 71–90.

Ariamanesh M., Mahmoudpour Z., 2012: Survey of hidden faults in Ahar region based on airborne graviy data. National Congress Planning the Pathology and Earthquake Effects. 21 August 2012 in East Azerbaijan Province.

Arısoy M. Ö., Dikmen Ü., 2011: Potensoft: MATLAB-based software for potential field data processing, modeling and mapping. Comput. Geosci., **37**, 7, 935-942, doi: 10.1016/j.cageo.2011.02.008.

ArRajehi A., McClusky S., Reilinger R., Daoud M., Alchalbi A., Ergintav S., Gomez F., Sholan J., Bou-Rabee F., Ogubazghi G., Haileab B., Fisseha S., Asfaw L., Mahmoud S., Rayan A., Bendik R., Kogan L., 2010: Geodetic constraints on present-day motion of the Arabian Plate: Implications for Red Sea and Gulf of Aden rifting. Tectonics, **29**, 3, TC3011, doi: 10.1029/2009TC002482.

Berberian M., 1995: Master "blind" thrust faults hidden under the Zagros folds: active basement tectonics and surface morphotectonics. Tectonophysics, **241**, 3-4, 193–224, doi: 10.1016/0040-1951(94)00185-C.

Besse S., Rebouillat D., Marie I., Puvion-Dutilleul F., Hovanessian A. G., 1998: Ultrastructural localization of interferon-inducible double-stranded RNA-activated enzymes in human cells. Exp. Cell Res.,**239**, 2, 379–392, doi: 10.1006/excr.1997.3908.

Blakely R. J., 1996: Potential theory in gravity and magnetic applications. Cambridge University Press, Revised edition, 464 p.

Bosworth W., Huchon P., McClay K., 2005: The Red Sea and Gulf of Aden basins. J. Afr. Earth Sci., **43**, 1-3, 334–378, doi: 10.1016/j.jafrearsci.2005.07.020.

Camp V. E., Roobol M. J., 1992: Upwelling asthenosphere beneath western Arabia and its regional implications. J. Geophys. Res., **97**, B11, 15255–15271, doi: 10.1029/92JB00943.

Cooper G. R. J., Cowan D. R., 2006: Enhancing potential field data using filters based on the local phase. Comput. Geosci., **32**, 10, 1585–1591, doi: 10.1016/j.cageo.2006.02.016.

Danaei G., Finucane M. M., Lu Y., Singh G. M., Cowan M. J., Paciorek C. J., Lin J. K., Farzadfar F., Khang Y.-H., Stevens G. A., Rao M., Ali M. K., Riley L. M., Robinson C. A., Ezzati M., 2011: National, regional, and global trends in fasting plasma glucose and diabetes prevalence since 1980: systematic analysis of health examination surveys and epidemiological studies with 370 country-years and 2.7 million participants. Lancet, **378**, 9785, 31–40, doi: 10.1016/S0140-6736(11)60679-X.

Dehghani G. A., Makris J., 1984: The gravity field and crustal structure of Iran. Neues Jahrb. Geol. Paläontol. – Abhandlungen, **168**, 2-3, 215–229, doi: 10.1127/njgpa/168/1984/215.

Deif A., Al-Shijbi Y., El-Hussain I., Ezzelarab M., Mohamed A. M. E., 2017: Compiling an earthquake catalogue for the Arabian Plate, Western Asia. Journal of Asian Earth Sciences, **147**, 345–357, doi: 10.1016/j.jseaes.2017.07.033.

Del Chiaro M., Rangelova E., Halimi A., Ateeb Z., Scandavini C., Valente R., Segersvärd R., Arnelo U., Verbeke C. S., 2019: Pancreatectomy with arterial resection is superior to palliation in patients with borderline resectable or locally advanced pancreatic cancer. HPB, Oxford, **21**, 2, 219–225, doi: 10.1016/j.hpb.2018.07.017.

Doulati Ardejani F., 2011: Raw survey data and interpretation of Marvdasht Exploration Area. Master thesis, Amirkabir University, Faculty of Mining, Tehran.

Ebrahimzadeh Ardestani V., 2010: Applied Gravity. In: Mineral Exploration, Engineering Geology. Tehran, Institute of Tehran University.

Falcon N. L., 1969: Problems of the relationship between surface structure and deep displacements illustrated by Zagros range. In: Kent P. E., Satterthwaite G. E., Spencer A. M.: Time and Place in Orogeny. Geol. Soc. Spec. Publ., **3**, 9–21, doi: 10.1144/GSL.SP.1969.003.01.02.

Foulger G. R., Pierce C., 2007: Geophysical Methods in Geology. Teaching Handbook, University of Durham, UK, 78 p.

Ghasemi A., Talbot C. J., 2006: A new tectonic scenario for the Sanandaj–Sirjan Zone (Iran). J. Asian Earth Sci., **26**, 6, 683–693, doi: 10.1016/j.jseaes.2005.01.003.

Giese P., Makris J., Akashe B., Röwer P., Letz H., Mostaanpour M., 1984: The crustal structure in Southern Iran derived from seismic explosion data. Neues Jahrb. Geol. Paläontol. – Abhandlungen, **168**, 2-3, 230–243, doi: 10.1127/njgpa/168/1984/230.

Hadadian A., 2011: Precise boundary detection of potential field anomalies using local phase filters. M.Sc. Thesis, Shahrood University of Technology, 102 p.

Hinze W. J., 1990: The role of gravity and magnetic methods in engineering and environmental studies In: Geotechnical an Environmental Geophysics: Volume I: Review and Tutorial. Society of Exploration Geophysicists, 75–126, doi: 10.1190/1.9781560802785.ch4.

Horton B. K., Hassanzadeh J., Stockli D. F., Axen G. J., Gillis R. J., Guest B., Amini A., Fakhari M. D, Zamanzadeh S. M., Grove M., 2008: Detrital zircon provenance of Neoproterozoic to Cenozoic deposits in Iran: Implications for chronostratigraphy and collisional tectonics. Tectonophysics, **451**, 1-4, 97–122, doi: 10.1016/j.tecto.2007.11.063.

Jafarzadeh V., 2015: Three-dimensional inverse modeling of gravity data using the Li-Oldenburg method (Case study: Sabzevar region). Master thesis. Shahrood University of Technology.

Kolagari A. A., 1992: Principles of geophysical exploration, Radish Publishing, 585 p.

Li Y., Oldenburg D. W., 1998: 3-D inversion of gravity data. Geophysics, **63**, 1, 109–119, doi: 10.1190/1.1444302.

Madahizadeh R., Mostafazadeh M., Ashkpour-Motlagh S. H., 2016: Earthquake Potential in the Zagros region (Iran), Acta Geophysica, De Gruyter, **64**, 5, 1462–1494, doi: 10.1515/acgeo-2016-0080.

Makris J., Rihm R., 1991: Shear-controlled evolution of the Red Sea: pull apart model. Tectonophysics, **198**, 2-4, 441–466, doi: 10.1016/0040-1951(91)90166-P.

Miller H. G., Singh V., 1994: Potential field tilt—a new concept for location of potential field sources. J. Appl. Geophys., **32**, 2-3, 213–217, doi: 10.1016/0926-9851(94)90022-1.

Morcos S. A., 1970: Physical and chemical oceanography of the Red Sea. Oceanogr. Mar. Biol. Ann. Rev., **8**, 73–202.

Nabighian M. N., 1972: The analytic signal of two-dimensional magnetic bodies with polygonal cross-section: Its properties and use for automated anomaly interpretation. Geophysics, **37**, 3, 507–517, doi: 10.1190/1.1440276.

Nowroozi A. A., 1971: Seismotectonics of the Persian plateau, eastern Turkey, Caucasus and Hindu-Kush regions. Bull. Seismol. Soc. Am., **61**, 2, 317–341.

Pašteka R., Richter F. P., Karcol R., Brazda K., Hajach M., 2009: Regularized derivatives of potential fields and their role in semi-automated interpretation methods. Geophys. Prospect., **57**, 4, 507–516, doi: 10.1111/j.1365-2478.2008.00780.x.

Paterson N. R., Reeves C. V., 1985: Applications of Gravity and Magnetic Surveys: The State-of-the-Art in 1985. Geophysics, **50**, 12, 2558–2594, doi: 10.1190/1.1441884.

Phillips N., 2001: Geophysical inversion in an integrated exploration program: examples from the San Nicolás deposit. University of British Columbia. Vancouver, Canada: Master's Thesis.

Rasul N. M. A., Stewart I. C. F., 2015: The Red sea. The Formation, Morphology, Oceanography and Environment of a Young Ocean Basin. Springer Earth System Sciences.

Reilinger R., McClusky S., ArRajehi A., 2015: Geodetic Constraints on the Geodynamic Evolution of the Red Sea. In: Rasul N., Stewart I. (Eds.): The Red Sea. Springer Earth System Sciences, Springer, Berlin, Heidelberg, 135-149, doi: 10.1007/978-3-662-45201-1_7.

Reynolds J. M., 1997: An introduction to applied and environmental geophysics. John Wiley and Sons.

Saccani E., Allahyari K., Beccaluva L., Bianchini G., 2013: Geochemistry and petrology of the Kermanshah ophiolites (Iran): Implication for the interaction between passive rifting, oceanic accretion, and OIB-type components in the Southern Neo-Tethys Ocean. Gondwana Res., **24**, 1, 392–411, doi: 10.1016/j.gr.2012.10.009.

Sella G. F., Dixon T. H., Mao A., 2002: REVEL: A model for Recent plate velocities from space geodesy, J. Geophys. Res., **107**, B4, 2081, doi: 10.1029/2000JB000033.

Snyder D. B., Barazangi M., 1986: Deep crustal structure and flexure of the Arabian Plate beneath the Zagros collisional mountain belt as inferred from gravity observations. Tectonics, **5**, 3, 361–373, doi: 10.1029/TC005i003p00361.

Stern R. J., Johnson P. R., 2010: Continental lithosphere of the Arabian Plate: A geologic, petrologic, and geophysical synthesis. Earth Sci. Rev., **101**, 1, 29–67, doi: 10.1016/j.earscirev.2010.01.002.

Sultan M., Becker R., Arvidson R. E., Shore P., Stern R. J., El Alfy Z., Attia R. I., 1993: New constraints on Red Sea rifting from correlations of Arabian and Nubian Neoproterozoic outcrops. Tectonics, **12**, 6, 1303–1319, doi: 10.1029/93TC00819.

Swartz D. H., Arden D. D., 1960: Geologic history of the Red Sea area. AAPG Bull., **44**, 10, 1621–1637.

Verduzco B., Fairhead J. D., Green C. M., MacKenzie C., 2004: New insights into magnetic derivatives for structural mapping. Lead. Edge, **23**, 2, 116–119, doi: 10.1190/1.1651454.

Walpersdorf A., Hatzfeld D., Nankal H., Tavakoli F., Nilforoushan F., Tatar M., Vernant P., Chéry J., Masson F., 2006: Difference in the GPS deformation pattern of North and Central Zagros (Iran). Geophys. J. Int., **167**, 3, 1077–1088, doi: 10.1111/j.1365-246X.2006.03147.x.

Williams N. C., 2008: Geologically-constrained UBC–GIF gravity and magnetic inversions with examples from the Agnew-Wiluna greenstone belt, Western Australia. University of British Columbia, Vancouver, Canada, Ph.D. Thesis.

Contributions to Geophysics and Geodesy Vol. 50/1, 2020 (33–47)

Could the directly measured data of transpiration be replaced by model outputs?

Hana STŘEDOVÁ[1,2,*], Jana KLIMEŠOVÁ[1], Tomáš STŘEDA[1,2], Petra FUKALOVÁ[1]

[1] Faculty of AgriSciences, Mendel University in Brno, Zemědělská 1665/1, 613 00 Brno, Czech Republic

[2] Department of Meteorology and Climatology, Czech Hydrometeorological Institute, Brno Branch, Kroftova 43, 616 67 Brno, Czech Republic

Abstract: Successful upscaling of the direct measurement of evapotranspiration at individual plant level to canopy level with specific microclimatic conditions has recently received considerable attention of scientific community. And since the knowledge of transpiration is among important inputs of various experiments on solitary plant level the paper employs the reverse approach – the downscaling from the canopy to individual plant. The main task of the study is thus to compare Penman–Monteith method of computing potential evapotranspiration with directly measured values of transpiration of maize. Since the model deals with canopy level and the direct measurement is being carried out on level of individual plants, this comparison answers the question if the time-consuming and demanding measurement of transpiration on plant level could be substitute by relative easily reachable model outputs. The results shown that evapotranspiration of maize computed by Penman–Monteith model cannot be successfully downscaled back to the solitary plant level. The correlation coefficient between these two data series for three individual phenological stages vary from 0.5831 to 0.7803 ($\alpha = 0.01$) while for whole growing period regardless phenological stage is 0.6925 ($\alpha = 0.01$). The directly measured data of transpiration cannot by simply replaced by modelled data, but their application after conversion using regression equations is possible with certain level of inaccuracy.

Key words: maize, sap flow, stem heat balance, transpiration model, the Czech Republic, Penman–Monteith

1. Introduction

Changes in transpiration values, which are strongly dependent on meteo-

*corresponding author: e-mail: hana.stredova@mendelu.cz

doi: 10.31577/congeo.2020.50.1.2

rological variables, are induced in accordance with the plant's phenological stage (*Pivec et al., 2009*), the water levels in the soil (*Irmak and Mutiibwa, 2010*) or the water potential of the leaves (*Li et al., 2002*).

Several methods have been used to determine transpiration from individual plants, including tracer measurements for calculations of the sap flow velocity and porometer measurements of leaf transpiration for estimation of the stomatal conductance. Direct measurements of evapotranspiration with using of weighing lysimeters or eddy covariance are difficult to install and operate although they provide the most realistic and accurate data.

Transpiration is closely related to water flow in the xylem (sap flow). Therefore, methods for the evaluation of sap flow may be used to measure either the water consumption of plants (*Bethenod et al., 2000*) or the stomatal conductivity at the leaf or plant level (*Ewers et al., 2007*). Methods for sap flow measurement are based on the physical characteristics of water and employ the heat transferred by water contained in the xylem. The "heat pulse method" involves measurement of the gradual speed of flow of a short pulse of heat in the stem or trunk (*Cohen et al., 1988; Green, 1993*). The "thermal dissipation method" is based on the difference between the temperature of a heated indicator and another sensor, which is influenced by the rate of sap flow (*Granier, 1985*). The "Stem Heat Balance" method SHB (*Lindroth et al., 1995; Smith and Allen, 1996; Kučera et al., 1977*) involves direct electrical warming of tissues and internal measurement of temperature. This method may be applied to crops with larger stem diameters (*Cohen and Li, 1996*), such as maize and sunflower (*Ishida et al., 1991*), oilseed rape (*Merta et al., 2001; Pivec et al. 2011*) or cotton (*Ham et al., 1990; Dugas et al., 1994*). The effect of soil water shortages on plant transpiration, as evaluated by measuring xylem sap flow, has been described by *Bethenod et al. (2000)*, *Jara et al. (1998)*, *Gavloski et al. (1992)* and *Sameshima et al. (1995)*, among others. *Jara et al. (1998)* confirmed that the sap flow measurement method is able to detect differences in water consumption by plants grown under different irrigation regimes as well as field conditions. In short, several studies have shown that sap flow measurements with stem heat balance methods agree well with the results of gravimetric techniques. Sap flow measurement is therefore a suitable method for detecting changes in transpiration at the plant level. Long-term sap flow measurements may be used to help develop models of the (evapo)transpiration response to en-

vironmental variables, as well as crop simulation models, irrigation models etc.

Frequently used Penman–Monteith equation (e.g. equation with stomatal conductance measurement; *Zhang et al., 1997*) pro various uses and various plant species have been confronted with direct measurement of sap flow. A fairly good match between calculated and measured results in terms of their correlation is usually reported, except for several episodes. Nevertheless, the Penman–Monteith model needs auxiliary sub-models or parameterizations for the stomatal conductances and need local calibrations.

Plants are widely separated in many agronomic, agroforestry, horticultural and forestry situations and are best considered as isolated plants or as rows of plants. It is of practical and theoretical interest to understand the controls on the transpiration rate of single plants. Models based on *Monteith (1965)*, including the Penman–Monteith equation as parameterized by the FAO-56 bulletin (*Allen et al., 1998*) to compute grass reference evapotranspiration, being derived from canopy do not reflect the real situation of solitary plant. It thus limits their relevance for detail experiments carried out on solitary plant level, such as various laboratory or pot experiments. Stand microclimate, mainly of dense seeded crops usually significantly differs from pot experiments climate (*Středa et al., 2011; Krčmářová et al., 2016*).

To obtain the precise a detail data on transpiration (e.g. 10-minute interval) in experiments on solitary plant level (not on canopy level) is necessary to measure it in various regimes and sufficient number of plants due to stem-to-stem variability in sap flow, preferably under standard stand conditions. The sap flow measurement itself should also be accompanied with measuring of many environmental and biological variables. Ideal is continuous measurement throughout wide range of phenological stages, including the generative period and senescence of the plant not only during short (several days duration) periods.

The measurements of sap flow from individual stems need to be upscaled with the using of sophisticated upscaling functions to derive the transpiration of the entire stand. It is therefore of both scientific and practical importance to develop an accurate upscaling method for extrapolating measured stem-level transpiration to the entire crop community (*Duan et al., 2017*).

A common approach to simulate crop evapotranspiration is the crop co-

efficient technique presented in FAO-56 bulletin (*Allen et al., 1998*). Crop coefficient curves can be developed as a function of time, plant growth stage, thermal unit or growing degree days (GDD), and leaf area index or canopy cover (*Martel et al., 2018*). To top it all there are inter varietal differences of crop coefficient. It limits the relevance of the method for precise experiments. For example *Xu et al. (2018)* found out seasonal crop coefficients at initial stage, mid-stage and late stage 0.46, 1.53, 1.22 and 0.44, 1.40, 1.09 for large-sized variety and small-sized variety of maize, respectively. It should be taken more into account especially for sizing of irrigation, calculation of water supply in the soil, crop growth models, crop yield models etc. In addition, *Anapalli et al. (2016)* observed, that crop coefficients calculated with measured evapotranspiration and the short grass or alfalfa crop reference evapotranspiration methods varied from year to year.

Nevertheless, *Pereira et al. (2006)* deployed concept, that if soil water is not limiting, the transpiration will be conditioned by the leaf area without the need of a crop coefficient. Canopy transpiration of irrigated orchard apple trees, olives, grapevines, and an isolated walnut tree was reliably estimated through the use of the conventional grass reference evapotranspiration parameterized by the FAO-56 bulletin (*Allen et al., 1998*) corrected only by the canopy leaf area.

Since detail transpiration measurement by stem heat balance method is expensive and time-consuming method and at the same time the knowledge of transpiration is among important inputs of various experiments on solitary plant level there is the following question erasing: Could the modelled evapotranspiration data on canopy level be successfully use for precise biological experiments on solitary plant level? By other words, could they be successfully downscaled back to the plant level?

We should be aware, that in order to validate any model of (evapo)transpiration by its direct measurements by lysimeters, evapometers and or by stem heat balance sensors they must be placed in the same surrounding canopy on sufficiently large piece of land. However the reverse approach i.e. downscaling from the modelled canopy (evapo)traspiration to the solitary plant level should not respect this condition, because the experiments on this solitary level are being conducted beyond canopy (in pot experiments, laboratories, driven environment in phytotrons etc.).

2. Materials and methods

2.1. Experiment design

The experiment set comprised six particular plants of maize (line 2087 – the breeding materials of CEZEA Čejč) in three different meteorological years of the last decade. The years under investigation were selected in terms of evapotranspiration demands of atmosphere expressed by vapor pressure deficit (VPD): the year characterized by the highest values of VPD – "the dry year", the year with the medium values – "the normal year" and with the lowest values – "the wet year". The experiment itself was carried out using outdoor pot trials in the climate conditions of South Moravia (the Czech Republic). Six maize plants were sown in pot (size $0.4\,\mathrm{m}^2$ and volume of $200\,\mathrm{dm}^3$). Based on pedological analysis and continuous monitoring of soil moisture the available water holding capacity (AWHC) had permanently been maintained on the level of 90% since BBCH 40 phase i.e. development of harvestable vegetative plant parts (the BBCH scale is a internationally recognized system for a uniform coding of growth stages of plant species; *Meier, 1997*). Volume soil moisture [%] at the depth of 10–40 cm and soil water potential [bar] were measured throughout the experiment.

2.2. Direct measurement of transpiration on the plant level (Ea)

Transpiration (Ea, $\mathrm{mm.h}^{-1}$) was monitored by continuous measurement of xylemic sap flow in a 10-minute interval. The measurement system uses the non-destructive method "Stem Heat Balance" (SHB). The measuring system consists of a pair of thermocouples that are installed at a precise distance from each other on the plant stem. For plant species with a thin stem, an external heater is used in the upper thermocouple, and the temperature change is measured by an internal needle sensor in both thermocouples. At the point of thermocouples the stem is insulated with a cylindrical seal all over the perimeter. The entire system is protected from sunlight and rain by an aluminum cover. The electronic system maintains a constant temperature difference dT (while the power P is then proportional to the current intensity) (*Kučera et al., 1977; Ishida et al., 1991*). The heat supplied to the stem is drained by the flow of water in the xylem. At the same time, heat losses occur though. These losses can be derived by measuring the current transpiration flow under the rain or before the dawn and are included

in the calculation equations. The values of the transpiration flow (Q) are given in units [kg.h^{-1}] and converted to a surface area of 1 m^2 (Ea, mm.h^{-1}) according to canopy density in the pot experiment. The plants from BBCH 60 (flowering) until BBCH 89 (full maturity) were measured.

2.3. Modelling of the evapotranspiration on the canopy level (ETo)

At the effective height of the stand (i.e. 0.68 × actual height with extreme values of 0.53 to 0.86 (*Mölder et al., 1999*) solar radiation is transformed into other kinds of energy (*Hurtalová et al., 2003; Matejka and Huzulák, 1987; Matejka et al., 2002*), which has a significant impact on the temperature and humidity regime. The following meteorological elements were measured directly between plants at the effective height level, i.e. 0.68 × plant height:

- Average relative air humidity [%];
- Average air temperature [°C];
- Duration of solar radiation [hours];
- Average wind velocity [m.s^{-1}].

Based on this data the daily values of reference (potential) evapotranspiration of maize canopy were computed according to Penman–Monteith model (canopy parameters: height = 2 m; albedo = 0.3; stomatal conductivity = 100 m.s^{-1}). Reference evapotranspiration was computed according to FAO methodology (*Allen et al., 1998*) that is based on modified Penman–Monteith equation.

Data sap flow, i.e. the intensity of transpiration and meteorological data (average air temperature, average value of global radiation etc.), was always evaluated only for the day-time from sunrise to sunset (diurnal data).

2.4. Data evaluation

The growing period was divided into three particular periods on the basis of relative unique phenological phases:

- 1st period: BBCH 63–65 (flowering).
- 2nd period: BBCH 65–75 (full flowering – development of fruit).

- 3rd period: BBCH 75–85 (ripening; BBCH 85 – kernels yellowish to yellow, about 55% dry matter).

3. Results and discussion

Average daily values, which create the basis of evaluation, were calculated from continuously measured data. The following figures (Figs. 1–3) show the both model (ETo) and measured (Ea) transpiration in terms of meteorological parameters: global radiation, vapour pressure deficit (VPD). It was assessed separately for each year divided into the three periods with regard to the different course of transpiration depending on the plant growth phase.

Previous partial research of *Klimešová et al. (2013)* was focused on finding out the degree of influence of key agrometeorological elements on transpiration. Significant relationships among transpiration, global radiation and air temperature were found.

Relationship between measured transpiration Ea and model transpiration ETo was expressed by correlation coefficient. Correlation in first period r = 0.936 ($\alpha = 0.01$) for "the dry year", 0.705 ($\alpha = 0.05$) for "the normal year" and 0.935 ($\alpha = 0.01$) for "the wet year". In the second period r = 0.817

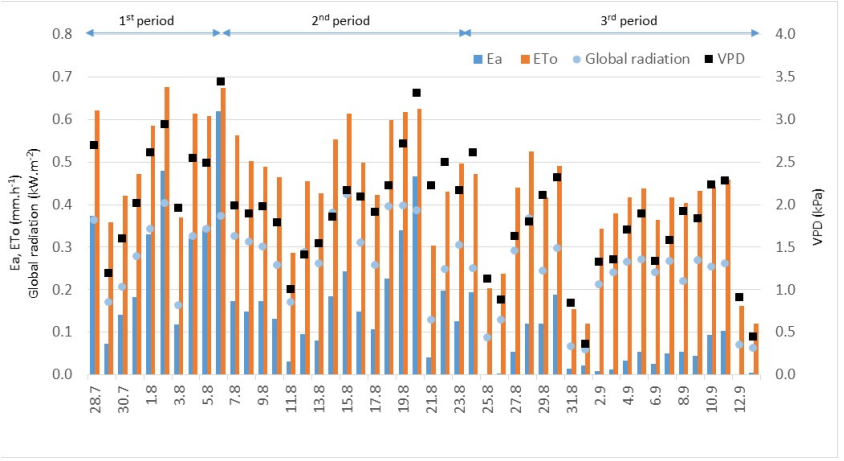

Fig. 1. Course of daily Ea and ETo ($mm.h^{-1}$) and global radiation and vapor pressure deficit (VPD) for three phenological periods in "dry year".

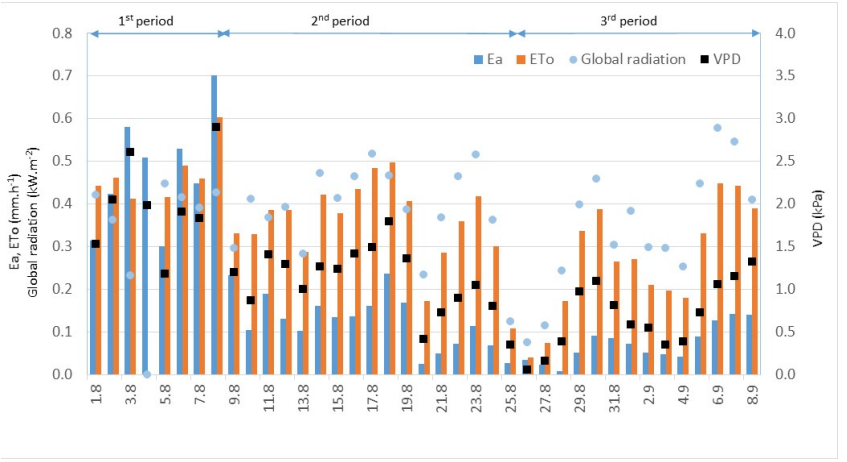

Fig. 2. Course of daily Ea and ETo ($mm.h^{-1}$) and global radiation and vapor pressure deficit (VPD) for three phenological periods in "normal year".

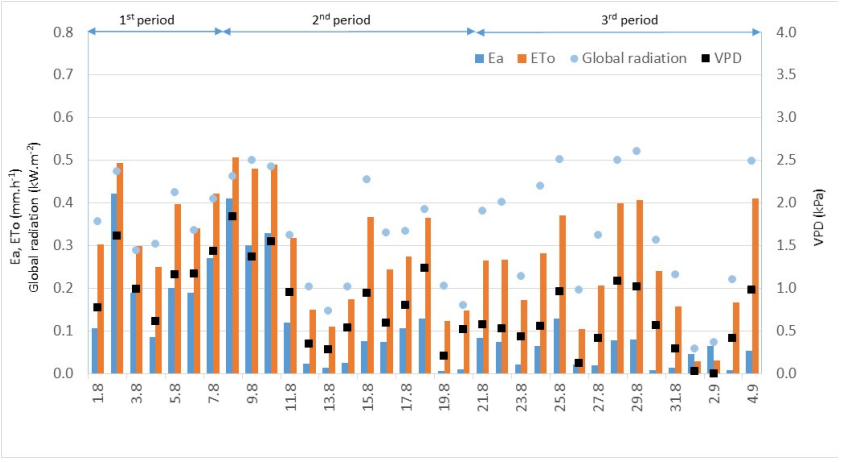

Fig. 3. Course of daily Ea and ETo ($mm.h^{-1}$) and global radiation and vapor pressure deficit (VPD) for three phenological periods in "wet year".

($\alpha = 0.01$) for "the dry year", r = 0.750 ($\alpha = 0.01$) for "the normal year", r = 0.924 ($\alpha = 0.01$) for "the wet year". In the third period r = 0.714 ($\alpha = 0.01$) for "the dry year", r = 0.869 ($\alpha = 0.01$) for "the normal year" and r = 0.531 ($\alpha = 0.05$) for "the wet year" (combined Fig. 4).

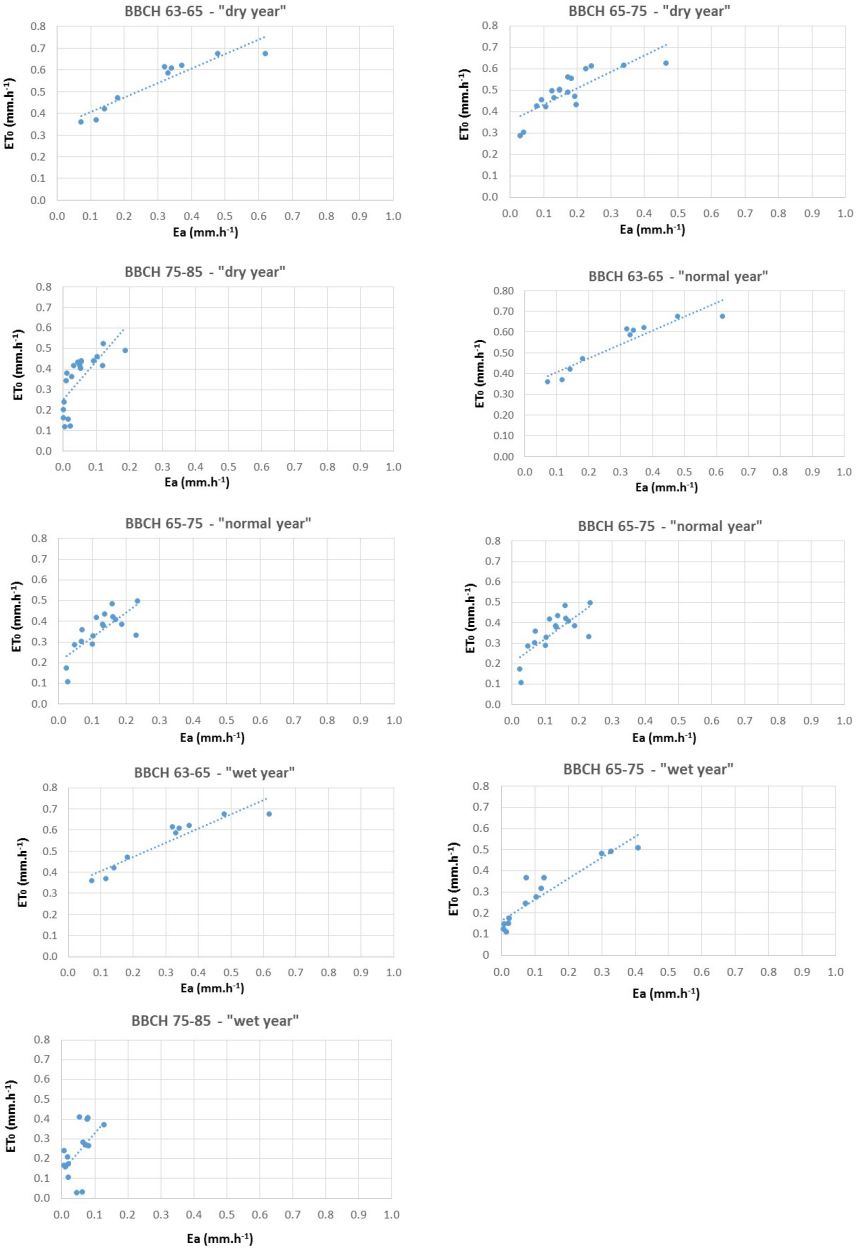

Fig. 4. Relationship between Ea and ETo ($\mathrm{mm.h^{-1}}$) for three individual phenological stages in three years.

Average Ea and ETo ($mm.h^{-1}$) values from three-year period were evaluated for three phenological periods is shown in Fig. 5.

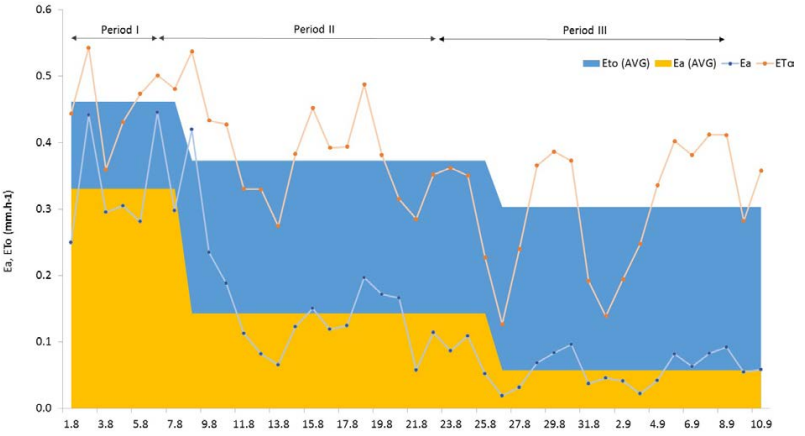

Fig. 5. Three-year average course of Ea and ETo ($mm.h^{-1}$) and their average values for three phenological periods.

Based on the regression dependence between modelled and measured transpiration, the relationships (combined Fig. 6) and dependence rate (Table 1) were derived.

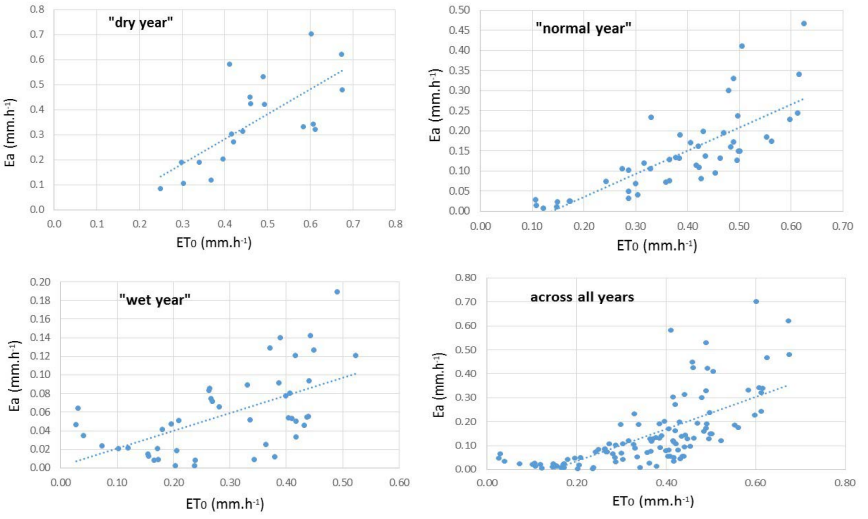

Fig. 6. Relationship between ETo a Ea.

Table 1. The conversion equations the level of significance.

	conversion equation	**correlation coefficient (r)**
year	$\mathrm{Ea} = 0.6713\,\mathrm{ETo} - 0.0990$	0.6925^{**}
1^{st} period	$\mathrm{Ea} = 0.9943\,\mathrm{ETo} - 0.1146$	0.7124^{**}
2^{nd} period	$\mathrm{Ea} = 0.5739\,\mathrm{ETo} - 0.0795$	0.7803^{**}
3^{rd} period	$\mathrm{Ea} = 0.1902\,\mathrm{ETo} + 0.0021$	0.5831^{**}

**statistically very significant ($\alpha = 0.01$)

On the basis of conversion equation the modification of modelled values for each phenological period was determined (Table 2).

Table 2. Conversion table between ETo and Ea (modification).

ETo	**Ea**			
	year	**1^{st} period**	**2^{nd} period**	**3^{rd} period**
0.0	0.00	0.00	0.00	0.00
0.2	0.04	0.08	0.04	0.04
0.4	0.17	0.28	0.15	0.08
0.6	0.30	0.48	0.26	0.12
0.8	0.44	0.68	0.38	0.15
1.0	0.57	0.88	0.49	0.19

The applicability of a lot of alternative models for evaporation and transpiration calculation is usually restricted to specific geographical locations and climatic regimes, because their parameters are derived from experiments employed at the local scale (*Tegos et al., 2013*).

The Penman–Monteith (PM) model and the Direct Method (DM) model are two of the most widespread transpiration models. Penman–Monteith model was primarily developed for crops grown in open field conditions. For each model, the values of meteorological variables such as air temperature, air humidity, solar radiation, as well as key plant characteristics, (e.g. leaf temperature for DM model) are needed to estimate crop transpiration.

According to *Morille et al. (2013)* study focused on usage of the PM model, the location of the meteorological parameters used to implement the model is a key factor that affects the results. The study demonstrates that the temperature and humidity considered in the PM model should be taken inside the crop and not above the crop, leading to a so-called PM-Like (PML) model. The PM-Like and the DM models, in a one-layer configura-

tion, give similar results and are in agreement with actual measurements. The PM model could even be successfully applied under greenhouse conditions, provided that some adjustments are made (thus defining the PM-Modified model).

The necessity of modifying the model is also desirable on the basis of proven differences in meteorological data measured at a standard climatic station and in a canopy, resp. monitoring of microclimate and microclimate. *Krčmářová et al. (2016)*, who, among other things, investigated the relationship between the relative humidity in the wheat canopy and calculated or measured meteorological values pointed out the necessity of continual canopy microclimate monitoring as well as complicatedness of canopy microclimate modelling. The prediction of air humidity in a wheat canopy cannot be based on data measured at standard climatological stations, as it has not been proven that there is a statistically strong dependence.

4. Conclusion

One of the most used transpiration model are Penman–Monteith model that was primarily developed for crops grown in open field conditions. In addition to the models, transpiration can be determined by direct measurement. However, these measurements are very technically demanding. The main task of the paper was to compare Penman–Monteith modelled values of evapotranspiration with directly measured transpiration values of the pot maize experiment.

Measuring of transpiration flow (sap flow) is a possible method for flow water quantification by plants in dependence on environmental factors while respecting the microclimatic specifics With regard to the phenological development of crops, it is appropriate to divide the growth period into partial periods.

The results show that it is not appropriate to use modelled values for single plant experiments without modification. Nevertheless, the conversion of the modified modelled values to single plant level is possible with statistically very significant level of reliability.

Since the conversion equations provided by this paper were derived from the pot measurement they can only be successfully used for the experiments carried out beyond canopy.

Acknowledgements. The paper was supported by the Ministry of Agriculture of the Czech Republic, Project No. *QK1720285 "New methods for adjustment of altered crop water requirements in irrigation systems across Czechia as affected by soil and climate changes"*.

References

Allen R. G., Pereira L. S., Raes D., Smith M., 1998: Crop evapotranspiration: guidelines for computing crop water requirements. Irrigation and Drainage Paper No. 56. FAO, Rome, Italy, 300 p.

Anapalli S. S., Ahuja L. R., Gowda P. H., Ma L., Marek G., Evett S. R., Howell T. A., 2016: Simulation of crop evapotranspiration and crop coefficients with data in weighing lysimeters. Agric. Water Manag., **177**, 274–283, doi: 10.1016/j.agwat.2016.08.009.

Bethenod O., Katerji N., Goujet R., Bertolini J. M., Rana G., 2000: Determination and validation of corn crop transpiration by sap flow measurement under field conditions. Theor. Appl. Climatol., **67**, 3-4, 153–160, doi: 10.1007/s007040070004.

Cohen Y., Fuchs M., Falkenflug V., Moreshet S., 1988: Calibrated heat pulse method for determining water uptake in cotton. Agron. J., **80**, 3, 398–402, doi: 10.2134/agronj1988.00021962008000030004x.

Cohen Y., Li Y., 1996: Validating sap flow measurement in field-grown sunflower and corn. J. Exp. Bot., **47**, 11, 1699–1707, doi: 10.1093/jxb/47.11.1699.

Duan L., Li Y., Yan X., Liu T., Wan X., 2017: Upscaling Stem to Community-Level Transpiration for Two Sand-Fixing Plants: *Salix gordejevii* and *Caragana microphylla*. Water, **9**, 5, doi: 10.3390/w9050361.

Dugas W. A., Heuer M. L., Hunsaker D., Kimball B. A., Lewin K. F., Nagy J., Johnson M., 1994: Sap flow measurements of transpiration from cotton grown under ambient and enriched CO_2 concentrations. Agric. For. Meteorol., **70**, 1-4, 231–245, doi: 10.1016/0168-1923(94)90060-4.

Ewers B. E., Mackay D. S., Samanta S., 2007: Interannual consistency in canopy stomatal conductance control of leaf water potential across seven tree species. Tree Physiol., **27**, 1, 11–24, doi: 10.1093/treephys/27.1.11.

Gavloski J. E., Whitfield G. H., Ellis C. R., 1992: Effect of restricted watering on sap flow and growth in corn (Zea mays L.). Can. J. Plant Sci., **72**, 2, 361–368, doi: 10.4141/cjps92-040.

Granier A., 1985: Une nouvelle méthode pour la mesure du flux de sève brute dans le tronc des arbres. Ann. For. Sci., **42**, 2, 193–200, doi: 10.1051/forest:19850204 (in French).

Green S. R., 1993: Radiation balance, transpiration and photosynthesis of an isolated tree. Agric. For. Meteorol., **64**, 3-4, 201–221, doi: 10.1016/0168-1923(93)90029-H.

Ham J. M., Heilman J. L., Lascano R. J., 1990: Determination of soil water evaporation and transpiration from energy balance and stem flow measurements. Agric. For. Meteorol., **52**, 3-4, 287–301, doi: 10.1016/0168-1923(90)90087-M.

Hurtalová T., Matejka F., Janouš D., Rožnovský J., 2003: Influence of a spruce forest stand on the flowing and air temperature and moisture vertical stratification. In: Rožnovský J., Litschmann, T. (Eds.): Workshop "Mikroklima porost", Brno, March 26, 2003, ISBN 80-86690_05-9, 66–79 (in Slovak with English summary).

Ishida T., Campbell G. S., Calissendorff C., 1991: Improved heat balance method for determining sap flow rate. Agric. For. Meteorol., **56**, 1-2, 35–48, doi: 10.1016/0168-1923(91)90103-W.

Irmak S., Mutiibwa D., 2010: On the dynamics of canopy resistance: Generalized linear estimation and relationships with primary micrometeorological variables. Water Resour. Res., **46**, 8, W08526, doi: 10.1029/2009WR008484.

Jara J., Stockle C. O., Kjelgaard, J., 1998: Measurement of evapotranspiration and its components in a corn (Zea Mays L.) field. Agric. For. Meteorol., **92**, 2, 131–145, doi: 10.1016/S0168-1923(98)00083-5.

Klimešová J., Středa T., Středová H., 2013: Maize transpiration in response to meteorological conditions. Contrib. Geophys. Geod., **43**, 3, 225–236, doi: 10.2478/congeo-2013-0014.

Krčmářová J., Pokorný R., Středa T., 2016: The course, stratification and possibility of simulating relative air humidity in winter wheat stand. Contrib. Geophys. Geod., **46**, 2, 137–154, doi: 10.1515/congeo-2016-0010.

Kučera J., Čermák J., Penka M., 1977: Improved thermal method of continual recording the transpiration flow rate dynamics. Biol. Plant., **19**, 6, 413–420, doi: 10.1007/BF02922976.

Li Y., Fuchs M., Cohen S., Cohen Y., Wallach R., 2002: Water uptake profile response of corn to soil moisture depletion. Plant Cell Environ., **25**, 4, 491–500, doi: 10.1046/j.1365-3040.2002.00825.x.

Lindroth A., Čermák J., Kučera J., Cienciala E., Eckersten H., 1995: Sap flow by heat balance method applied to small size *Salix* trees in a short-rotation forest. Biomass Bioenergy, **18**, 1, 7–15, doi: 10.1016/0961-9534(94)00085-8.

Martel M., Glenn A., Wilson H., Kröbel R., 2018: Simulation of actual evapotranspiration from agricultural landscapes in the Canadian Prairies. J. Hydrol. Reg. Stud., **15**, 105–118, doi: 10.1016/j.ejrh.2017.11.010.

Matejka F., Huzulák J., 1987: Analysis of the microclimate of the stand (Analýza mikroklímy porastu). Bratislava: VEDA, 232 p. (in Slovak).

Matejka F., Rožnovský J., Hurtalová T., Janouš D., 2002: Effect of soil drought on evapotranspiration of a young spruce forest. J. For. Sci., **48**, 4, 166–172, doi: 10.17221/11871-JFS.

Meier U., 1997: BBCH-Monograph. Growth stages of plants – Entwicklungsstadien von Pflanzen – Estadios de las plantas – D'eveloppement des Plantes. Blackwell Wissenschaftsverlag, Berlin und Wien, 622 p.

Merta M., Sambale C., Seidler C., Peschke G., 2001: Suitability of plant physiological methods to estimate the transpiration of agricultural crops. J. Plant Nutr. Soil Sci., **164**, 1, 43–48, doi: 10.1002/1522-2624(200102)164:1<43::AID-JPLN43>3.0.CO;2-W.

Mölder M., Grelle A., Lindroth A., Halldin S., 1999: Flux profile relationships over aboreal forest — roughness sublayer corrections. Agric. For. Meteorol., **98–99**, 645–658, doi: 10.1016/S0168-1923(99)00131-8.

Monteith J. L., 1965: Evaporation and Environment. Symposia of the Society for Experimental Biology, **19**, 205–234.

Morille B., Migeon C., Bournet P. E., 2013: Is the Penman–Monteith model adapted to predict crop transpiration under greenhouse conditions? Application to a new Guinea Impatiens crop. Sci. Hortic., **152**, 80–91, doi: 10.1016/j.scienta.2013.01.010.

Pivec J., Brant V., Bečka D., 2009: The influence of weather conditions on the sap flow of *Brassica napus* L. during the fructification and maturation stages. Ekológia, **28**, 1, 43–51, doi: 10.4149/ekol_2009_01_43.

Pivec J., Brant V., Bečka D., Cihlář P., 2011: Consumptive use of water in *Brassica napus* L. from flowering to ripening stage under rainless region conditions. Irrig. Drain., **60**, 4, 493–498, doi: 10.1002/ird.598.

Pereira A. R., Green S., Nova N. A. V., 2006: Penman–Monteith reference evapotranspiration adapted to estimate irrigated tree transpiration. Agric. Water Manag., **83**, 1-2, 153–161, doi: 10.1016/j.agwat.2005.11.004.

Sameshima R., Sakuratani T., Takenouchi A., 1995: Relationship between transpiration rate of soybean plants (*Glycine max* Merr. cv. Enrei) and soil water content estimated by stem heat balance and heat probe methods. J. Agric. Meteorol., **51**, 2, 153–157, doi: 10.2480/agrmet.51.153.

Smith D. M., Allen S. J., 1996: Measurement of sap flow in plant stems. J. Exp. Bot., **47**, 12, 1833–1844, doi: 10.1093/jxb/47.12.1833.

Středa T., Středová H., Rožnovský J., 2011: Orchards microclimatic specifics. In: Šiška B., Hauptvogl M., Eliašová M. (Eds.): Bioclimate: Source and Limit of Social Development, International Scientific Conference, 6th – 9th September 2011, Topoľčianky, Slovakia. Nitra: Slovak University of Agriculture in Nitra, 132–133.

Tegos A., Efstratiadis A., Koutsoyiannis D. A., 2013: A parametric model for potential evapotranspiration estimation based on a simplified formulation of the Penman–Monteith equation. In: Alexandris S. (Ed.): Evapotranspiration – An Overview. Chapter: 8, InTech, Rijeka, Croatia, 143–165, doi: 10.5772/52927.

Xu G., Xue X., Wang P., Yang Z., Yuan W., Liu X., Lou Ch., 2018: A lysimeter study for the effects of different canopy sizes on evapotranspiration and crop coefficient of summer maize. Agric. Water Manag., **208**, 1–6, doi: 10.1016/j.agwat.2018.04.040.

Zhang H., Simmonds L. P., Morison J. I. L., Payne D., 1997: Estimation of transpiration by single trees: comparison of sap flow measurements with a combination equation. Agric. For. Meteorol., **87**, 2-3, 155–169, doi: 10.1016/S0168-1923(97)00017-8.

Contributions to Geophysics and Geodesy Vol. 50/1, 2020 (49–60)

GIS application in abiotic risks regionalization for spring barley

Tomáš STŘEDA[1,2,*], Radim CERKAL[1], Lenka HÁJKOVÁ[2], Filip CHUCHMA[1,2], Tomáš KHEL[3], Jana KLIMEŠOVÁ[1]

[1] Mendel University in Brno, Zemědělská 1665/1, 613 00 Brno, Czech Republic

[2] Czech Hydrometeorological Institute, Na Šabatce 2050/17, 143 06 Praha – Komořany, Czech Republic

[3] Research Institute for Soil and Water Conservation, Žabovřeská 250, 156 27 Praha – Zbraslav, Czech Republic

Abstract: In recent years, there has been a noticeable uneven distribution of rainfall in Central Europe during the main vegetation season of most field crops. The rising air temperatures also increase the evapotranspiration demands of the environment and increase the frequency and length of heatwaves, which is a stress factor for plants. Using the GIS procedures, we identified the areas of significant abiotic risks occurring during the critical growth stages of spring barley (high air temperatures at the time of tillering and lack of soil moisture from the beginning of flowering to yellow ripening) with potential impact on grain yield in the Czech Republic. Unique datasets, including i) meteorological data, ii) phenological data, iii) pedological data, iv) land-use data, and v) geographic data, have been integrated and analysed using the sophisticated ArcGIS software environment. The method used in this study is universally applicable and allows comparisons at the local, regional, and supra-regional levels. The identification of risk areas will allow for a) finding tolerant varieties from problematic areas, b) locating the use of these varieties in risk areas and c) recommending and implementing adequate farming practices to reduce the impact of risk abiotic stressors on spring barley under current climate conditions. This will allow accurate estimation of weather impacts on spring barley grain yield in a particular year and precise application of countermeasures leading to reduced negative impacts on yield and the quality of spring barley production. Using the data and methods presented, we identified areas that correspond in good accordance to areas with spring barley yield deficits in dry years.

Key words: evapotranspiration, soil moisture, air temperature, phenology, ALADIN, barley, agroclimatology

*corresponding author: e-mail: streda@mendelu.cz

doi: 10.31577/congeo.2020.50.1.3

1. Introduction

The main abiotic stressors for agricultural crops reducing yields in Europe are agricultural drought as well as high air temperatures during the main growing season. Although drought in Central Europe is a relatively recent problem, worldwide it is the most serious abiotic stress affecting crop yields in the long term (*Boyer, 1982*). Plant production is based on maintaining transpiration in the absence of water. All other criteria are always secondary, where biomass production is concerned (*Blum, 2011; Chaves et al., 2011*).

According to *Bodner et al. (2015)*, three main types of climate can be distinguished in areas with intensive agricultural production. They differ mainly in the distribution of precipitation and evapotranspiration requirements, the type of soil and the length and beginning of the growing season. The climate of Central Europe is predominantly "supply-driven", whereby the water is mostly supplied by precipitation during the growing season. In Central Europe, there has generally been an increase in the uneven distribution of precipitation, combined with an increase in air temperature in recent decades. Although an increased incidence of extreme rainfall has been observed, local or regional drought has been more prevalent in recent decades as demands for evapotranspiration are increasing due to increasing air temperature (*Škvarenina et al., 2009*). Analyses of precipitation characteristics in the Czech Republic show that there is no decrease in the total amount of precipitation, but rather a shift towards greater inequality of its distribution over time (during the year). In the Czech Republic's environmental conditions, the number of days without rainfall may increase from the current 79.9 days to 141.6 days from 2071 through 2100, but no significant decrease in the amount of rainfall per year is expected. The climate models also predict an increase in the average sum of active temperatures above 10 °C for the Czech Republic from the current 2717 °C to 3732 °C. These changes increase the evapotranspiration demands of the environment to which agricultural crops will be exposed. In addition, temperatures above 20–25 °C can decrease the level of inhibitory substances in the plant, and thus reduce tiller formation of cereals (*Rawson, 1971*). The rate of tillering decreases at temperature above 25 °C (*Friend, 1966*). Modern barley varieties show strong ability to make a canopy denser during tillering. Tillering is thus crucial for barley's yield creation. Having in mind that barley's yield

is closely related to number of spikes, the low number of productive spikes might be compensated at latter phases just to a limited extent. Increasing frequency of unfavourable conditions at early spring (during tillering), especially higher temperatures and drought periods, can affect negatively the formation of spring barley yield and grain quality parameters (*Křen et al., 2015*), particularly under the central Europe climate. Plants grown in the warmer cropping season produced relatively few grains due to the short period of tillering as a results of high air temperatures compared with those grown in the colder crop season (*Tanaka and Nakano, 2019*).

The availability of soil moisture, together with global radiation and vapour pressure deficit, are among the main determinants of transpiration (*Du et al., 2011; She et al., 2013; Zeppel et al., 2008*). Daily or the long-term course of these variables affects the plant's transpiration flow (*Naithani et al., 2012*). Changes in transpiration intensity are considered to be an indicator of drought stress on the plant. *Blum (2005)* defines the onset of drought as a period when the plant's water demand is not satisfied, and the plant is in a water deficit. *Lipiec et al. (2013)* define drought as a result of water flow imbalance between evapotranspiration environmental demands and water transport in the soil-root system. The limit value for cereals such as common wheat or barley, where there is still no reduction in transpiration, is the soil moisture in the root zone at about 50–65% of the available water holding capacity of the soil (according to various authors and the growth phase of the plant). For example, *Jamieson et al. (1995)* found changes in the transpiration of barley plants with water content in the soil below 65% of the available water holding capacity. This finding was similar to *Matejka et al. (2005)* who recorded changes in the modelled evapotranspiration of the maize crop when the available water holding capacity of the soil fell below 58.2%. However, for the agriculturally intensive areas of the Czech Republic up to approx. 300 m above sea level, the characteristic long-term values of available water holding capacity are below 45%. Our previous results also show an increase in potential evapotranspiration and thus a higher susceptibility of drought in intensive agricultural areas in South and Central Moravia and Central Bohemia in the 1961–2010 period compared to the 1901–1950 average. Scenario calculations of potential evapotranspiration predict an increase in the risk of dry episodes in the Czech Republic (*Středová and Středa, 2015*).

Accurate targeting of the use of the variety to a specific area of cultivation can be a successful result. For example, deep-rooting varieties may be successful in dry years on deep soils with higher groundwater levels or sufficient water supply in the soil during winter months. However, shallow topsoil profiles of stony soils will be unsuitable for these varieties. At locations where droughts occur regularly, some strategies allow agricultural crops to survive primarily from water supplies in the soil acquired during the winter months. The occurrence of terminal drought (at the end of the growing season) is a regular phenomenon in Australia, the US and the Mediterranean. The solution may be the early varieties.

2. Material and methods

The resulting map was created based on the analysis of two raster inputs. The first data input was a layer of an average number of days with a maximum daily air temperature exceeding 25 °C in the period since the beginning of the phenophase of spring barley tillering which according to the Czech Hydrometeorological Institute (CHMI) phenological database, occurs at the site plus fifteen days from the start date. The input data for the calculation consisted of the maximum daily air temperature data for a set of technical stations (a total of 268 stations within the Czech Republic). For each station, the average date of spring barley tillering was determined from the phenological layer (for the period between 1991 to 2010 the longest comprehensive range of observations available in the Czech Republic; while we are fully aware that the period does not correspond to the period of undermentioned climatological datasets. Since the phenological observation of the CHMI were officially finished in 2010 we were facing to two, both imperfect, possible approaches in terms of length of period: either to employ the parallel phenological and climatological period 2000–2010 i.e. only 11 years, or the longest possible period i.e. for temperature and evapotranspiration from 2000–2018 and 1991–2010 for phenology i.e. around 20 years) of the beginning of spring barley tillering, and the 15-day calculation period from that date was determined. For this, for each station-specific period, the number of days with a maximum daily air temperature exceeding 25 °C was calculated for each year and station and the average annual number of days for the period 2000–2018 was calculated. These calculations resulted

in the set of 268 technical stations with an average number of days with a maximum daily air temperature exceeding 25 °C in the given phenological period for the period 2000–2018. A raster layer was created from this file using spatial statistics methods by interpolation into the Czech Republic area. The resulting raster model was subsequently processed in the ArcGIS 10.5 software, and the nearest neighbours smoothing method was applied. The raster layer was then reclassified into individual categories in a 0.5-day step, i.e. six categories ranging from < 1 to > 3.1 (Fig. 1). It is highly probable that in the areas with higher number of days with daily maximum above 25 °C also includes temperatures catching up this threshold value. Even these higher temperatures inhibit the tillering though. Linear distribution was based on the experience that relationship between air temperature and lasting at tillering phase is linear (unless the lethal temperature is reached or exceeded).

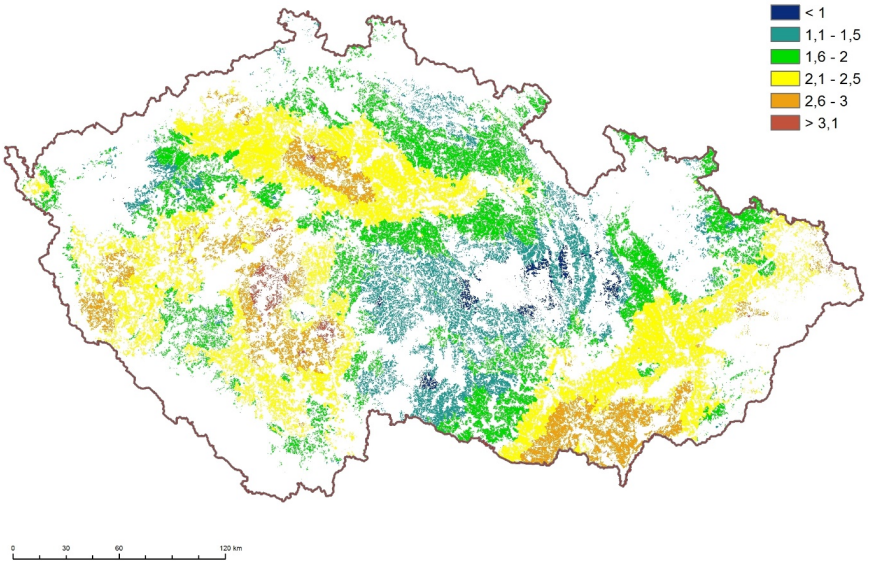

Fig. 1. Layer of the average number of days with a maximum daily air temperature exceeding 25 °C in the period since the onset of spring barley tillering phase, plus fifteen days from this start date.

The second data input was the layer of ratio of the actual evapotranspiration sum (ETa, evapotranspiration affected by the amount of water in soil) and potential evapotranspiration sum (ETp, high environmental evap-

oration and transpiration requirements) processed for the period 2000–2018 during the critical growth period of the spring barley from the beginning of the flowering phenophase to yellow ripening, which occurs at the site according to the CHMI phenological database (for the period 1991–2010; the longest available comprehensive series of observations in the Czech Republic). Input data ETa and ETp were calculated using the AVISO agrometeorological model (*Kohut et al., 2009*) from the input series of meteorological elements for stations of the CHMI station network with available measurements in the period 2000–2018. Both ETa and ETp values were calculated for spring barley. Moreover, to improve the correctness of the water abstraction intensity by evapotranspiration, for each calculation point (station), we used a specific hydro limit derived according to the available water holding capacity of soil (source: Research Institute for Soil and Water Conservation). It implicates that available water holding capacity is an integral part of the ETa parameter making our model unique, taking into account real soil conditions. Real moisture conditions in the soil profile in terms of soil parameters and evapotranspiration are reflected.

From the phenological layers, the average date of the beginning of flowering and the average date of the beginning of yellow ripening was determined for each station and a computational period was set between these dates. For this, for each station-specific period, sums ETa and ETp were calculated in individual years for the period 2000–2018. These values were then put into the sum ETa/sum ETp ratio, which is a standard index for agronomic drought identification. The resulting set of stations with the assigned value of ETa/ETp ratio in the individual years for the period 2000–2018 was created. Based on spatial statistics by interpolation into the area of the Czech Republic, annual raster layers of ETa/ETp ratio were created from this set. The resulting rasters were averaged and a raster layer of average values of the ETa/ETp ratio for the period 2000–2018 was created. The resulting raster model was subsequently processed in the ArcGIS 10.5 software, and the nearest neighbour smoothing method was used. The raster layer of ratio values was then reclassified into individual categories in a step of 0.04, i.e. six categories from 6 to 1 for the value of categories from < 0.76 to > 0.92 (Fig. 2), since in this particular case the linear impact on possible yield reduction is apparent. The number of categories (i.e. six) corresponds to number of drought categories (expressed as % of available water holding

capacity) of the CHMI, however regarding to constriction of ETa/ETp ratio there are apparent differences from simple drought evaluation used by CHMI. Our complex and wiser index though better reflects real demands and impacts of the plants.

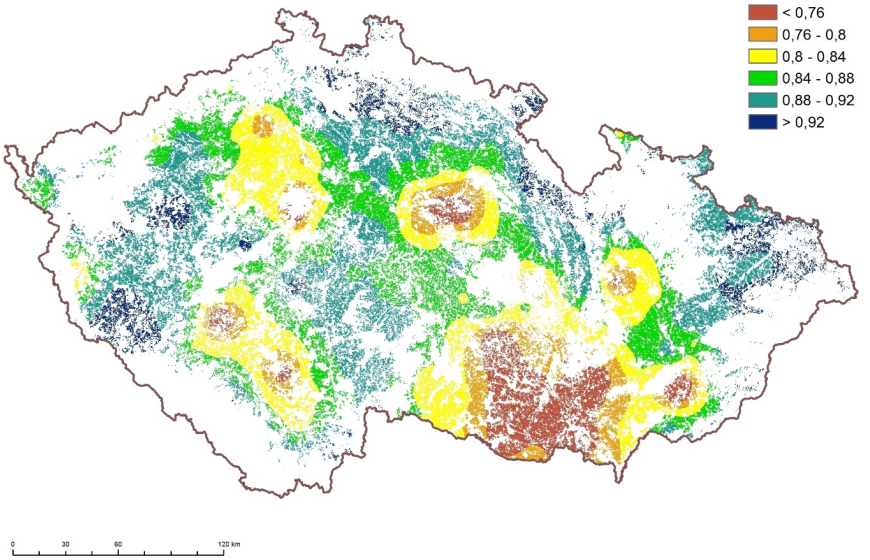

Fig. 2. Layer of the ratio of the actual evapotranspiration sum (ETa) and the potential evapotranspiration sum (ETp) for the period 2000–2018 during flowering to yellow ripening of spring barley.

Both partial raster layers (number of days category layer and ETa/ETp ratio category layer) were then summed, and the resulting sum total of the raster layer was again divided into six risk categories. The raster layer was converted to polygons and only areas under arable land (arable land layer; source: Research Institute for Soil and Water Conservation.) and at an altitude of 600 m above sea level (we do not expect intensive cultivation of spring malting barley at a higher altitude) were selected. The resulting map output was also created in ArcGis 10.5 software.

3. Results and discussion

Climate change in Europe since 1990 has been unfavourable for cereals yields because of heat stress during grain filling and drought during stem elonga-

tion (*Brisson et al., 2010*). The severity of the effects of drought increases with the prolongation of its exposure during the growing season and its occurrence at critical stages of plant development. For example, flowering and the early stage of ripening are critical for cereals. The occurrence of drought during sowing and the vegetative phases of cereal growth, as well as the high temperatures at this stage, have an impact on the emergence of the crop and the consequent reduction of tillers. The effect of drought during generative phases results in a reduction in the number of spiked seeds and grains. Flowering is a critical period when water scarcity has a worse impact than at other stages of development. Another critical period is the start of grain formation, where the number of cells in the endosperm is decided. In the grain filling phase, water stress interferes with the synthesis and storage of starch and storage proteins.

In our previous work, we evaluated the moisture conditions during the vegetation period (91–180 days of the year) for the period 1975–2007 and its influence on the production of spring barley. A long-term trend of decreasing soil water supply was found in 20 out of 21 localities, expressed as % of available water holding capacity. At the same time, a statistically significant correlation was found between the yield of spring barley grain and the state of soil saturation with water, expressed in terms of the current state of % of available water holding capacity.

Mužíková et al. (2013) evaluated yields of spring barley and fluctuations in soil moisture in the critical period in terms of barley yield in the Czech Republic for the period 1975–2010. On most sites, there were statistically significant relationships between grain yield and soil moisture in different stages of vegetation. A statistically significant relationship was also found when evaluating average values of soil moisture and the average grain yield across stations. When evaluating the season-average soil moisture and yield, these researchers found a statistically significant to a highly significant year effect (1976, 1981, 1985, 1986, 1995, 1996, 2000, 2004, 2007, 2009 and 2010). In the last decade, the number of growing seasons with a demonstrable influence of moisture conditions on barley yield increased in different production areas.

Spring barley grain yields and values of the effective drought index (EDI) in the critical period in terms of yield formation of spring barley in the Czech Republic were evaluated for the period 1975–2015 (*Slabá et al., 2017*). In

most areas, there were statistically significant relationships between grain yield and the EDI in different stages of vegetation (fourth and sixth decade of the vegetation primarily).

The aim of the analysis and mapping of the outcomes was to define areas with increased risk of main abiotic stressors occurrence during the critical growth and development phase of spring barley vegetation (high temperatures during tillering and drought from flowering to hard dough growth stage) in the territory of the Czech Republic (Fig. 3). Analyses were based on a sophisticated synthesis of the long-term a) meteorological datasets, b) phenological datasets, c) soil conditions data (available water holding capacity of Czech soils), d) land-use data, and e) the arable land category and maximum 600 m a.s.l. The current findings illustrate that 49% of the potentially usable areas of spring barley are categorised as risky (with varying degrees of risk).

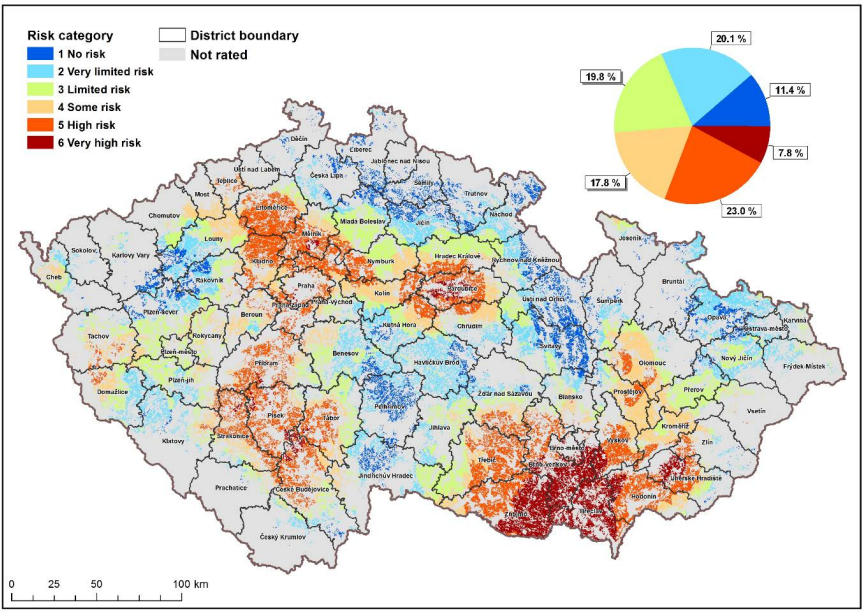

Fig. 3. The categorisation of the territory of the Czech Republic according to the risk of occurrence of abiotic stressors for spring barley.

Per the research priorities of the Ministry of Agriculture for the period 2017–2025, the map provides partial information for the optimisation of crop

representation in each locality, organisation and optimisation of farming practices, use of minimisation and soil conservation technologies for better soil retention, utilisation of varieties tolerant to drought, and the potential for using an effective irrigation system at the time when plants need water the most.

4. Summary

Increasing climate variability and increasing frequency of abiotic stressors, especially drought, also result in a decrease in spring barley grain yield as well as quality by increasing the nitrogen content. In the Czech Republic, these problems are most pronounced in traditional areas of spring barley cultivation. Predictions of future climate developments suggest an increased likelihood of the occurrence of episodes unfavourable for plant production, such as dry and very warm seasons. As a short growing time and small root system, spring barley will be severely affected by these problematic episodes and is already considered a risky crop.

Drought can have various impacts on different agricultural crops, based on time of occurrence, the monitored crop and stage of its growth etc. Therefore, the methods of drought evaluation can differ greatly, and their outcomes can thus vary as well. A simple evaluation of precipitation totals is not a sufficient indicator of moisture conditions. For the exact evaluation of moisture conditions, it is advisable to use a costly direct stand microclimatic monitoring. Hence, it is necessary to use sophisticated models concerning a wide range of meteorological elements and biological characteristics of the monitored crop in order to objectively evaluate the moisture conditions in the soil-plant-atmosphere system.

The number of growing seasons with the proven effect of moisture conditions on barley yield in various production areas has increased in the last decade. These outputs demonstrate the possibility of using commonly available data sources in combination with the application of sophisticated computational methods. Their effective combination brought interesting results for the state administration, agricultural research as well as agricultural practice. The aforementioned technique is an elegant alternative to climate monitoring and costly dedicated field experiments.

The innovative aspect of the method lies in the categorisation of the territory of the Czech Republic according to the risk of occurrence of main abiotic stressors affecting spring barley. The resulting maps also define areas that appear to be less risky on standard maps as at risk; however, depending on actual precipitation, these areas correspond to areas of spring barley with significantly reduced grain yield in recent years. The map, therefore, forms a basis for spring barley cultivation targeted for relevant features and the regionalisation of varieties.

Acknowledgements. This research was supported financially by the National Agency of Agricultural Research Ministry of Agriculture (project Nos. QK1910197 and QK1920280).

References

Blum A., 2005: Drought resistance, water-use efficiency, and yield potential—are they compatible, dissonant, or mutually exclusive? Aust. J. Agr. Res., **56**, 11, 1159–1168, doi: 10.1071/AR05069.

Blum A., 2011: Plant Breeding for Water – Limited Environments. Springer – Verlag New York, 255 pp.

Bodner G., Nakhforoosh A., Kaul H.-P., 2015: Management of crop water under drought: a review. Agron. Sustain. Dev., **35**, 2, 401–442, doi: 10.1007/s13593-015-0283-4.

Boyer J. S., 1982: Plant productivity and environment. Science, **218**, 4571, 443–448, doi: 10.1126/science.218.4571.443.

Brisson N., Gate P., Gouache D., Charmet G., Oury F.-X., Huard F., 2010: Why are wheat yields stagnating in Europe? A comprehensive data analysis for France. Field Crops Res., **119**, 1, 201–212, doi: 10.1016/j.fcr.2010.07.012.

Chaves M. M., Costa J. M., Saibo N. J. M., 2011: Recent advances in photosynthesis under drought and salinity. Adv. Bot. Res., **57**, 49–104, doi: 10.1016/B978-0-12-387692-8.00003-5.

Du S., Wang Y. L., Kume T., Zhang J. G., Otsuki K., Yamanaka N., Liu G. B., 2011: Sapflow characteristics and climatic responses in three forest species in the semi-arid Loess Plateau region of China. Agric. For. Meteorol., **151**, 1, 1–10, doi: 10.1016/j.agrformet.2010.08.011.

Friend D. J. C., 1966: The effects of light and temperature on the growth of cereals. In: Milthorpe F. L., Ivins J. D. (Eds.): The growth of cereals and grasses. Butterworths, London, United Kingdom, pp. 181–199.

Jamieson P. D., Francis G. S., Wilson D. R., Martin R. J., 1995: Effects of water deficits on evapotranspiration from barley. Agric. For. Meteorol., **76**, 1, 41–58, doi: 10.1016/0168-1923(94)02214-5.

Kohut M., Rožnovský J., Chuchma F., 2009: The long-term soil moisture reserve variability in the Czech Republic based on the AVISO model. Sustainable Development and Bioclimate, Stará Lesná, Slovakia. Slovak Academy of Sciences: Bratislava, 160–161.

Křen J., Klem K., Svobodová I., Míša P., Lukas V., 2015: Influence of sowing, nitrogen nutrition and weather conditions on stand structure and yield of spring barley. Cereal Res. Commun., **43**, 2, 326–335, doi: 10.1556/CRC.2014.0036.

Lipiec J., Doussan, S., Nosalewicz A., Kondracka K., 2013: Effect of drought and heat stresses on plant growth and yield: a review. Int. Agrophys., **27**, 4, 463–477, doi: 10.2478/intag-2013-0017.

Matejka F., Hurtalová T., Rožnovský J., Chalupníková B., 2005: Effect of soil moisture on evapotranspiration of a maize stand during one growing season. Contributions to Geophysics and Geodesy, **35**, 3, 219–228.

Mužíková B., Středa T., Krmelová P., Dvořáčková O., 2013: Yields of spring barley in the climatic conditions of the Czech Republic. Kvasný Průmysl, **59**, 12, 352–357, doi: 10.18832/kp2013038.

Naithani K. J., Ewers B. E., Pendall E., 2012: Sap flux-scaled transpiration and stomatal conductance response to soil and atmospheric drought in a semi-arid sagebrush ecosystem. J. Hydrol., **464–465**, 176–185, doi: 10.1016/j.jhydrol.2012.07.008.

Rawson H. M., 1971: Tillering patterns in wheat with special reference to the shoot at the coleoptile node. Aust. J. Biol. Sci., **24**, 4, 829–842, doi: 10.1071/BI9710829.

She D., Xia Y., Shao M., Peng S., Yu S., 2013: Transpiration and canopy conductance of Caragana korshinskii trees in response to soil moisture in sand land of China. Agrofor. Syst., **87**, 3, 667–678, doi: 10.1007/s10457-012-9587-4.

Škvarenina J., Tomlain J., Hrvol J., Škvareninová J., Nejedlík P., 2009: Progress in dryness and wetness parameters in altitudinal vegetation stages of West Carpathians: Time-series analysis 1951–2007. Idojárás, **113**, 1-2, 47–54.

Slabá V., Procházková P., Středa T., 2017: Relationship between barley yield and annual precipitation conditions. MendelNet 2017: Proceedings of International PhD Students Conference. Brno: Mendel University in Brno, 2017, 132–136.

Středová H., Středa T., 2015: Agroclimatic conditions of the Czech Republic – development and influence on agricultural production. Seed and seedlings. Prague. Czech University of Life Sciences Prague, 22–27.

Tanaka R., Nakano H., 2019: Barley yield response to nitrogen application under different weather conditions. Sci. Rep., **9,** 8477, doi: 10.1038/s41598-019-44876-y.

Zeppel M. J. B., Macinnis-Ng C. M. O., Yunusa I. A. M., Whitley R. J., Eamus D., 2008: Long term trends of stand transpiration in a remnant forest during wet and dry years. J. Hydrol., **349**, 1-2, 200–213, doi: 10.1016/j.jhydrol.2007.11.001.

Contributions to Geophysics and Geodesy Vol. 50/1, 2020 (61–81)

Crustal deformation analysis in Zagros and Makran zones, based on GPS permanent network data

Seyed Reza SAKHAEI*, Ghasem Ghorbani ROSTAM

Department of Physics, Sciences Faculty, Islamshahr Branch, Islamic Azad University, Islamshahr, Iran

Abstract: We present an analysis of strain based on the evaluation of crustal deformation in Zagros and Makran, which has implications in terms of the dynamics of the study area. We have used data from 17 permanent GPS stations of the Cartographic Centre of Iran spanning the period 2011–2013. The raw observed data were in RINEX format. The elements of strain tensor were calculated by a 2D isoparametric method and the inversion of strain equation. Then the dilatation (extension and compression) and shearing were obtained through the analysis of eigenvalue and eigenvector of tensors. In most cases compression has overcome the extension, which can be expected due to the convergence of the Arabia and Eurasia plates. The compression axis is nearly vertical along the Zagros causing reverse and thrust faults in Zagros. Due to the N–S trending of the Sabzvaran–Jiroft–Kahnuj fault system and to the direction of compression and extension, the system will be of strike–slip mechanism. Sudden changes of shearing can be used to identify the strike–slip faults. As observed in this study, there were sudden changes in shearing of the Rafsanjan and Jiroft–Kahnuj faults. The P/T axis rotates significantly in the Zagros–Makran transition zone. Moreover, the Makran's P/T axis is smaller than the P/T axis of Zagros, which demonstrates that the impact of the Arabian plate, moving towards Iran, is greater than the impact of the Indian subcontinent plate movement. The values of the counter-clockwise rotation rate at stations located east of the Zagros–Makran transition zone are higher than at other stations. Also the velocity vectors at stations were determined while using the software GAMIT/GLOBK.

Key words: crustal deformation analysis, strain, Zagros, Makran

1. Introduction

Iranian plateau as an active seismically area is located in the Alpine-Himalayan belt. Accumulation of forces in Iran is through the Arabian plate moving toward north-east and the Indian subcontinent moving toward the

*corresponding author: e-mail: reza.sakhaei@srbiau.ac.ir

doi: 10.31577/congeo.2020.50.1.4

north, which caused a seismic area. Understanding the elastic properties of the studying area and providing related seismotectonic model, are possible through the studying and understanding the basic parameters such as stress and strain fields of study area. In many studies, geodetic observations are used to determine the pattern of regional strain rate. *Shen et al. (1996)*, *Cai and Grafarend (2007)*, used a technique known as discretization. In the other way, inversion technique is used to determine the strain field (*Spakman and Nyst, 2002*). *Allmendinger et al. (2007)* used the nearest neighbour and weighted distance methods, to obtain the velocity fields.

The study area is one of the most complex tectonic regions of Iran (Figs. 1 and 2). Through the convergence of Arabia and Eurasia plates two different oceanic subduction zone (Makran) and collision zone (Zagros) in the south and southwest of Iran were created. In this research studying the crustal deformation of the Zagros and Makran through using the data recorded in 17 GPS permanent network stations (Fig. 1, Table 1) will be investigated. The contour map of results will be drawn and also the obtained results will be compared with the regional stress field and focal mechanisms of occurred earthquakes.

Table 1. Location of GPS permanent stations in this region.

Station name	**Latitude (° N)**	**Longitude (° E)**	**Height (m)**
ABDN	30.37783	48.21347	−12.98
ANGN	26.45720	57.89737	718.32
BAFT	29.23915	56.58001	2275.75
BEBN	30.60564	50.21693	301.98
BRBS	27.20722	56.32058	4.75
CHBR	25.27058	60.65112	−19.73
DBST	29.23770	57.33018	2633.19
FDNG	30.82442	55.80831	1351.64
FHRJ	28.93733	58.88126	666.71
GLMT	27.48215	59.44850	363.14
JASC	25.63752	57.76989	−19.14
LAMD	27.36365	53.20334	380.79
MHAN	30.07158	57.28836	1873.25
SBAK	30.14615	55.10749	1857.43
SHRZ	29.54436	52.60258	1476.69
ZABL	30.84127	61.71591	1152.28
ZRND	30.83319	56.60769	1752.83

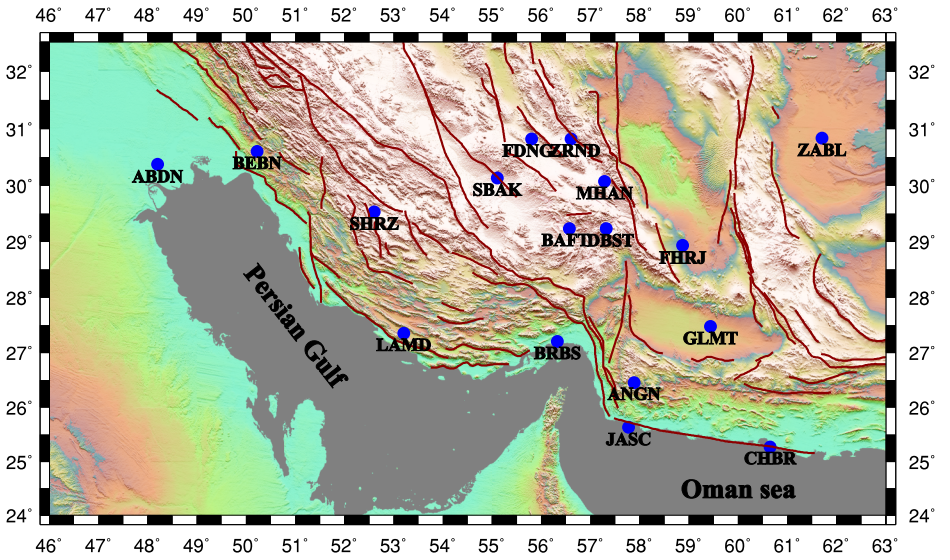

Fig. 1. Location of GPS permanent stations in south of Iran. The red lines represent main faults in this study area.

2. Tectonic setting

In the Strait of Hormuz in south of Iran (26.5° N and 56.5° E), the Arabian plate at avelocity of 23–25 mm/yr (measured by GPS), converges with Eurasia (*Bayer et al., 2003; McClusky et al., 2003; Vernant et al., 2004; Masson et al., 2007*). Due to convergence of Arabia and Eurasia plates, two different zones have been created: continental collision (Zagros) and oceanic subduction (Makran) in the West and the East Strait of Hormuz, respectively. The continental part of Arabian plate and Eurasian plate have collided together and created Zagros fold and thrust belt with NW–SE trending. The East part of Arabian plate underthrusted to Iran plate and consequently the vast Makran accretionary wedge shaped with east-west trending (*Byrne et al., 1992; McCall, 1997*).

The shortening rate of Zagros is obtained about 10 mm/yr with GPS measurement (*Tatar et al., 2002, Vernant et al., 2004; Hessami et al., 2006*). The total amount of shortening, in some studies is about 50 km (*Molinaro et al., 2005*) and according to other studies, it is estimated about 85 km (*McQuarrie, 2004*). Zagros is very active in terms of seismicity. More than

50 percent of Iran's earthquakes which has been recorded by the global networks have occurred in Zagross (*Mirzaei et al., 1998*). Sudden change of seismicity can be seen from the severe seismicity in Zagros to partial rest in the West of Makran (*Jackson and Mckenzie, 1984*).

The rate of convergence in the Makran increases from West (36.5 mm/yr in the western border) to East (42 mm/yr in the eastern border) (*Demets et al., 1990; Zarifi, 2006*). The rate of convergence in the Zagros is increased from Northwest to the Northeast. The rate of convergence in the transition from the Zagros collision zone to the Makran subduction zone, changes from 9±2 mm/yr to 19±2 mm/yr (*Vernant et al., 2004; Masson et al., 2007*).

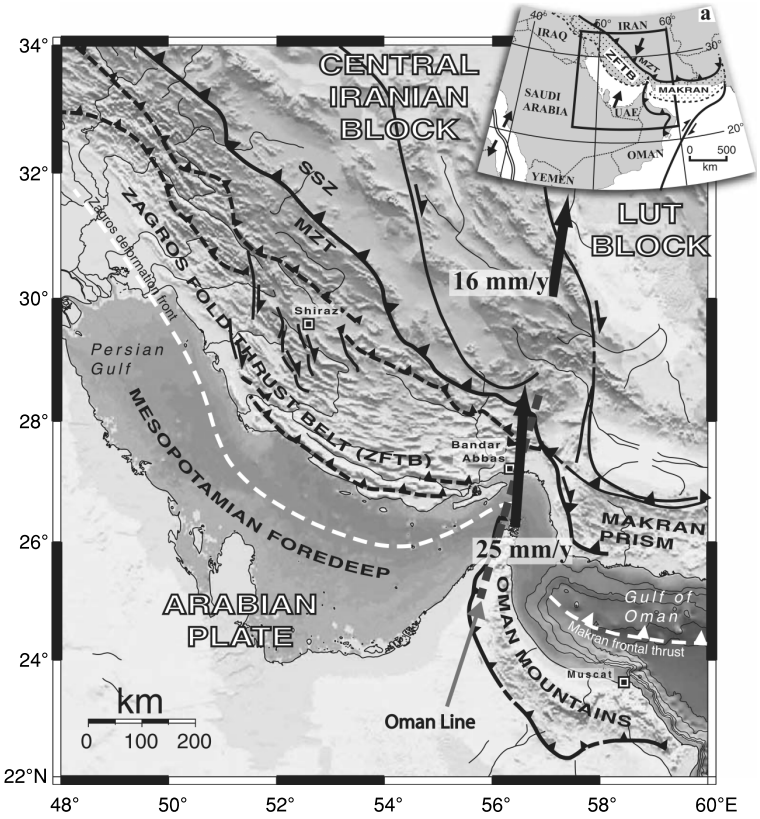

Fig. 2. Map of South Iran–North Arabia (*Regard et al., 2010*). The arrows represent the velocity relative to Eurasia (*Vernantet al., 2004*). MZT: Main Zagros Thrust; SSZ: Sanandaj–Sirjan Zone.

3. Determination of velocity vectors related to Eurasia and North Arabian plates

Velocity vectors related to a fixed reference is interesting in geodesy. As discussed in section 2 (tectonic settings), the study area is influenced by the convergence of two plates. Therefore, the velocity vectors of the region relative to the two plates are investigated. The magnitude and azimuth of velocity vector for each GPS station is calculated by well-known GAMIT/GLOBK software related to Eurasia and North Arabian plates. To determine these vectors which are related to Eurasian plate, three IGS stations (TASH, POL2, KIT3) are considered as fix points and reference frame. This work is done also for North Arabian plate with four stations (HALY, RAMO, DRAG, BSHM) (Figs. 3 and 4). The magnitude and azimuth of velocity vectors are shown in Tables 2 and 3 (Figs. 5–8). V_E and V_N represent velocity vectors in East–West and North–South directions, respectively. $\pm V_E$ and $\pm V_N$ represent errors of velocity calculation. The maximum magnitude of velocity vector was observed in station BRBS with

Table 2. Azimuth and magnitude of velocity vector related to the Eurasia.

Station name	$\mathbf{V_E}$ **(mm/yr)**	$\mathbf{V_N}$ **(mm/yr)**	$\pm\ \mathbf{V_E}$ **(mm/yr)**	$\pm\ \mathbf{V_N}$ **(mm/yr)**	**Magnitude (mm/yr)**	**Azimuth (deg)**
ABDN	26.07	31.78	0.94	1.44	41.10	39.38
ANGN	32.03	18.40	1.22	0.67	36.94	60.15
BAFT	28.33	20.53	0.92	0.68	34.99	54.10
BEBN	23.52	28.72	0.87	1.21	37.12	39.33
BRBS	32.56	28.42	1.21	0.79	43.22	48.91
CHBR	31.25	9.75	1.23	0.58	32.74	72.71
DBST	33.13	16.48	0.98	0.72	37.00	63.58
FDNG	19.92	9.40	0.90	0.85	22.03	64.77
FHRJ	31.74	11.64	1.02	0.71	33.81	69.90
GLMT	31.91	11.13	1.13	0.59	33.80	70.81
JASC	29.15	17.17	1.29	0.64	33.83	59.53
LAMD	28.52	25.96	1.31	1.08	38.57	47.71
MHAN	29.42	20.89	0.83	0.64	36.08	54.65
SBAK	26.81	20.83	0.85	0.78	33.95	52.18
SHRZ	25.7	21.83	0.95	0.98	33.72	49.68
ZABL	30.57	9.16	0.62	0.35	31.91	73.36
ZRND	27.38	19.60	0.79	0.70	33.67	54.43

Table 3. Azimuth and magnitude of velocity vector related to the North Arabian plate.

Station name	V_E (mm/yr)	V_N (mm/yr)	$\pm V_E$ (mm/yr)	$\pm V_N$ (mm/yr)	Magnitude (mm/yr)	Azimuth (deg)
ABDN	30.37	37.65	0.5	0.72	48.37	38.89
ANGN	50.42	40.88	1.34	1.58	64.91	50.97
BAFT	38.74	41.63	1.20	1.28	56.87	42.94
BEBN	28.01	38.05	0.61	0.81	47.25	36.36
BRBS	47.95	48.02	1.21	1.42	67.86	44.96
CHBR	55.06	37.75	1.63	1.91	66.76	55.57
DBST	43.94	39.16	1.34	1.38	58.86	48.29
FDNG	26.01	29.47	1.22	1.25	39.31	41.43
FHRJ	44.26	37.71	1.53	1.54	58.15	49.57
GLMT	48.73	37.77	1.57	1.67	61.65	52.22
JASC	49.56	38.85	1.29	1.62	62.97	51.91
LAMD	41.45	39.35	0.98	1.23	57.15	46.49
MHAN	38.08	43.85	1.29	1.30	58.08	40.97
SBAK	34.25	39.22	1.06	1.14	52.07	41.13
SHRZ	33.40	35.08	0.80	0.98	48.44	43.60
ZABL	39.42	42.52	1.81	1.56	57.98	42.83
ZRND	33.77	41.31	1.24	1.24	53.36	39.27

values 43.22 and 67.86 mm/yr related to the plates of Eurasia and North Arabian, respectively. And the minimum magnitude of velocity vector was obtained in station FDNG with values 22.03 and 39.31 mm/yr related to the plates of Eurasia and North Arabian, respectively. In the convergence with the Eurasia plate, ZABL and BEBN stations have the highest (73.36°) and the lowest (39.33°) azimuth, respectively. Also, CHBR and BEBN stations have the highest (55.57°) and the lowest (36.36°) Azimuth in divergence with the Northern Arabian Plate, respectively. The average error in the calculation of the velocity vector of the Eurasian and North Arabia has been set 0.92 and 1.31 mm/yr, respectively.

4. Strain analysis

In this study, the 2-D isoparametric method is used to obtain the strain tensor. This method utilizes the relative distance analysis between a point and its adjacent area before and after deformation and acquires a strain tensor for each point (GPS station). Mathematically, the strain is the gra-

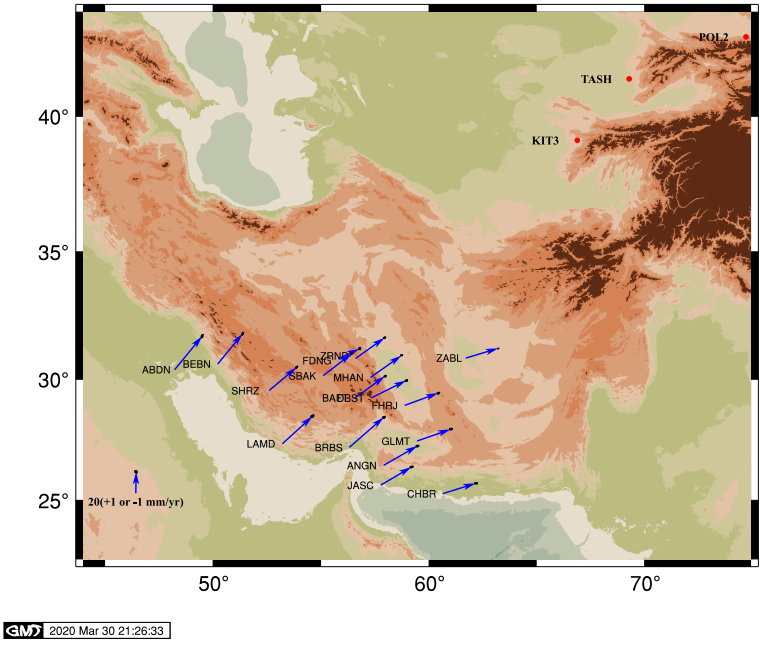

Fig. 3. Velocity vectors related to the Eurasia plate. Red circles are reference stations in the Eurasia plate.

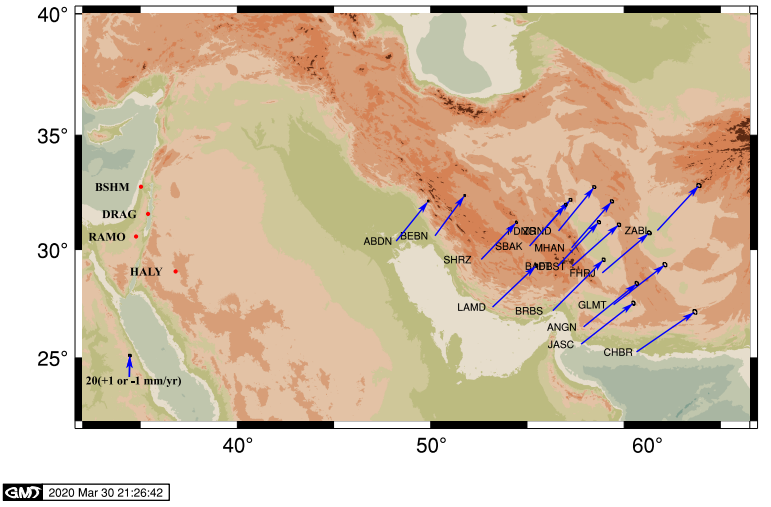

Fig. 4. Velocity vectors related to the North Arabian plate. Red circles are reference stations in the North Arabian plate.

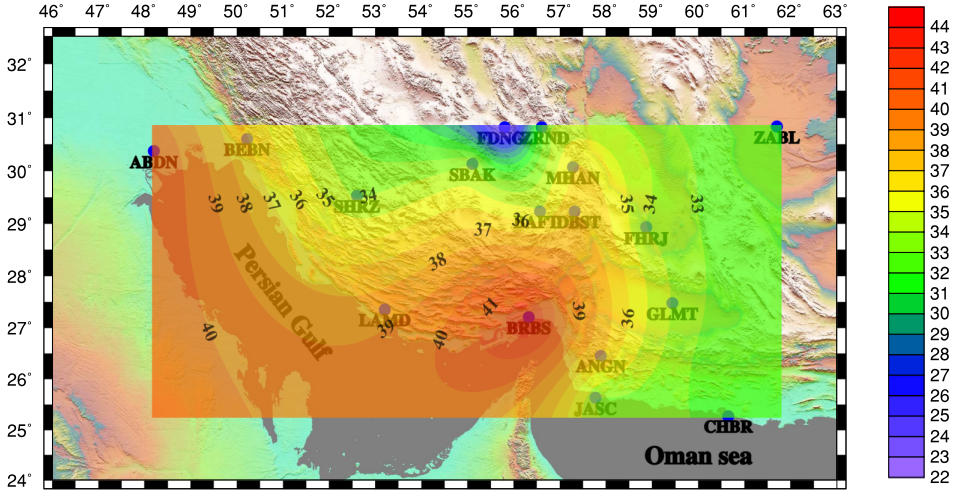

Fig. 5. Contour map of magnitude of velocity vectors related to the Eurasia plate (mm/yr).

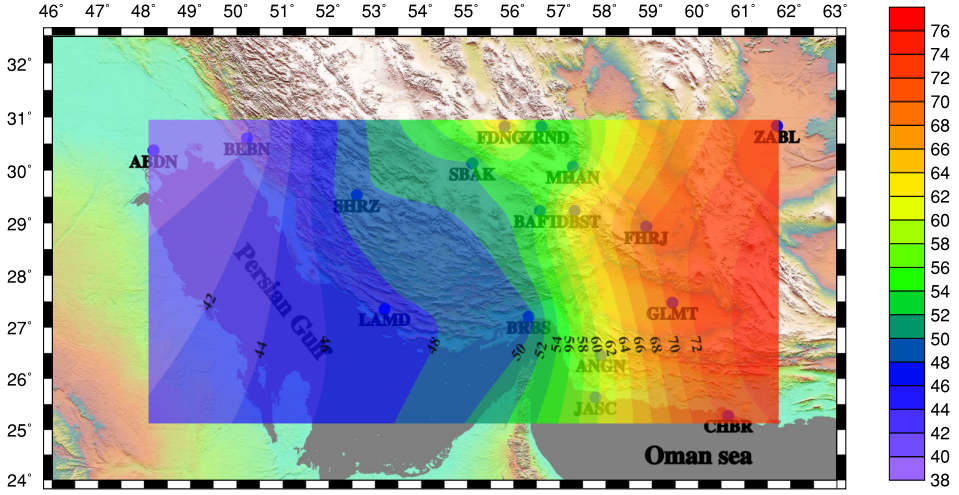

Fig. 6. Contour map of azimuth of velocity vectors related to the Eurasia plate (deg).

dient of the displacement field, that is, the displacement of two points at a differential distance. In the study of deformation using strain calculations, because the dependence on the coordinate system is eliminated, its results can be trusted more than other methods (*Vanicek and Krakiwsky, 1986*).

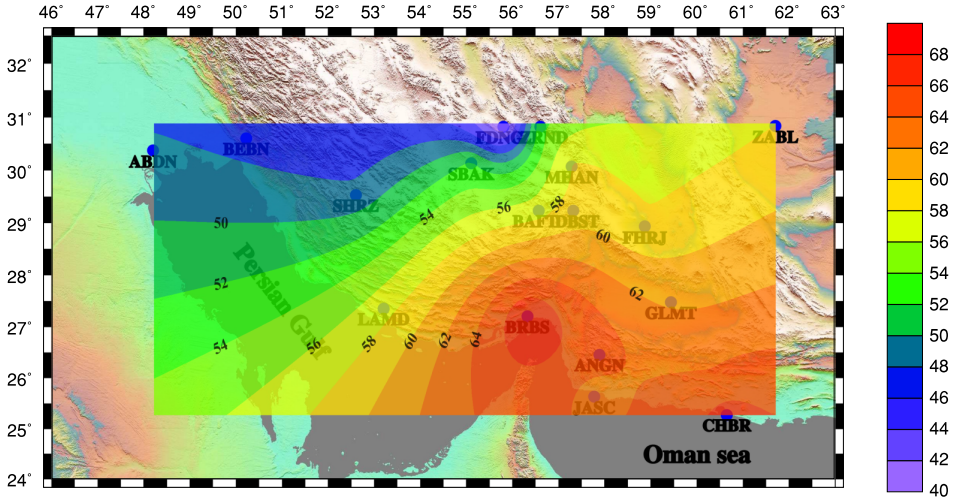

Fig. 7. Contour map of magnitude of velocity vectors related to the North Arabian plate (mm/yr).

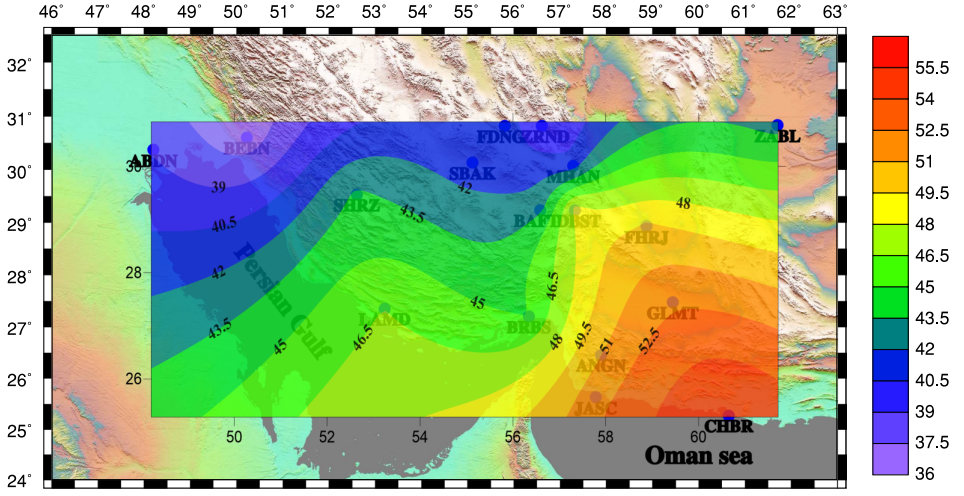

Fig. 8. Contour map of azimuth of velocity vectors related to the North Arabian plate (deg).

We consider two adjacent points of $\underline{a}$ and $\underline{b}$, so that their positions in the two-dimensional coordinate system before and after deformation are (x, y) and $(x + x', y + y')$, respectively. If the vector displacement of point

$\underline{a}$ caused by deformation, is (u, v), then the displacement vector of point $\underline{b}$ can be written in the form of $(u + u', v + v')$. Values of u' and v' by using Taylor expansion and elimination of higher order sentences are calculated as follows:

$$u' = e_{xx}\, x' + \frac{1}{2}\gamma_{xy}\, y' - \omega\, y'\,, \tag{1}$$

$$v' = \frac{1}{2}\gamma_{xy}\, x' + e_{yy}\, y' + \omega\, x'\,, \tag{2}$$

where:

$$e_{xx} = \frac{\partial u}{\partial x}\,, \quad e_{yy} = \frac{\partial v}{\partial y}\,, \quad \gamma_{xy} = \gamma_{yx} = \frac{\partial u}{\partial y} + \frac{\partial v}{\partial x}\,, \quad \omega = \frac{1}{2}\left(\frac{\partial v}{\partial x} - \frac{\partial u}{\partial y}\right), \tag{3}$$

In this equation e_{xx}, e_{yy}, γ_{xy} and γ_{yx} are elements of strain matrix.

To calculate the elements of strain matrix, we can use equations of the lengths of two adjacent points (before and after of deformation) and eliminating the sentences containing the second power and by multiplying derivations at each other:

$$\varepsilon = e_{xx}\cos^2\alpha + \gamma_{xy}\sin\alpha\cos\alpha + e_{yy}\sin^2\alpha\,, \tag{4}$$

where the angle between the vector of r and x-axis is called α.

The amount of ε is determined by calculating the difference between the displacement of two points before and after deformation. Finally, by knowing the angle α and strain ε we will find three unknown parameters that are strain matrix elements. Since we measure the displacement in relation to several adjacent stations for any stations, so the relationship (4) can be written in matrix form $d = Gm$, where d is called a data matrix or the information. Also, the matrix G is a matrix from the order of $i * 3$ (i = number of station). If i equals 3, we have three equations with three unknown parameters. And if you have more than three stations, the problem will be solved by using generalized linear inversion (*Lay and Wallace, 1995*):

$$m = (G^T G)^{-1} G^T d\,. \tag{5}$$

To find the directions of maximum and minimum extensions, we can derive the equation (4) to α and equal it to zero. Directions that satisfy the following relation are the maximum and minimum angles of extension and their values are eigenvalues of strain tensor (λ_{max}, λ_{min}):

$$\tan 2\alpha = \frac{\gamma_{xy}}{e_{xx} - eyy}\,. \tag{6}$$

Through splitting the strain tensor into two symmetric and antisymmetric parts, it can be written as:

$$\varepsilon = \frac{1}{2}(\varepsilon + \varepsilon^T) + \frac{1}{2}(\varepsilon - \varepsilon^T) = \varepsilon_s + \varepsilon_{as}\,, \tag{7}$$

where ε_s and ε_{as} are symmetric strain tensors (represent deformation of the object) and antisymmetric strain tensor (represents rotation of the object), respectively.

$$\varepsilon_s = \begin{bmatrix} e_{xx} & \frac{1}{2}(e_{xy} + e_{yx}) \\ \frac{1}{2}(e_{yx} + e_{xy}) & e_{yy} \end{bmatrix}, \tag{8}$$

$$\varepsilon_{as} = \begin{bmatrix} 0 & -\frac{1}{2}(e_{yx} - e_{xy}) \\ \frac{1}{2}(e_{yx} - e_{xy}) & 0 \end{bmatrix}. \tag{9}$$

Moreover, by defining two quantities of elongation (Δ) and shearing (γ) we can interpret a more tangible to the strain in the desired station:

$$\Delta = \lambda_{max} + \lambda_{min} = e_{xx} + e_{yy}\,, \tag{10}$$

$$\gamma = \lambda_{max} - \lambda_{min} = \sqrt{(e_{xx} - e_{yy})^2 + 4e_{xy}^2}\,. \tag{11}$$

Positive and negative values of elongation are referred to as expansion (stretching) and contraction (compression) of surface, respectively. Shearing gives maximum amount of change in direction, which is non-isotropic deformation property.

4.1. Calculation of strain tensor

To determine the strain tensor in each GPS permanent station in the south of Iran (around Zagros and Makran), the observed raw data (position) were used in the RINEX (Receiver Independent Exchange) format from 2011 to 2013. RINEX is a data interchange format for raw data (usually position and speed) that allows the user to post-process the received data to produce a more accurate result. To determine the coordinates of stations, the data

processed in NGS site (`http://www.ngs.noaa.gov/OPUS/`). The On-line Positioning User Service (OPUS) allows users to submit their GPS data files (for each selected day) to NGS, where the data are processed to determine position coordinates using NGS computers and software. OPUS is based on the average of three distinct single-baseline solutions computed using double-differenced, dual-frequency carrier-phase measurements using PAGES software. The selected Continuously Operating Reference Stations (CORS) sites may not be the nearest to the user location but are chosen by a few criteria, such as: distance, number of observations, site stability, etc. A good OPUS run is defined as a solution which used 90 percent or more of the observations, fixed at least 50 percent of the ambiguities, and the overall RMS did not exceed 3 cm. The estimated position is reported back to the user via email in International Terrestrial Reference Frame (ITRF) coordinate systems (*Kashani et al., 2008*). On the other hand, we know that ITRF uses the IGS reference stations (with a certain location). Then, the OPUS results (position for each day) are used as input data and the strain tensors were calculated by using the above formulas. We obtained the strain with the displacement of the points at the beginning and end of the time period. To avoid possible positioning errors, we used an average of 3 to 5 days (for each station) at the beginning and the end. The elements of strain tensors and distance between GPS stations and IGS reference stations are represented in Table 4.

Table 4. Elements of strain tensor (μ-strain/year) and distance with IGS stations.

Station name	e_{xx}	e_{xy}	e_{yy}	**IGS Reference stations**	**Distance (km)**
ABDN	0.0331	0.0677	0.0148	ISKU	328.178
				ISNA	410.024
				ISBA	485.219
ANGN	0.0070	−0.0351	−0.0125	TEHN	1198.360
				ISKU	1346.579
				ISBA	1501.967
BAFT	0.0713	0.0440	−0.0101	YILB	782.389
				TEHN	868.760
				ISKU	1116.015
BEBN	0.0337	0.0683	−0.0103	ISKU	468.267
				TEHN	574.096
				ISBA	624.393

Table 4. Continued from the previous page.

Station name	e_{xx}	e_{xy}	e_{yy}	IGS Reference stations	Distance (km)
BRBS	−0.0059	−0.0591	−0.0530	YILB	556.369
				ISBS	906.715
				TEHN	1052.412
CHBR	0.0164	−0.0140	−0.0079	TEHN	1455.971
				KIT3	1639.252
				ISKU	1647.212
DBST	0.0710	0.1811	0.0595	TEHN	910.576
				ISKU	1157.674
				ISBA	1305.913
FDNG	0.1055	−0.0329	−0.3117	TEHN	682.170
				ISKU	965.217
				ISBA	1107.170
FHRJ	0.0105	−0.0621	−0.0281	YILB	797.384
				TEHN	1031.264
				ISBS	1084.635
GLMT	−0.0080	−0.0174	−0.0083	TEHN	1190.221
				ISBS	1181.107
				ISKU	1424.556
JASC	0.0363	−0.0461	−0.0673	YIBL	417.744
				ISKU	1386.915
				ISBA	1543.421
LAMD	0.0394	0.0289	−0.0461	ISKU	912.130
				TEHN	940.121
				ISER	1303.952
MHAN	−0.0103	0.0195	0.0553	TEHN	935.694
				ISKU	1123.880
				ISNA	1250.794
SBAK	0.0211	−0.0553	−0.1427	TEHN	709.274
				ISKU	921.780
				ISBA	1069.495
SHRZ	−0.0038	−0.0476	−0.0633	ISBS	475.270
				ISKU	726.350
				ISNA	834.942
ZABL	−0.0106	−0.0362	−0.0007	KIT3	1032.549
				TEHN	1104.921
				ISKU	1514.722
ZRND	0.0561	−0.0747	−0.1051	TEHN	729.206
				ISKU	1039.213
				ISBA	1179.708

4.2. Calculation of dilatation and shearing

By analysis of eigenvalues and eigenvectors of matrix, we will achieve some important results. Summation and minus of the maximum and the minimum of eigenvalues are dilatation and shearing in each station, respectively. Moreover, eigenvalues determine direction of stretching and compression (Fig. 11). These values were calculated for the study of the study area and are represented in Table 5. Maximum compression (negative dilatation) and maximum stretching (positive dilatation) are -0.2062×10^{-6} and 0.1305×10^{-6} in the stations FDNG and DBST, respectively. Maximum and minimum shearing are also obtained in the stations FDNG and GLMT with values of 0.4224×10^{-6} and 0.0349×10^{-6}, respectively. Figs. 9 and 10 represent contour maps of dilatation and shearing.

Table 5. Eigenvalue, dilatation and shearing in the each stations (μ-strain/year).

Station name	l_max	l_min	Dilatation	Shearing
ABDN	0.0923	−0.0444	0.0479	0.1367
ANGN	0.0337	−0.0392	−0.0055	0.0729
BAFT	0.0905	−0.0293	0.0612	0.1198
BEBN	0.0835	−0.0601	0.0234	0.1436
BRBS	0.0342	−0.0932	−0.0590	0.1274
CHBR	0.0228	−0.0143	0.0085	0.0372
DBST	0.2465	−0.1160	0.1305	0.3625
FDNG	0.1081	−0.3143	−0.2062	0.4224
FHRJ	0.0562	−0.0738	−0.0176	0.1301
GLMT	0.0093	−0.0256	−0.0163	0.0349
JASC	0.0539	−0.0849	−0.0310	0.1388
LAMD	0.0483	−0.0550	−0.0067	0.1033
MHAN	0.0607	−0.0157	0.0450	0.0765
SBAK	0.0381	−0.1597	−0.1216	0.1978
SHRZ	0.0226	−0.0897	−0.0671	0.1123
ZABL	0.0308	−0.0421	−0.0113	0.0730
ZRND	0.0854	−0.1344	−0.0490	0.2198

4.3. Rotation rate

The rotation rates are negative values in all stations. So rotation isn't clockwise. Table 6 and Fig. 12 represent values of rotation rate and its

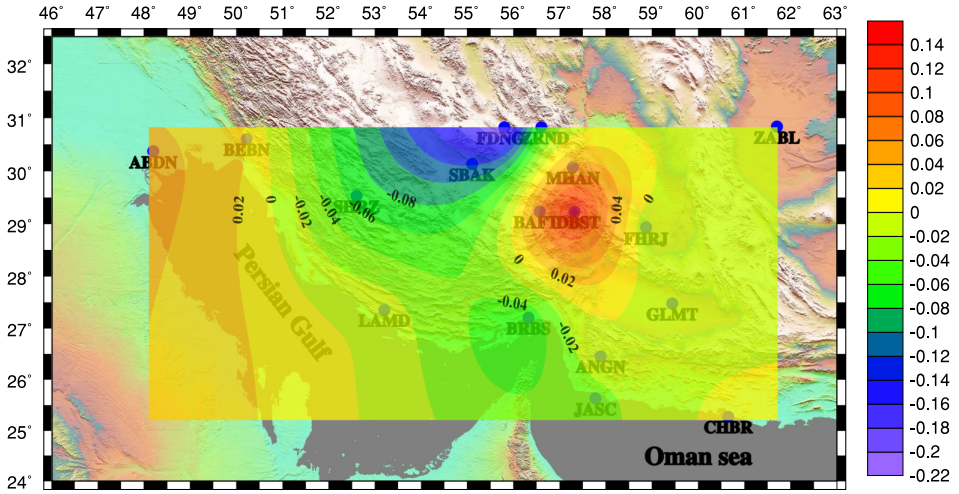

Fig. 9. Contour map of dilatation for study region (μ-strain/year).

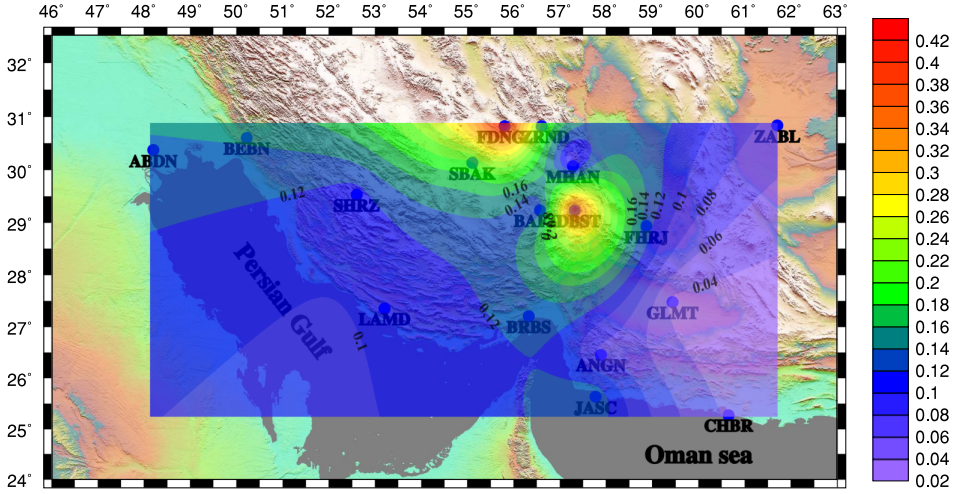

Fig. 10. Contour map of shearing for study region (μ-strain/year).

contour map, respectively. Maximum values of rotation rates are 6.09 and 5.46 in the stations CHBR and DBST, respectively. Stations LAMD and FDNG have minimum rotation rates (2.39 and 2.9, respectively).

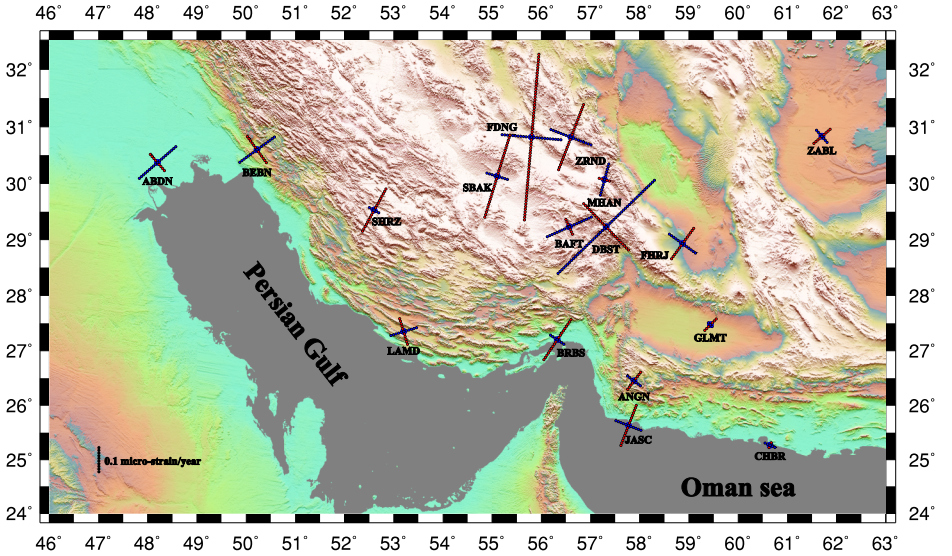

Fig. 11. Axis of stretching (blue) and compression (red).

Table 6. Values of anti-clockwise rotation rate ($\times 10^{-7}$ deg/yr).

Station	Rotation rate
ABDN	3.43
ANGN	4.73
BAFT	4.33
BEBN	4.72
BRBS	5.43
CHBR	6.09
DBST	5.46
FDNG	2.90
FHRJ	5.21
GLMT	4.72
JASC	4.72
LAMD	2.39
MHAN	4.30
SBAK	4.43
SHRZ	4.28
ZABL	4.47
ZRND	3.90

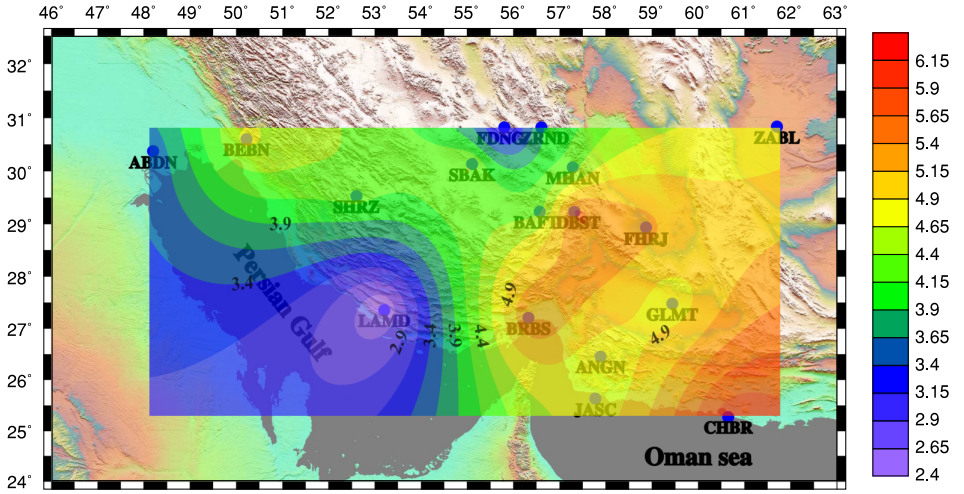

Fig. 12. The contour map of rotation rate ($\times 10^{-7}$ deg/yr).

5. Surveying the correctness of results

The condition number is a parameter that represents sensitivity values of function related to input error. This number is obtained from dividing maximum singular value to minimum singular value of Kernel matrix. This value is 1 to ∞. Value 1 and ∞ show the best and the worst condition, respectively. So, if this number is low, we can estimate the solution (model) more carefully. In this study, the condition numbers are low, so inversion problem is in good condition and has stable solution. Maximum values obtained in ABDN and SHRZ stations with values 13.31 and 8.52, respectively (total average is 4.7). In other words, there is the best (stable) condition in the BAFT station with the condition number of 1.96. Other values are shown in Table 7.

6. Discussion and conclusion

As mentioned before, the purpose of this study was the investigation of crustal deformation in the Zagros collision zone and the Makran subduction zone with geodetic data. To achieve this purpose, the data of 17 GPS

Table 7. condition numbers in the inversion calculation.

Station	Condition number
ABDN	13.31
ANGN	2.13
BAFT	1.96
BEBN	6.74
BRBS	3.09
CHBR	4.47
DBST	4.39
FDNG	3.64
FHRJ	2.75
GLMT	4.83
JASC	2.52
LAMD	5.69
MHAN	2.18
SBAK	4.01
SHRZ	8.52
ZABL	5.96
ZRND	4.42

permanent stations with 2-D isoparametric method were used. The results were analyzed with condition number of kernel matrix. Because of small size of amount, it can be said that the results have good stability and are great to be trusted.

In 11 stations, dilation values are indications of compression domination in the region. Only in 6 stations, values of stretching are dominant on the compression. This is convincing due to the convergence of Arabian and Eurasian plates on one hand and on the other hand the Indian subcontinent towards Eurasia is justified. The compression axis is nearly vertical along the Zagros and will be a reason to reverse and thrust faulting in the Zagros. But according to the North-South trending of Sbzvaran-Jiroft-Kahnuj and the compression and extensional axis direction, the mechanism of this system will be strike-slip.

According to the shearing contour map in two areas the amount of shearing which is related to the other parts are increased significantly. Since the shearing is defined as the maximum change in along, it is expected to be big strike-slip fault in these two points. Referring to the map of active faults

of Iran, these points are on the surrounding of Jiroft-Kahnuj and Rafsanjan faults, respectively. So sudden changes in the shearing can be used as detection of strike-slip faults.

The axes of extension/compression in the Zagros-Makran transition zone have rotated significantly, and it seems to be in communication with the sensitive change of the fault trending from Zagros toward the transition zone and different faulting to the Zagros (in terms of trending and mechanism) is justified on these rotations. Also, this axis in the Makran are smaller than the Zagros, which demonstrates the influence of the Arabian plate moving toward Iran is more than the moving impact of the Indian subcontinent plate. It can be concluded that the values of rotation rate of stations located in East of Zagros-Makran transition zone are larger than western stations.

The achieved velocity vectors towards the Eurasian plate have the northeast direction, which are in compliance with Iran and Eurasian convergence. The displacement rate at the BABS station (in the vicinity of the ZMP fault system and Oman Line), both in terms of magnitude and azimuth is larger than the other stations. This represents a significant change in the strain field in the Zagros-Makran transition zone towards its surrounding areas.

According to the Zagros faults (NW–SE) and Zendan-Minab-Palami fault system trending (in the Zagros-Makran transition zone) and the direction of velocity vectors which are obtained in this study, the mechanism of compression for Zagros faults and strike slip for ZMP fault system, is justified. The convergence of plates in Eurasia and Iran, the velocity vector of eastern stations have smaller magnitude and it would be associated with adjacency of these stations and relatively stable block of Lute.

Shortening in the Zagros region is a well-known phenomenon. Based on the amounts of convergence and divergence that are determined, taking into account the LAMD station as the station in the southern end of the Zagros and stations MHAN, FDNG, SBAK, BAFT as stations in the Northeast Zagros, and the difference of velocity magnitude between these stations, shortening in the Zagros is obvious.

Weak points of determining the strain and the deformation analysis with geodetic observations are the heterogeneous distribution, lack of stations and lack of access to newer data. So the need for more permanent stations can be felt especially in important areas such as the Zagros for more detailed and applied studies. As were obtained in this study, the condition number

in the regions where the density of stations is low, they have larger values than denser regions. For example ABDN and SHRZ stations (which are in the West region) have higher condition number.

References

Allmendinger R. W., Reilinger R., Loveless J., 2007: Strain and rotation rate from GPS in Tibet, Anatolia, and the Altiplano. Tectonics, **26**, 3, TC3013, doi: 10.1029/2006TC002030.

Bayer R., Shabanian E., Regard V., Doerflinger E., Abbassi M., Chery J., Nilforoushan F., Tatar M., Vernant P., Bellier O., 2003: Active deformation in the Zagros–Makran transition zone inferred from GPS measurements in the interval 2000–2002. Geophys. Res. Abstr., **5**, 5891.

Byrne D. E., Sykes L. R., Davis D. M., 1992: Great thrust earthquakes and aseismicslip along the plate boundary of the Makran Subduction Zone. J. Geophys. Res., **97**, B1, 449–478, doi: 10.1029/91JB02165.

Cai J., Grafarend E. W., 2007: Statistical analysis of geodetic deformation (strain rate) derived from the space geodetic measurements of BIFROST Project in Fennoscandia. J. Geodyn., **43**, 2, 214– 238, doi: 10.1016/j.jog.2006.09.010.

Hessami K., Nilforoushan F., Talbot C. J., 2006: Active deformation within the Zagros Mountains deduced from GPS measurements. J. Geol. Soc., **163**, 1, 143–148, doi: 10.1144/0016-764905-031.

Jackson J., McKenzie D., 1984: Active tectonics of the Alpine-Himalayan belt between western Turkey and Pakistan. Geophys. J. Int. Roy. Astron. Soc., **77**, 1, 185–264, doi: 10.1111/j.1365-246X.1984.tb01931.x.

Kashani I., Wielgosz P., Grejner-Brzezinska D. A., Mader G. L., 2008: A New Network-Based Rapid - Static Module for the NGS Online Positioning User Service – OPUS-RS. Navigation, **55**, 3, 225–234, doi: 10.1002/j.2161-4296.2008.tb00432.x.

Lay T., Wallace T., 1995: Modern Global Seismology. Academic Press, United States, 521 p.

Masson F., Anvari M., Djamour Y., Walpersdorf A., Tavakoli F., Daignieres M., Nankali H., Van Gorp S., 2007: Large-scale velocity field and strain tensor in Iran inferred from GPS measurements: new insight for the present-day deformation pattern within NE Iran. Geophys. J. Int., **170**, 1, 436–440, doi: 10.1111/j.1365-246X.2007.03477.x.

McCall G. J. H., 1997: The geotectonic history of the Makran and adjacent areas of southern Iran. J. Asian Earth Sci., **15**, 6, 517-531, doi: 10.1016/S0743-9547(97)00032-9.

McClusky S., Reilinger R., Mahmoud S., Ben Sari D., Tealeb A., 2003: GPS constraints on Africa (Nubia) and Arabia plate motions. Geophys. J. Int., **155**, 1, 126–138, doi: 10.1046/j.1365-246X.2003.02023.x.

McQuarrie N., 2004: Crustal scale geometry of the Zagros fold–thrust belt, Iran. J. Struct. Geol., **26**, 3, 519–535, doi: 10.1016/j.jsg.2003.08.009.

Mirzaei N., Gao M., Chen Y. T., 1998: Seismic source regionalization for seismic zoning of Iran: major seismotectonic provinces. J. Earthquake Predict. Res., **7**, 465–495.

Molinaro M., Leturmy P., Guezou J.-C., Frizon de Lamotte D., Eshraghi S. A., 2005: The structure and kinematics of the south-eastern Zagros fold-thrust belt, Iran: From thin-skinned to thick-skinned tectonics. Tectonics, **24**, 3, TC3007, doi: 10.1029/2004TC001633.

Regard V., Hatzfeld D., Molinaro M., Aubourg C., Bayer R., Bellier O., Yamini-Fard F., Peyret M., Abbasi M. R., 2010: The transition between Makran subduction and the Zagros collision: recent advances in its structure and active deformation. Geol. Soc. Spec. Publ., **330**, 41–64, https://hal.archives-ouvertes.fr/hal-00356532, doi: 10.1144/SP330.4.

Shen Z. K., Jackson D. D., Ge B. X., 1996: Crustal deformation across and beyond the Los Angeles basin from geodetic measurements. J. Geophys. Res., **101**, B12, 27957–27980, doi: 10.1029/96JB02544.

Spakman W., Nyst M., 2002: Inversion of relative motion data for estimates of the velocity gradient field and fault slip. Earth Planet. Sci. Lett., **203**,1, 577–591, doi: 10.1016/S0012-821X(02)00844-0.

Tatar M., Hatzfeld D., Martinod J., Walpersdorf A., Ghafori-Ashtiany M., Chéry J., 2002: The present-day deformation of the central Zagros from GPS measurements. Geophys. Res. Lett., **29**, 19, 33-1–33-4, doi: 10.1029/2002GL015427.

Vanicek P., Krakiwsky E., 1986: Geodesy: The Concepts. 2nd Edition, Elsevier Science, North-Holland, Amsterdam., 714 p.

Vernant P., Nilforoushan F., Hatzfeld D., Abbasi M. R., Vigny C., Masson F., Nankali H., Martinod J., Ashtiani A., Bayer R., Tavakoli F., Chéry J., 2004: Present-day crustal deformation and plate kinematics in Middle East constrained by GPS measurements in Iran and northern Oman. Geophys. J. Int., **157**, 1, 381–398, doi: 10.1111/j.1365-246X.2004.02222.x.

Contributions to Geophysics and Geodesy Vol. 50/1, 2020 (83–111)

Estimation of GNSS tropospheric products and their meteorological exploitation in Slovakia

Martin IMRIŠEK[1,2,*], Mária DERKOVÁ[2], Juraj JANÁK[1]

[1] Department of Theoretical Geodesy, Faculty of Civil Engineering, Slovak University of Technology, Bratislava, Slovak Republic; e-mail: martin.imrisek@stuba.sk, juraj.janak@stuba.sk

[2] Slovak Hydrometeorological Institute, Bratislava, Slovak Republic; e-mail: maria.derkova@shmu.sk

Abstract: This paper discusses the in near–real time processing of Global Navigation Satellite System observations at the Department of Theoretical Geodesy at the Slovak University of Technology in Bratislava. Hourly observations from Central Europe are processed with 30 minutes delay to provide tropospheric products. The time series and maps of tropospheric products over Slovakia are published online. Zenith total delay is the most important tropospheric parameter. Its comparison with zenith total delays from IGS and E–GVAP solutions and the validation of estimated zenith total delay error over year 2018 have been made. Zenith total delays are used to improve initial conditions of numerical weather prediction model by the means of the three–dimensional variational analysis at Slovak Hydrometeorological Institute. The impact of assimilation of different observation types into numerical weather prediction model is discussed. The case study was performed to illustrate the impact of zenith total delay assimilation on the precipitation forecast.

Key words: GNSS processing, zenith total delay, data assimilation, numerical weather prediction model

1. Introduction

The processing of Global Navigation Satellite System (GNSS) observations has a long tradition at the Department of Theoretical Geodesy at the Slovak University of Technology in Bratislava. Since 2009, the sub network of EUREF Permanent Network (EPN) and Central European Permanent (CEPER) network were designed to estimate coordinates, tropospheric and

*corresponding author: e-mail: martin.imrisek@stuba.sk

doi: 10.31577/congeo.2020.50.1.5

ionospheric parameters for site velocities estimates and for the determination of Precipitable Water Vapour (PWV) over the observing stations (*Hefty et al., 2009*).

The tropospheric parameters express the impact of refraction of transmitted signals from GNSS satellites to receivers on Earth. This refraction is denoted as tropospheric delay and it is a consequence of the propagation of GNSS signals through dry gases and water vapour in the atmosphere. The delay caused by dry gases is stable and can be modelled with high precision: *Saastamoinen (1972), Niell (1996), Hopfield (1969), Henriksen et al. (1972)*, Global Mapping Function (*Böhm et al., 2006a*) combined with Global Model of Pressure and Temperature (*Böhm et al., 2007*) and with Vienna Mapping Function (*Böhm et al., 2006b*) combined with ECMWF model. On the other hand, the delay caused by water vapour is not stable and the distribution does not correspond to the dry gases. Nearly half of the total atmospheric water vapour is accumulated between sea level and about 1.5 km altitude, the other 45% of the water vapour is distributed up to the altitude of 5 km.

The GNSS observation processing at the Department of Theoretical Geodesy focused mainly on tropospheric parameters was described in *Igondová* and Cibulka (2010). This network consisted of 58 GNSS permanent stations, it was processed four times per day (at 03, 09, 15, 21 Universal Coordinated Time (UTC)) from four one-hour GNSS data files with a two hours delay. We have developed a new system for estimating the tropospheric parameters[1] in near real–time and their conversion to various tropospheric products.

Multiple GNSS networks are nowadays processed at the Department of Theoretical Geodesy. In general the networks can be distinguished according to the latency. The final solutions of the sub network of EPN and CEPER network are estimated with two and three weeks latency based on daily observation files with the Precise Network Positioning (PNP) method. On the contrary, the networks processed in near–real time have latency in minutes after the hourly observation files are downloaded.

The requirements for tropospheric parameters estimated in near–real time are following: (i) the tropospheric parameters should representatively describe the state of troposphere, (ii) the latency should be small to satisfy

[1] with addition of tropospheric gradients

the needs of numerical weather nowcasting systems. These two requirements are in contradiction. Therefore a balance between these two requirements and optimal processing strategy should be implemented to satisfy these requirements.

The GNSS tropospheric products are becoming an important source of information that is improving the description of the water vapour distribution in the atmosphere. Many meteorological institutes utilize Zenith Total Delay (ZTD) estimates in their global and limited area Numerical Weather Prediction (NWP) models (*Guerova et al., 2016*). ZTD data enter the data assimilation systems as a valuable complementary observation of humidity with high spatial and temporal resolution. These features are essential to describe the high impact weather phenomena associated with moisture processes. Recently, the benefit of the utilization of the GNSS tropospheric products in numerical weather prediction in Europe has been widely demonstrated. *Poli et al. (2007)* developed an assimilation methodology of ZTD data in the global model and observed their positive impact over different meteorological regimes. In limited area NWP models various improvements in moisture-related parameters by ZTD data assimilation were shown as well. In *Storto and Randriamampianina (2010)* improvement in short–range humidity forecasts in winter period was discussed. The paper *Mile et al. (2019)* shows the error reduction of NWP derived values of two meter temperature and humidity. *Mahfouf et al. (2015)* demonstrates better localisation and intensity of forecasted precipitation for Application de la Recherche à l'Opérationnel à Méso-Échelle (AROME)/France NWP model.

At Slovak Hydrometeorological Institute (SHMU) currently only the measurements from the surface weather stations are used operationally for data assimilation purposes (*Derková et al., 2017*). However, in the preparation of the future setup of the convection resolving numerical weather prediction system there are several activities ongoing to explore the potential of high resolution data assimilation. Among others, in the frame of cooperation between SHMU and the Department of Theoretical Geodesy the ZTD data assimilation procedure is being investigated.

The aim of this paper is to summarize the current state of GNSS processing activities at the Department of Theoretical Geodesy and to demonstrate the potential of application of GNSS products in the numerical weather analysis and prediction system at the SHMU. The influence of the atmo-

sphere on the propagation of the GNSS signals is described in the Sec. 2. The Sec. 3 presents the setup of routine processing of GNSS measurements. Validation of estimated ZTD is discussed in the Sec. 4. Various tropospheric products and transformation of ZTD to PWV are described in the Sec. 5. Exploitations of tropospheric products in meteorology are presented in the Sec. 6.

2. GNSS observations and the atmosphere

The signals from GNSS are bent while propagating through the atmosphere due to ionospheric and tropospheric refraction. This bent causes delay, which affects the measured pseudorange and carrier phase from satellites to receiver on the ground. Ionospheric delay can be effectively removed by processing strategy or with ionospheric correction. The tropospheric delay has to be modelled and estimated together with other parameters e.g. coordinates, clock correction etc.

The pseudorange measurement P_k^i for satellite i and receiver k may be expressed as:

$$P_k^i = \rho_k^i + \Delta\rho_k^i + I_k^i + T_k^i + c\delta_k - c\delta^i, \tag{1}$$

where
ρ_k^i is the geometric range between satellite i and receiver k,
$\Delta\rho_k^i$ is the sum of relativistic effects, instrumental delays, multipath and receiver noise,
T_k^i is the tropospheric delay for satellite i and receiver k,
I_k^i is the ionospheric delay for satellite i and receiver k,
c is the speed of light in vacuum,
δ_k is the receiver clock offset from the GNSS time scale,
δ^i is the satellite clock offset from the GNSS time scale.

Besides the pseudorange, carrier phase L_k^i is also used to obtain a measure of the apparent distance between the satellite and receiver. These carrier phase measurements are much more precise than the code measurements (typically two orders of magnitude more precise), but they are ambiguous by an unknown integer number of wavelengths (λn_k^i). The carrier phase measurement L_k^i for satellite i and receiver k may be expressed as:

$$L_k^i = \rho_k^i + \Delta\rho_k^i - I_k^i + T_k^i + c\delta_k - c\delta^i + \lambda n_k^i \,, \tag{2}$$

where

λ is the wavelength of transmitted signal,
n_k^i is the integer ambiguity.

From now on only the tropospheric delay will be discussed in this paper. The ionospheric delay, relativistic effects, instrumental delays, multipath and receiver noise etc. can be eliminated by processing strategy or by precomputed corrections from global analysis center International GNSS Service (IGS). The tropospheric delay, denoted as Slant Total Delay (STD), can be expressed as:

$$T_k^i = mf_h(e)\, ZHD + mf_w(e)\, ZWD + mf_g(e)\left[G_N \cos(A) + G_E \sin(A)\right], \tag{3}$$

where

e is the elevation of measurement,
A is the azimuth of measurement,
mf_h is the coefficient of hydrostatic mapping function,
mf_w is the coefficient of wet mapping function,
mf_g is the coefficient of gradient mapping function estimated as:

$$mf_g(e) = \frac{1}{\sin(e)\tan(e) + 0.0032} \text{ according to } \textit{Chen and Herring (1997)},$$

ZHD is the zenith hydrostatic delay,
ZWD is the zenith wet delay,
G_N is the north tropospheric gradient,
G_E is the east tropospheric gradient.

The terms of Eq. (3) express slant hydrostatic delay ($mf_h(e)ZHD$), slant wet delay ($mf_w(e)ZWD$) and gradient delay ($mf_g(e)\left[G_N \cos(A) + G_E \sin(A)\right]$) from satellite i to receiver k respectively. In the estimation of parameters it is not possible to obtain the tropospheric delay for each measurement (the design matrix would be singular). Hence, the ZTD of receiver is estimated from longer time period. The ZTD can be divided, similarly to tropospheric delay, to hydrostatic Zenith Hydrostatic Delay (ZHD) and wet component Zenith Wet Delay (ZWD) (*Davis et al., 1985*). The ZHD is

caused by the dry gases present in the atmosphere. This component is relatively stable and can be sufficiently modelled by climatological or numerical weather prediction model. The hydrostatic delay is about 2.3 meters in zenith and about 10 meters in 10° elevation. On the other hand, the ZWD varies more with change of local weather conditions. The delay caused by water vapour and condensed water in form of clouds is ranging from 0.1 meters in winter to 0.3 meters in summer.

Tropospheric products are widely exploited in the NWP modelling. These data can be used to improve initial conditions of NWP model.

3. Estimation of zenith total delay

The processing of the hourly GNSS measurements is carried out in near real–time each hour with PNP method at the Department of Theoretical Geodesy at the Slovak University of Technology (SUT) in Bratislava[2] from 2016. The network consists of 59 permanent GNSS stations (Fig. 1). Hourly data are downloaded from regional data centre Federal Office of Metrology and Surveying Austria (*Sehnal et al., 2019*), Bundesamt für Kartographie und Geodäsie (*Bruyninx et al., 2012*) and local data centre at the Department of Theoretical Geodesy. The data files are stored in Receiver INdependent EXchange format (RINEX) version 2.11 (*IGS, 2019*) which includes Global Positioning System (GPS) and Globalnaya Navigatsionnaya Sputnikovaya Sistema (GLONASS) measurements only. The coordinates and tropospheric parameters are estimated by multi–GNSS data processing software developed at the Astronomical Institute of the University of Bern version 5.2 (*Dach et al., 2015*). All mandatory files required for processing are downloaded from Center for Orbit Determination in Europe (CODE) data centre. The rapid Earth orientation parameters, ionospheric corrections and satellite clock corrections (*Dach et al., 2018*) are downloaded from the CODE data centre as well. The rapid satellite positions are primarily downloaded from IGS. In case the combined solution is not available the CODE solution is downloaded.

The a priori coordinates of permanent GNSS stations are interpolated to processing epoch from EPN multi–year position and velocity solution

[2] described as SUT solution

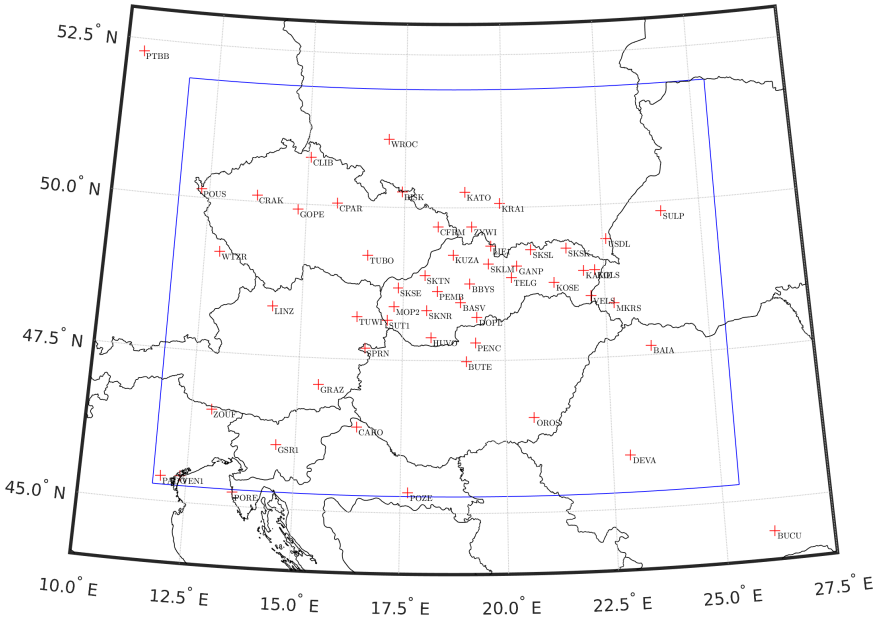

Fig. 1. Map of GNSS permanent stations and NWP domain of AROME/SHMU (blue polygon).

in reference frame IGS14. A priori coordinates for stations not included in EPN are computed from stable ten days long time series. The position from site log file is used as a priori coordinates if the station has not long enough time series of coordinates, or the time series have standard deviation more than 10 mm. The station is excluded from processing if there are any data gaps in last eight hours. This restrictions should provide only estimation of reliable ZTD from the stations without data issues. The PNP method is using baselines to differ observations between permanent GNSS stations. The baselines are created with the OBS–MAX optimization criterion. This method creates baselines upon amount of common time epochs of the same satellite measurements between two stations. The outputs from the Global Model of Pressure and Temperature (*Böhm et al., 2007*) and Global Mapping Function (*Böhm et al., 2006a*) are used as a priori ZHD and coefficients of mapping functions in parameter estimation. The model *Chen and Herring (1997)* is chosen for estimation of tropospheric gradients G_N and G_E.

4. Validation of estimated zenith total delay

Multiple validations of zenith total delays estimated in near real–time were done. First one year long error analysis of ZTD was performed. The second comparison was done between ZTD of SUT and The EUMETNET EIG GNSS water vapour programme (E–GVAP) solutions. The last comparison of ZTD was carried out between SUT and IGS solutions. The choice of permanent stations for validations depended on the status of GNSS network at the time of comparison and on the availability of the tropospheric products from other sources.

4.1. Zenith total delay error analysis

The analysis of ZTD was carried out for the year 2018. This analysis was performed over several GNSS permanent stations chosen to represent various regions and to cover the whole network (Fig. 1). The mean error of ZTD at GNSS permanent stations varies from the 0.80 mm in the winter to 1.56 mm in the summer. Mean time series of ZTD error are displayed in Table 1 of individual permanent stations in the winter and in the summer 2018.

Table 1. Statistics of ZTD errors in summer and winter period of the year 2018 [mm].

	Winter		Summer	
Station	Mean	Standard deviation	Mean	Standard deviation
BASV	0.91	0.094	1.14	0.158
BBYS	0.87	0.102	1.06	0.154
BUCU	1.03	0.102	1.31	0.197
DEVA	1.22	0.121	1.51	0.235
GANP	0.85	0.090	1.06	0.153
GRAZ	0.83	0.082	1.04	0.155
TUBO	0.80	0.086	1.01	0.150
WTZR	0.84	0.090	1.08	0.312
ZIMM	1.23	0.140	1.56	0.245

The mean ZTD errors are 25% higher in the summer than in the winter. This difference is caused by increased content of water vapour in the atmosphere in the summer period. The hot air has bigger water vapour capacity

than the cold air and contains more water vapour. The ZTD errors at 00 and 12 UTC were compared for the whole year. No significant increase due to diurnal cycle was detected. Fig. 2 displays the ZTD error time series of the station TUBO (Vysoké učení technické v Brně, Czech Republic). This station has the lowest mean error in the winter and in the summer.

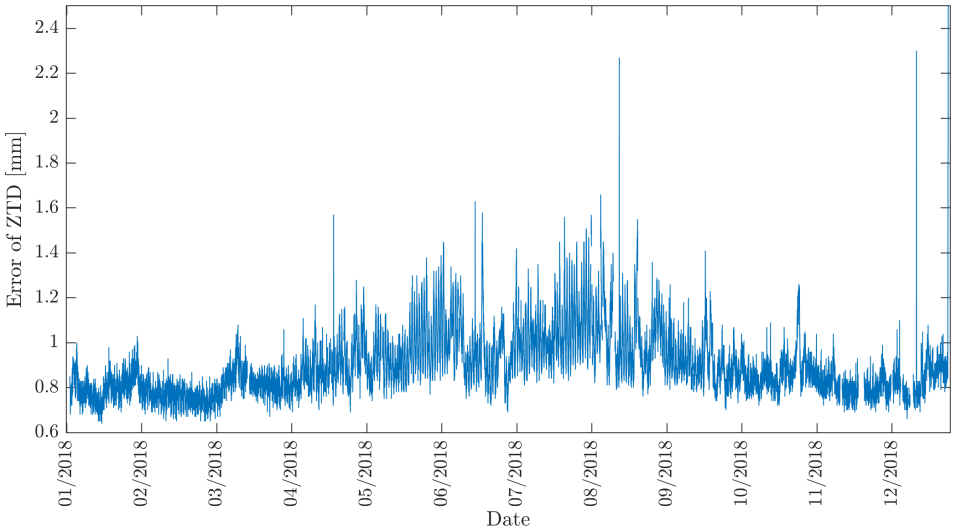

Fig. 2. Zenith total delay error time series [mm] of the year 2018 for the permanent station TUBO.

On the other hand, the permanent station ZIMM (Zimmerwald, Switzerland) has the highest mean winter and summer error of estimated ZTD. Fig. 3 displays the ZTD error time series of the station ZIMM.

The mean winter and summer ZTD error is about 53% and 54% higher at the permanent GNSS station ZIMM than at the station TUBO respectively. This increase might be caused by two reasons. The minor reason might be the different orographic obstacles in horizon and the environment in which the stations are located. While station TUBO is located on flatland in city, permanent station ZIMM is in agricultural environment in Alps. The main reason may be related to the received measurements from satellite systems. While the station ZIMM receives only signals from navigational system GPS, the other stations receive signals also from satellite system GLONASS. The lack of GLONASS observations has impact on the estima-

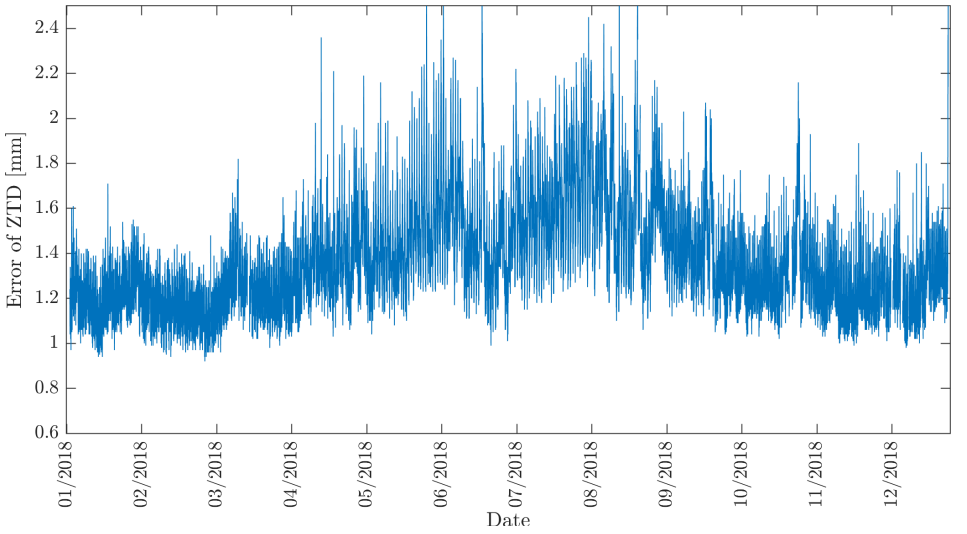

Fig. 3. Zenith total delay error time series [mm] of the year 2018 for the permanent station ZIMM.

tion of ZTD. Stations receiving multiple GNSS have better space coverage of the atmosphere from different directions. This assumption was affirmed by error of station DEVA (Deva, Romania), which has also about 50% higher error of estimated ZTD compared to stations receiving signals from multiple GNSS (Table 1). This stations is also not receiving signals from GLONASS. Overall, the error of estimated zenith total delay is only 0.05% of its absolute value. Therefore we can consider estimated ZTD suitable for further comparison with ZTD from other sources.

4.2. Comparison of SUT and E–GVAP solutions

The comparison with ZTD obtained from independent E–GVAP project (*Guerova et al., 2016*) was done. This programme collects and processes GNSS data from over 1800 European permanent stations in near real–time with PNP method. The comparison was done between 1 and 26 October 2016 on three permanent stations BBYS (Banská Bystrica, Slovakia), CFRM (Frýdek Místek, Czech Republic) and TUBO. Time series of SUT and E–GVAP ZTD for station TUBO is plotted in Fig. 4. The differences are computed as E–GVAP solution minus SUT solution.

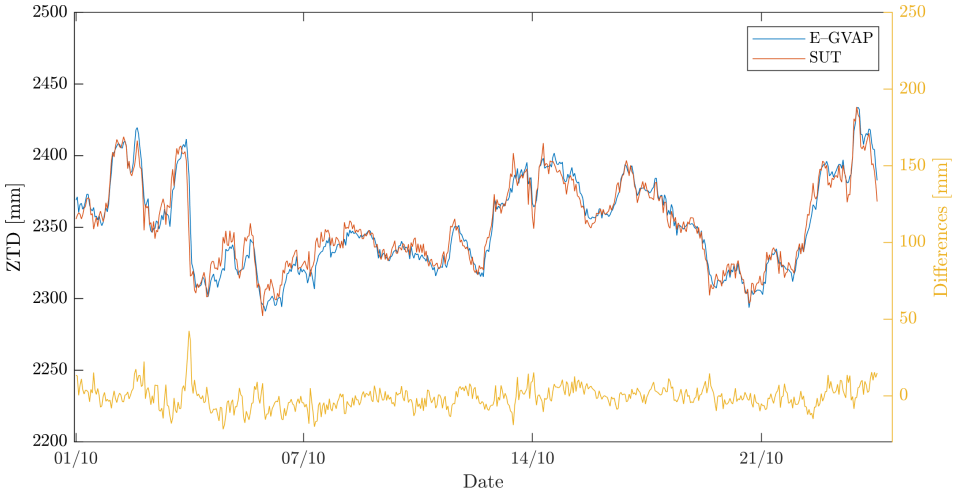

Fig. 4. Comparison of ZTD [mm] between SUT and E–GVAP solutions from 1 to 26 October 2016 at station TUBO.

These differences are shown in Table 2. Mean values of differences are relatively small (only 0.05% of absolute value) and they are comparable to the estimated ZTD error (Table 1). The positive correlations were found for all stations. Small mean differences and positive correlation coefficients declares high fit between SUT and E–GVAP solution. The highest peaks in differences are caused by different time of detection of the ZTD change. The absolute values of ZTD are approximately the same. When a sudden change of weather occurs the SUT and E–GVAP solutions are slightly shifted.

Table 2. Statistics of ZTD differences between SUT and E–GVAP solutions [mm].

	BBYS	CFRM	TUBO
Mean value	−1.8	−1.6	−1.0
Standard deviation	8.17	7.30	7.18
Correlation coefficient	+0.980	+0.978	+0.975

4.3. Comparison of SUT and E–GVAP solutions

The comparison was made between SUT and IGS solutions. The IGS service provides final solution with 21 days delay estimated with Precise Point Positioning (PPP) method for permanent GNSS stations included in IGS

network. The following GNSS permanent stations from IGS network are processed in the SUT solution: BUCU (Bucuresti, Romania), GANP (Gánovce, Slovakia), GRAZ (Graz, Austria), GOPE (Ondřejov, Czech Republic), PENC (Penc, Hungary), WROC (Wroclaw, Poland), WTZR (Bad Koetzting, Germany) and ZIMM (Zimmerwald, Switzerland). The IGS solution is estimated with different approach and the most precise corrections. This makes IGS solution suitable for comparison. Comparison was done on one month period of February 2019. The time series of ZTD and differences for GANP station are displayed in Fig. 5. The differences are computed as IGS solution minus SUT solution.

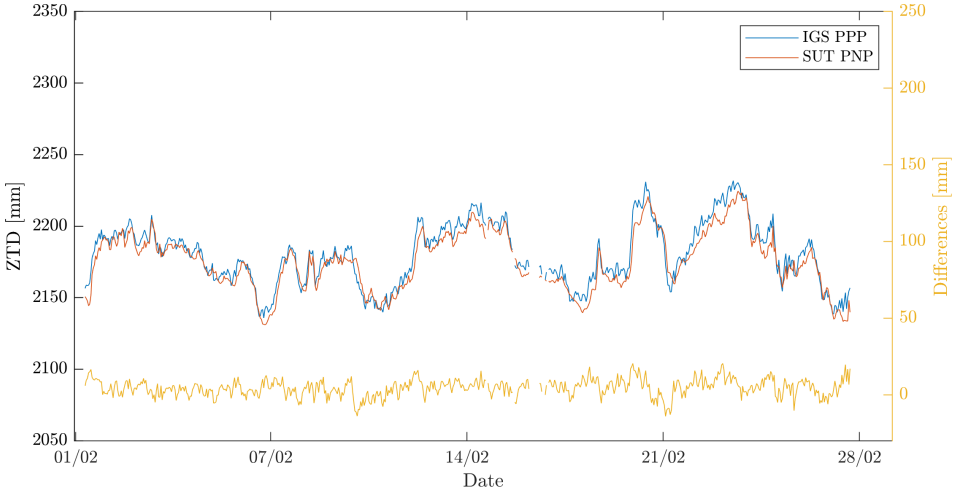

Fig. 5. Comparison of ZTD [mm] at station GANP between SUT and IGS solutions from 1 to 28 February 2019.

The gaps in time series are the consequence of the temporal data unavailability at the station. The mean absolute values of differences for stations are approximately twice bigger than in E–GVAP comparison, but it is only 0.2% of the ZTD. The differences are mainly caused by different processing approach. In PPP method there are no baselines created, so the estimated parameters are independent from measurements of another station. Mean differences, standard deviations and correlation coefficients are shown in Table 3.

Table 3. Statistics of ZTD [mm] differences between SUT and IGS solutions [mm].

	GANP	GRAZ	WTZR
Mean value	4.5	4.2	4.4
Standard deviation	5.60	5.50	5.15
Correlation coefficient	+0.965	+0.971	+0.978

The decrease of standard deviation of differences is about 30% in respect to E–GVAP. Positive and high correlation coefficients declare very good agreement of ZTD between SUT and IGS solution. Nowadays, the comparison is available after each processing for all IGS stations processed in SUT solution. This comparison is available on public web page together with other tropospheric products, more in section 5.

5. Tropospheric products

As demonstrated in the previous sections, the SUT solution provides reliable ZTD comparable quality to the products from E–GVAP and IGS. Therefore, based on this conclusion, the SUT data are further processed, visualised and made available via public web page `http://space.vm.stuba.sk/pwvgraph/space.vm.stuba.sk/pwvgraph/` hosted on local server at the Department of Theoretical Geodesy. Multiple products and additional information about the processing for chosen stations are online:

- 31 day long time series of ZTD,
- 31 day long time series of PWV,
- 31 day long time series of G_N and G_E,
- last 5 hours of ZTD maps (see Fig. 6),
- last 5 hours of PWV maps (see Fig. 7),
- vertical and horizontal cross sections of GNSS tomography valid for last processing,
- time series of position differences between SUT and EPN solutions,
- station data availability statistic for last day, last 7 and 31 days,
- complete processing summary from Bern GNSS software valid for last processing.

The GNSS tomography is a technique to estimate three–dimensional information about a humidity distribution in the troposphere. This estimation

is based on intersection of GNSS signals from different satellites and permanent stations. The tomographic reconstruction is carried out every hour and it is based on *Bender et al. (2011)*. The STD (Eq. 3) is computed from azimuth and elevation to satellites and Global Mapping Function with atmospheric parameters. Azimuth and elevation to satellite is derived from satellite position and station coordinates. The atmospheric parameters are derived from operational Aire Limitée Adaptation dynamique Développement InterNational (ALADIN)/SHMU NWP model (*Derková et al., 2017*).

The ZTD values in maps over Slovakia are transformed to mean sea level pressure for better visualization. The dependency of ZTD on station altitude is reduced to minimum by adding model zenith total delay corresponding to its altitude. After this transformation the isolines are smooth and the values are more consistent[3] as it is displayed in Figs. 6 and 7.

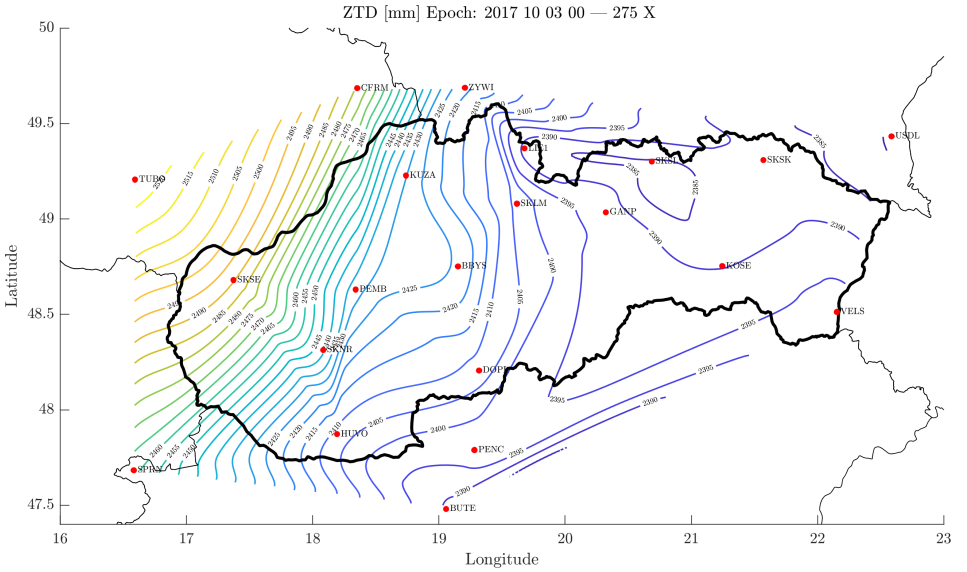

Fig. 6. Map of zenith total delay [mm] over Slovakia on 3 October 2017.

The transformation of ZTD to PWV is proposed in *Bevis et al. (1994)*. Meteorological data are required for this transformation. The SHMU is providing temperature, pressure, relative humidity and other atmospheric

[3] maps are without big gradients

parameters from operational NWP products for permanent GNSS stations in Slovakia and its vicinity. For this transformation the ZHD is [m] required (*Henriksen et al., 1972*):

$$ZHD = 10^{-7}\, k_1 \frac{R_d}{g_{\varphi,H}}\, p\,, \tag{4}$$

where

k_1 is the physical constant of refraction [77.604 $\mathrm{K\,hPa^{-1}}$],

R_d is the specific gas constant of dry air $R_d = \dfrac{R}{M_h}$ [287.058 $\mathrm{kg^{-1}\,K^{-1}}$],

R is the gas constant [8.3144621 $\mathrm{J\,mol^{-1}\,K^{-1}}$],

M_h is the molar mass of the hydrostatic air [0.0289645 $\mathrm{kg\,mol^{-1}}$],

p is the atmospheric pressure [hPa] at station,

$g_{\varphi,H}$ is the gravity acceleration [$\mathrm{m\,s^{-2}}$],

$$g_{\varphi,H} = 9.784\,(1 - 0.00266\,\cos(2\varphi) - 0.00000028\,H), \tag{5}$$

H is the orthometric height [m],

φ is the ellipsoidal laitude of station.

The ZWD is defined as:

$$ZWD = ZTD - ZHD. \tag{6}$$

Bevis et al. (1994) proposed the transformation of ZWD to PWV [m]:

$$PWV = \frac{\kappa\, ZWD}{\rho_w}, \tag{7}$$

where

κ is the transformation coefficient $\kappa = \dfrac{10^8}{R_w\left(\dfrac{k_3}{T_m} + k_2 - mk_1\right)}$,

k_2 is the physical constant of refraction 22.1 $\mathrm{K\,hPa^{-1}}$],

k_3 is the physical constant of refraction 3.766×10^5 $\mathrm{K^2\,hPa^{-1}}$],

T_m is the mean temperature of atmosphere [K] estimated as:

$T_m = 70.2 + 0.72\,T$,

T is the temperature [K] at station,

m is the molar mass ratio of the water vapour and hydrostatic air:

$m = \dfrac{M_w}{M_h}$,

M_w is the molar mass of the water vapour [0.0180152 kg mol^{-1}],
R_w is the specific gas constant of the water vapour, estimated as:
$R_w = \dfrac{R}{M_w}$ [kg^{-1} K^{-1}],
ρ is the density of water [998 kg m^{-1}].

The PWV represents the amount of water contained in a column of atmosphere above permanent station. Fig. 7 displays the PWV distribution over Slovakia in [mm]. One millimetre of PWV is equal to one litre of water per square meter.

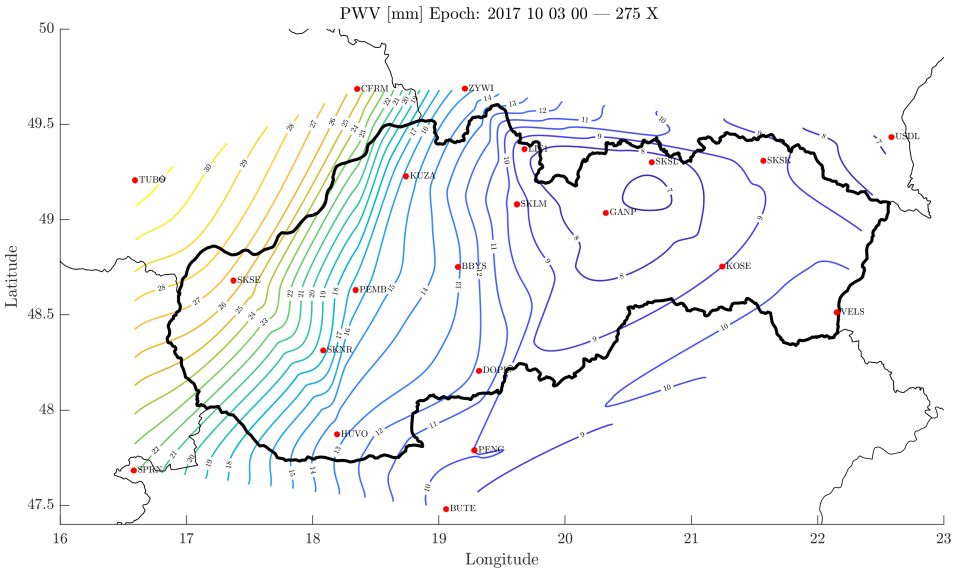

Fig. 7. Map of precipitable water vapour [mm] over Slovakia on 3 October 2017.

6. Usage of tropospheric products

The ZTD or derived products can be exploited in detection of large scale atmospheric systems in form of time series, maps and tomographic reconstruction of troposphere (Sec. 6.1). The tomographic reconstruction of fields of wet refractive indexes of the troposphere, which can be transformed to the water vapour content, is not discussed in this paper. The exploitation of ZTD in NWP models is described from Sec. 6.2.3 to 6.2.5.

6.1. Detection of large scale atmospheric systems

Zenith total delays can be used for detection of movement of large scale atmospheric systems. Change of zenith total delay occurs when a large scale atmospheric system is passing above permanent stations. This case study of passing atmospheric system was carried out for a time window from the 27 September to the 3 October 2017. The wet air was pushing dry air containing small amount of water vapour toward south east direction. The amount of water vapour is included in ZTD as ZWD (Eq. 6). This phenomenon is illustrated in map of ZTD over Slovakia (Fig. 6) and derived map of PWV over Slovakia (Fig. 7). The time series of ZTD at selected stations located along the atmospheric system trajectory are plotted in Fig. 8. The individual time series are reduced by their minimum values for better comparison. The approaching atmospheric system is detected by rapid increase of zenith total delay on permanent stations. At first, the atmospheric system moved over station TUBO (Vysoké učení technické v Brně, Czech Republic), then over SKTN (Trenčín, Slovakia), then over GANP (Gánovce, Slovakia) and at last over the station KOSE (Košice, Slovakia).

The station SKTN is not present in Figs. 6 and 7 because the atmospheric data were not available at the moment of case study.

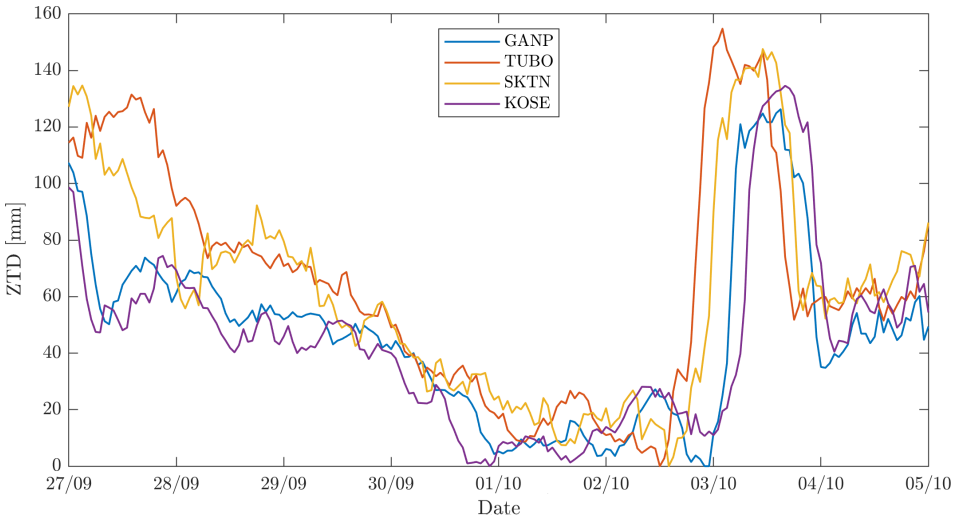

Fig. 8. Time series of differenced ZTD for the selected permanent stations from 27 September to 5 October 2017.

6.2. ZTD assimilation into NWP model

In order to illustrate the potential of exploitation of the ZTD in the high resolution numerical weather forecasting the multiple experiments were conducted at SHMU. The first experiment was a single observation experiment, where we demonstrated impact of one assimilated zenith total delay on numerical weather prediction model. The second experiment compares the impact of assimilation of ZTD with respect to other types of observations. The last experiment demonstrates the impact of ZTD assimilation on precipitation forecast.

6.2.1. Numerical weather prediction model

At SHMU the ALADIN NWP model (*Termonia et al., 2018*) – configuration AROME (*Seity et al., 2011*) is used for data assimilation. The AROME NWP model is adapted to the limited area geometry and the physical parameterization schemes are derived from Meso–NonHydrostatic research model (*Lafore et al., 1998*). AROME NWP model is experimentally exploited at the SHMU (*Derková et al., 2017*). The AROME domain covers Slovakia and vicinity. The size and position of AROME domain is displayed in Fig. 1. The horizontal resolution is 2.0 km on a Lambert projection with $\lambda = (11.73°, 25.40°)$, $\phi = (45.27°, 51.93°)$ which results to 501 and 373 physical[4] grid points in the east–west and north–south directions respectively. The domain is vertically divided into 73 levels using a hybrid pressure terrain–following coordinate system. The height of the lowest level[5] is about 11 m above the ground. The size and resolution of the domain depends on computing capacities of supercomputer at SHMU. This setup of NWP model is referred to as AROME/SHMU. For NWP forecasting[6] the boundary conditions are mandatory. The AROME/SHMU model is nested in ALADIN/SHMU (*Derková et al., 2017*) with hourly coupling frequency.

6.2.2. Assimilation method

The initial conditions[7] for numerical weather forecast can be improved using

[4] the most model computation are in spectral space
[5] model level number 73
[6] denoted as *integration*
[7] the initial state for the integration of the atmospheric model

data assimilation methods. These provide the best possible estimation of the current state of the atmosphere based on the various types of observations and measurements of the atmospheric parameters. Data assimilation is an analysis method in which the observed information is accumulated into the model state by taking advantage of consistency constraints with laws of time evolution and physical properties (*Courtier et al., 1991*). In the experimental setup of AROME/SHMU the Three–Dimensional Variational analysis (3D–Var) method is used to obtain NWP analysis $\mathbf{x}_a$ (*Fischer et al., 2005*). The principle of 3D–Var method is to estimate an approximate solution to the equivalent minimization problem defined by the cost function (Eq. 8). The solution is sought iteratively by performing several evaluations of the cost function:

$$\begin{aligned} J(\mathbf{x}) &= (\mathbf{x}-\mathbf{x}_b)^T \mathbf{B}^{-1} (\mathbf{x}-\mathbf{x}_b) + (\mathbf{y}-H(\mathbf{x}))^T \mathbf{R}^{-1} (\mathbf{y}-H(\mathbf{x})) \,, \\ J(\mathbf{x}) &= J_b + J_o \,, \end{aligned} \tag{8}$$

where

$\mathbf{x}$ is the model state,
$\mathbf{x}_b$ is the background model state[8],
$\mathbf{y}$ is the vector of observations,
H is the observation operator,
$\mathbf{B}$ is the covariance matrix of background model state,
$\mathbf{R}$ is the covariance matrix of observations,
J_o is the observation cost function,
J_b is the background cost function.

An analysis is the production of an accurate image of the true state of the atmosphere at a given time, represented in a model as a collection of numbers. An analysis can be useful in itself as a comprehensive and self–consistent diagnostic of the atmosphere. It can also be used as input data for a numerical weather forecast, or as a data retrieval to be used as a pseudo-observation. It can provide a reference against which to check the quality of observations (*Bouttier and Courtier, 2002*).

Zenith total delays can be used stand alone or together with other observations as $\mathbf{y}$ in the 3D–Var method.

[8] denoted as *guess*

6.2.3. Single ZTD assimilation experiment

The first experiment was an assimilation of a single observation into AROME /SHMU NWP model to demonstrate the impact of ZTD observations on the NWP analysis. The ZTD was from station GANP (Gánovce, Slovakia) estimated in near–real time on 15 August 2018 at 12 UTC. This station was chosen due to the stable time series of estimated tropospheric products, due to successful validation with ZTD from other sources and due to approximate position in the middle of NWP domain. The NWP analysis was created by assimilation of the ZTD with 3D–Var method to the background model state of NWP model. The impact of single observation assimilation is computed as difference of analysis and background model state[9] to show how the information from the assimilated observation propagates horizontally and vertically in space. The impact of single ZTD assimilation on specific humidity is displayed in Fig. 9. As it is shown, the increments at the 65th model level are concentric isolines around the position of assimilated ZTD. Height of the 65th model level is about 209 m above terrain.

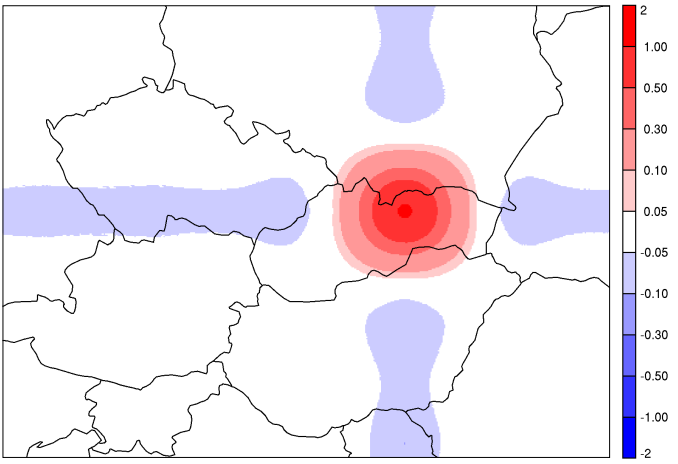

Fig. 9. Increments of specific humidity [1×10^{-4} kg kg^{-1}] on 15 August 2018 12 UTC at model level 65.

The maximum increments of specific humidity reached 1.18×10^{-4} kg kg^{-1} at the 65th model level in the position of permanent station GANP. Whereby

[9] the differences are denoted as *increments*

the increments are close to zero about 100 km away from permanent station. The Fig. 10 displays 155 km east–west direction vertical cross section of increments of specific humidity.

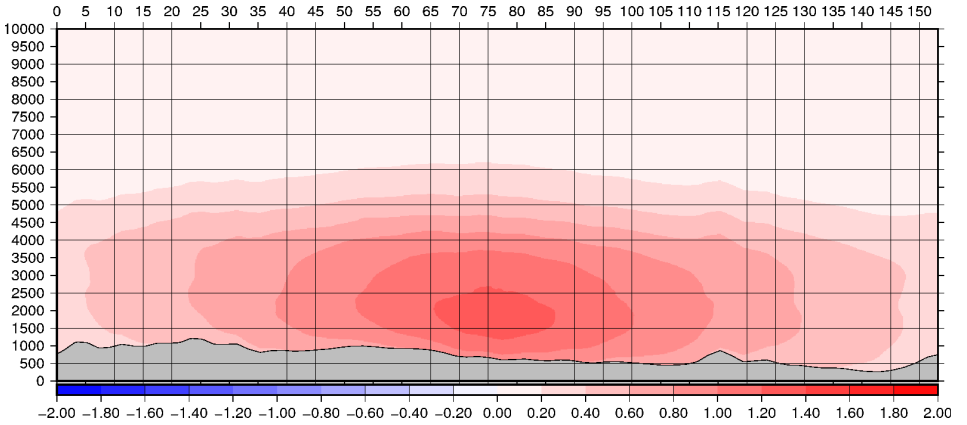

Fig. 10. Specific humidity [1×10^{-4} kg kg^{-1}].

The impact of single ZTD assimilation is located in the bottom layers of the troposphere – below the first 5 km of atmosphere. This result of 3D–Var assimilation method is in agreement with *Mockler (1995)*, who declared that 90% of water vapour is accumulated in the first 5 km of troposphere. The difference between estimated ZTD from SUT solution and from the model state estimated by observation operator H decreased after assimilation from 3.79 mm to 0.35 mm. This decrease illustrates, that the analysis of NWP model has been adapted to assimilated ZTD.

6.2.4. Impact of ZTD assimilation

The impact analysis of ZTD assimilation on AROME/SHMU NWP model with respect to other different observation types was carried out. The experiment was performed for two days. First selected day (19 July 2018) represents rainy weather with locally measured precipitation of 110 mm in 24 h. On the contrary no precipitation were recorded on the second selected day 27 July 2018. For both days the Degrees of Freedom for Signal (DFS) diagnostic was calculated. DFS diagnostic is the derivative of the analysis

increments in the observation space with respect to the observations used in the analysis system. As proposed by *Chapnik et al. (2006)* DFS can be computed through the perturbations of observations:

$$DFS = (\mathbf{y}^p - \mathbf{y})\,\mathbf{R}^{-1}\left(\left(\Delta_g^p - \Delta_a^p\right) - (\Delta_g - \Delta_a)\right), \tag{9}$$

where

Δ_g are the differences between perturbed and non–perturbed observations and background model state,

Δ_a are the differences between perturbed and non–perturbed observations and analysis model state.

The upper index p denotes perturbed differences. Perturbation is done by modifying the assimilated observations by adding small value with normal distribution. The absolute DFS represent the impact of assimilating different observation types into the NWP model, in terms of amount, distribution, instrumental accuracy and observation operator definition. The results are displayed in Figs. 11 and 12. Five data types were assimilated to AROME/SHMU NWP model: observations from ground based meteorological stations (Surface Synoptic Observations (SYNOP) ∼5000 obs.), meteorological observations from air planes (AMDAR ∼2000 obs.), observations from radiosondes (TEMP ∼4000 obs.), wind speed and direction estimated from geostationary meteorological satellites (Atmospheric Motion Vector (AMV) ∼250 obs.) and zenith total delays estimated from hourly processing in near real–time with PNP method at SUT (ZTD ∼120 obs.).

The absolute impact of ZTD assimilation is low compared to other observation types. The ZTD are outnumbered by factor ∼42 compared to SYNOP observations and by factor ∼33 to TEMP observations. The relative DFS illustrates the impact of one assimilated observation compared to other observation types. The impact of one assimilated ZTD is dominant compared to other observation types. The decrease of relative impact of the SYNOP and TEMP observation could be related to space overlapping increments from different observations of the same type (two different observations have impact in the same spatial location). Based on these results the network densification of assimilated GNSS stations is proposed, as there are still uncovered areas in AROME/SHMU model domain (Fig. 1). The overlapping of increments shall be avoided by model tuning.

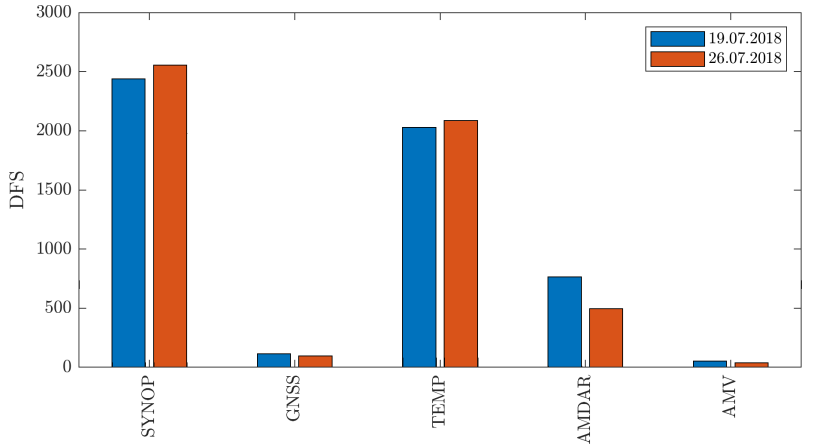

Fig. 11. Absolute DFS of observation types on 19 and 27 July 2018.

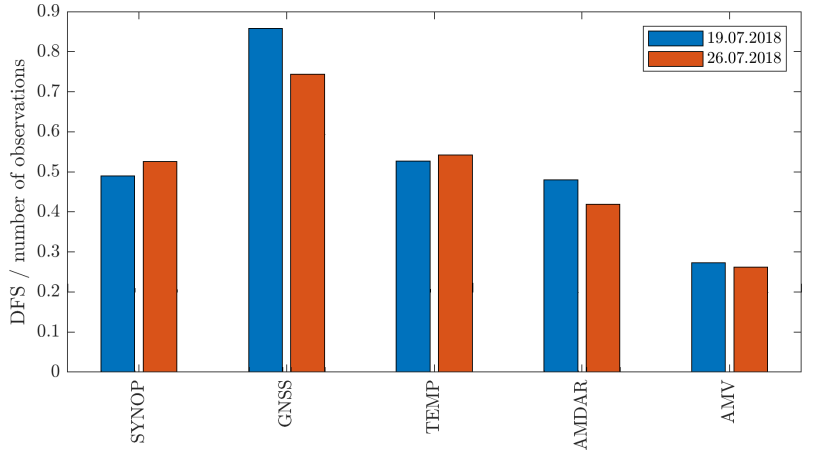

Fig. 12. Relative DFS of observation types on 19 and 27 July 2018.

6.2.5. ZTD assimilation impact case study on precipitation forecast

The impact case study of ZTD assimilation on precipitation forecast was performed on heavy rain situation on 24 and 25 August 2019. The accumulated precipitation over 24 hours were compared to INCA analysis, representing the real state. This INCA analysis is based on radar reflectivity

measurements (which correspond to the intensity of rain) combined with automatic ground weather rain gauge measurements. Three experiments were performed. All experiments have common domain, AROME/SHMU configuration and forecasting length 24 hours. First experiment is without any data assimilation[10]. The second experiment is with data assimilation of SYNOP, AMDAR, TEMP and AMV observations. The zenith total delays were assimilated on top of other observations in the third experiment. The results of 24 hour precipitation forecasts are displayed in Fig. 13.

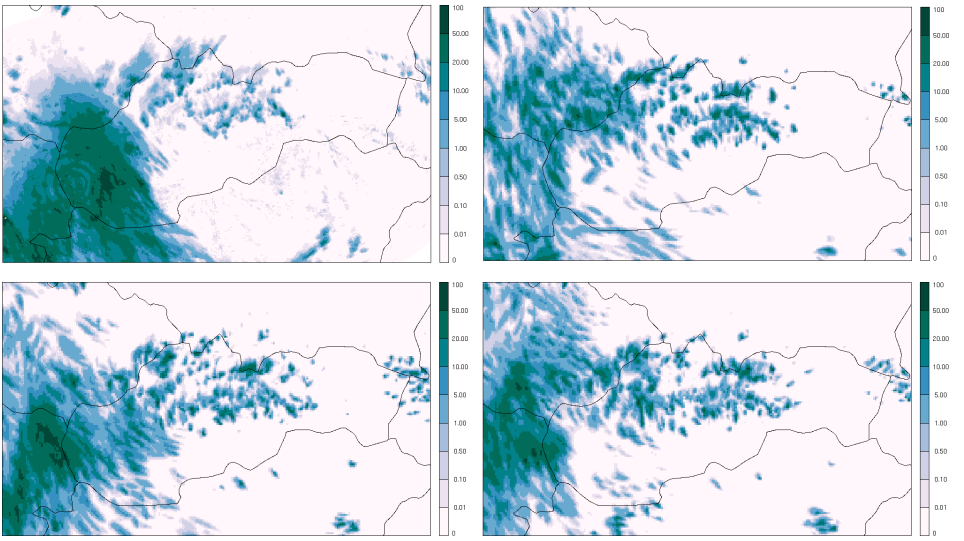

Fig. 13. Accumulated precipitation [mm] from 24 August 2019 12 UTC to 25 August 2019 12 UTC. Top left picture displays INCA analysis. Top right picture displays the experiment without data assimilation. Bottom left picture displays the experiment with ZTD assimilation. Bottom right picture displays the experiment without ZTD assimilation.

The INCA analysis is regarded as a representation of the true state of accumulated precipitation (top left). The AROME/SHMU model without data assimilation (top right) has in this case the most unrealistic 24 hour precipitation forecast compared to INCA analysis. The rain that has occurred in south-western Slovakia was not predicted at all and the precipitation over the mountains in northern Slovakia were overestimated. The

[10] denoted as *dynamic adaptation*

implementation of observation assimilation (without ZTD) with the 3D–Var method results in more realistic total amount of precipitated water (bottom right). The precipitation patterns in eastern Austria and western Slovakia are captured better, albeit still not fully correct. The best result in this case study was achieved by assimilation of all available data types (ZTD included). The ZTD have major impact on spatial location of precipitation. The extent of the territory hit by rain is more realistic with ZTD data utilization.

7. Conclusion and perspectives

New advanced in near–real time system for the GNSS tropospheric parameters estimation and their post processing has been developed at the Department of Theoretical Geodesy at the Slovak University of Technology in Bratislava. Its improvements with respect to the previously exploited one (*Igondová and Cibulka, 2010*) can be quantified as follows:

- the GNSS network is more dense in Slovakia (area per one station decreased from 8200 km^2 to 2300 km^2),
- the latency of processing is reduced four times (from 2 hours to 30 minutes),
- the frequency of processing is quadrupled (parameters are estimated every hour),
- the time span of processed datasets are two times larger (from 4 to 8 hour dataset),
- additional tropospheric parameters are estimated (north and east tropospheric horizontal gradients G_N and G_E).

The most important estimated tropospheric parameter, zenith total delay, was compared to ZTD from E–GVAP and IGS solutions. These comparisons confirmed high standard of SUT solution. Furthermore, new tropospheric products were introduced on top of the standard ZTD and PWV time series and maps. The tomography of the atmosphere and the time series of tropospheric gradients are available on public web page.

We will also focus on estimation and a posteriori analysis of tropospheric horizontal gradients. These gradients are used in the estimation of STD,

which are experimentally assimilated in AROME NWP model.

Tropospheric products derived from the GNSS network processing can provide useful complementary humidity measurements that are essential in the numerical weather prediction to forecast the high impact events associated with the moisture (*Guerova et al., 2016*). This was recently explored at the Slovak Hydrometeorological Institute in its experimental high resolution limited area AROME/SHMU NWP model. The potential of meteorological exploitation of ZTD data was demonstrated using Three–Dimensional variational data assimilation method. ZTD were analyzed together with other measurements to improve the NWP model initial conditions. The academic experiment assimilating only single observation showed how this measurement is horizontally and vertically propagated in the analysis. Dedicated DFS diagnostics after *Chapnik et al. (2006)* was applied to quantify the absolute and relative impact of various observation types within the data assimilation. Although the absolute impact of the ZTD assimilation on NWP analysis is small because the ZTD are outnumbered by other observation types, their relative impact is dominant. These results are in agreement with other studies, see *Mile et al. (2019)*. The ZTD impact on precipitation forecast was demonstrated on the case study. The most realistic accumulated precipitation in terms of maxima as well as their spatialisation were predicted with model where all data including ZTD were used in data assimilation. This confirms the conclusions of of *Mahfouf et al. (2015)*. Achievements described in this article suggest that a cooperation between the geodetic and meteorological communities in Slovakia shall continue. When more computer resources are acquired at SHMU, additional case studies as well as the parallel suites will be carried out to assess and quantify the impact of GNSS tropospheric products in the assimilation and forecasts of the AROME/SHMU system. Furthermore, the pilot implementation of the slant total delays data assimilation at the SHMU is planned.

Acknowledgements. The authors kindly acknowledge the support of the Jan Douša (Geodetic Observatory Pecný) for providing data from E–GVAP project for validation. The ZTD data assimilation experiments with the AROME/SHMU numerical weather prediction model were carried out within the KOSYMOKO project (OPKZP-PO1-SC141-2017-25/ITMS 310011Q847).

References

Bender M., Dick G., Ge M., Deng Z., Wickert J., Kahle H., Raabe A., Tetzlaff G., 2011: Development of a GNSS water vapour tomography system using algebraic reconstruction techniques. Adv. Space Res., **47**, 10, 1704–1720, doi: 10.1016/j.asr.2010.05.034.

Bevis M., Businger S., Chiswell S., Herring T. A., Anthes R. A., Rocken C., Ware R. H., 1994: GPS Meteorology: Mapping Zenith Wet Delays onto Precipitable Water. J. Appl. Meteorol. Climatol., **33**, 3, 379–386, Addison Wesley, Massachusetts, doi: 10.1175/1520-0450(1994)033<0379:GMMZWD>2.0.CO;2.

Böhm J., Niell A. E., Tregoning P., Schuh H., 2006a: Global Mapping Function (GMF): A new empirical mapping function based on numerical weather model data. Geophys. Res. Lett., **33**, 7, L07304, doi: 10.1029/2005GL025546.

Böhm J., Werl B., Schuh H., 2006b: Troposphere mapping functions for GPS and VLBI from ECMWF operationals analysis data. J. Geophys. Res., **111**, B2, B02406, doi: 10.1029/2005JB003629.

Böhm J., Heinkelmann R., Schuh H., 2007: Short Note: A global model of pressure and temperature for geodetic applications. J. Geod., **81**, 10, 679–683, doi: 10.1007/s00190-007-0135-3.

Bouttier F., Courtier P., 2002: Data assimilation concepts and methods. Meteorological Training Course Lecture Series, Education material, ECMWF, https://www.ecmwf.int/node/16928.

Bruyninx C., Habrich H., Söhne W., Kenyeres A., Stangl G., Völksen C., 2012: Enhancement of the EUREF Permanent Network Services and Products. In: Kenyon S., Pacino M., Marti U. (Eds): Geodesy for Planet Earth. International Association of Geodesy Symposia, **136**, Springer, Berlin, Heidelberg, 27–35, doi: 10.1007/978-3-642-20338-1_4.

Chapnik B., Desroziers G., Rabier F., Talagrand O., 2006: Diagnosis and tuning of observational error in a quasi-operational data assimilation setting. Q. J. R. Meteorol. Soc., **132**, 615, 543–565, doi: 10.1256/qj.04.102.

Chen G., Herring T. A., 1997: Effects of atmospheric azimuthal asymmetry on the analysis of space geodetic data. J. Geophys. Res., **102**, B9, 20489– 20502, doi: 10.1029/97JB01739.

Courtier P., Freydier C., Geleyn J.-F., Rabier F., Rochas M., 1991: The ARPEGE project at Météo-France. ECMWF, Shinfield Park, Reading, https://www.ecmwf.int/node/8798.

Dach R., Lutz S., Walser P., Fridez P., 2015: Bernese GNSS Software Version 5.2. Astronomical Institute, University of Bern. http://www.bernese.unibe.ch/docs/DOCU52.pdf.

Dach R., Schaer S., Arnold D., Prange L., Sidorov D., Stebler P., Villiger A., Jäggi A., 2018: CODE rapid product series for the IGS. Astronomical Institute, University of Bern, http://www.aiub.unibe.ch/download/CODE.

Davis J., Herring T., Shapiro I., Rogers A., Elgered G., 1985: Geodesy by radio interferometry: Effects of atmospheric modeling errors on estimates of baseline length.

Radio Sci., **20**, 6, 1593–1607, doi: 10.1029/RS020i006p01593.

Derková M., Vivoda J., Belluš M., Španiel O., Dian M., Neštiak M., Zehnal R., 2017: Recent improvements in the ALADIN/SHMU operational system. Meteorol. J., **20**, 2, 45–52.

Fischer C., Montmerle T., Berre L., Auger L., Stefanescu S. E., 2005: An overview of the variational assimilation in the ALADIN/France NWP system. Q. J. R. Meteorol. Soc., **131**, 613, 3477–3492, doi: 10.1256/qj.05.115.

Guerova G., Jones J., Douša J., Dick G., de Haan S., Pottiaux E., Bock O., Pacione R., Elgered G., Vedel H., Bender M., 2016: Review of the state-of-the-art and future prospects of the ground-based GNSS meteorology in Europe. Atmos. Meas. Tech., **9**, 11, 5385–5406, doi: 10.5194/amt-9-5385-2016.

Hefty J., Igondová M, Droščák B., 2009: Homogenization of long-term GPS monitoring series at permanent stations in Central Europe and Balkan Peninsula. Contrib. Geophys. Geod., **39**, 1, 19–42, doi: 10.2478/v10126-009-0002-8.

Henriksen S. W., Mancini A., Chovitz B. H., 1972: The Use of Artificial Satellites for Geodesy. Geophysical Monograph No. 15, American Geophysical Union, Washington, D.C., 298 p.

Hopfield H., 1969: Two-quartic Tropospheric Refractivity Profile Correcting Satellite Data. J. Geophys. Res., **74,** 18, 4487–4499, doi: 10.1029/JC074i018p04487.

Igondová M, Cibulka D., 2010: Precipitable Water Vapour and Zenith Total Delay time series and models over Slovakia and vicinity. Contrib. Geophys. Geod., **40**, 4, 299–312, doi: 10.2478/v10126-010-0012-6.

IGS, International GNSS Service, 2019: RINEX: The Receiver Independent Exchange Format Version 2.11. https://kb.igs.org/hc/en-us/article_attachments/115007664947/RINEX-211.pdf.

Lafore J.-P., Stein J., Asencio N., Bougeault P., Ducrocq V., Duron J., Fischer C., Héreil P., Mascart P., Masson V., Pinty J. P., Redelsperger J. L., Richard E., Vilà-Guerau de Arellano J., 1998: The Meso-NH atmospheric simulation system. Part I: Adiabatic formulation and control simulations. Ann. Geophys., **16**, 1, 90–109, doi: 10.1007/s00585-997-0090-6.

Mahfouf J-F., Ahmed F., Moll P., Teferle F., 2015: Assimilation of zenith total delays in the AROME France convective scale model: a recent assessment. Tellus A: Dynamic Meteorology and Oceanography, **67**, 1, 20, doi: 10.3402/tellusa.v67.26106.

Mile M., Benáček P., Rózsa S., 2019: The use of GNSS zenith total delays in operational AROME/Hungary 3D-Var over a central European domain. Atmos. Meas. Tech., **12**, 3, 1569–1579, doi: 10.5194/amt-12-1569-2019.

Mockler S. B., 1995: Water vapor in the climate system. Special Report. American Geophysical Union, 2000 Florida Ave., N.W., Washington, D.C., 20009, USA, ISBN 0-87590-865-9.

Niell A. E., 1996: Global mapping functions for the atmosphere delay at radio wavelengths. J. Geophys. Res., **101**, B2, 3227–3246, doi: 10.1029/95JB03048.

Poli P., Moll P., Rabier F., Desroziers G., Chapnik B., Berre L., Healy S. B., Andersson E., El Guelai F.-Z., 2007: Forecast impact studies of zenith total delay data from

European near real-time GPS stations in Météo France 4DVAR. J. Geophys. Res.: Atmospheres, **112**, D6, D06114, doi: 10.1029/2006JD007430.

Saastamoinen J., 1972: Atmospheric Correction for the Troposphere and Stratosphere in Radio Ranging Satellites. In: Henriksen S. W., Mancini A., Chovitz B. H.: The Use of Artifical Satellites for Geodesy, **15**, 247–251. Washington, D.C., doi: 10.1029/GM015p0247.

Sehnal M., Mayer D., Mitterschiffthaler P., 2019: EUREF Analysis and Data Center at BEV Vienna. VGI – Österreichische Zeitschrift für Vermessung und Geoinformation, **2**, 116–118. ISSN 1605-1653.

Seity Y., Brousseau P., Malardel S., Hello G., Bénard P., Bouttier F., Lac C., Masson V., 2011: The AROME-France convective-scale operational model. Mon. Weather Rev., **139**, 3, 976–991, doi: 10.1175/2010MWR3425.1.

Storto A., Randriamampianina R., 2010: A new bias correction scheme for assimilating GPS zenith tropospheric delay estimates. Idojárás ? Quarterly Journal of the Hungarian Meteorological Service, **114**, 4, 237–250.

Termonia P., Fischer C., Bazile E., Bouyssel F., Brožková R., Bénard P., Bochenek B., Degrauwe D., Derková M., El Khatib R., Hamdi R., Mašek J., Pottier P., Pristov N., Seity Y., Smolíková P., Španiel O., Tudor M., Wang Y., Wittmann C., Joly A., 2018: The ALADIN System and its canonical model configurations AROME CY41T1 and ALARO CY40T1. Geosci. Model Dev., **11**, 1, 257–281, doi: 10.5194/gmd-11-257-2018.

Contributions to Geophysics and Geodesy Vol. 50/1, 2020 (113–133)

Estimation of hydraulic parameters by using VES sounding and neural network techniques in the semi-arid Khanasser valley region, Syria

Jamal ASFAHANI*, Zuhair AHMAD

Atomic Energy Commission of Syria,
P.O. Box 6091, Damascus, Syria

Abstract: An alternative approach based on using Vertical Electrical Sounding (VES) measurements and Artificial Neural Network (ANN) technique is newly proposed for computing the hydraulic conductivity K and the transmissivity T of an aquifer. VES measurements in the locations, where available water samples exist are required in such an approach, in order to train a neural network with fitting capability to evaluate both the hydraulic conductivity and transmissivity. The hydraulic conductivity and transmissivity are thereafter extrapolated by the use of trained neural network, even in the VES points where no water samples exist. This approach is practiced and tested in the Khanasser valley, Northern Syria, where the hydraulic conductivity and the transmissivity of the Quaternary aquifer is computed. We find an acceptable agreement between the hydraulic conductivity values obtained by the new approach and those obtained by the pumping test, which range between 0.864 and 8.64 m/day.

Key words: Hydraulic conductivity, Transmissivity, VES Sounding, Khanasser Valley, Syria

1. Introduction

The aquifer behaviour during the different stages of water extraction is predicted by the groundwater modelling by the use of the hydraulic conductivity parameter, considered as the most important in hydrogeology. The pumping tests technique is traditionally applied to estimate the hydraulic conductivity, but this technique is affected being expensive and yields to low spare resolution maps.

Geophysical methods are largely used to develop alternative approaches, aimed at estimating the hydraulic parameter, where specific relationships

*corresponding author: e-mail: cscientific@aec.org.sy (J. Asfahani)

doi: 10.31577/congeo.2020.50.1.6

between hydro-geological and geophysical parameters are provided (*Heigold et al., 1979; Frohlich, 1994; Frohlich et al., 1996; Yadav and Abolfazli, 1998; Salem, 1999; De Lima and Niwas, 2000; Niwas and De Lima, 2003; Dhakate and Singh, 2005; Lesmes and Friedman, 2005; Asfahani, 2007a,b,c; Asfahani, 2010a,b; Arétouyap et al., 2015; Arétouyap et al., 2019a; Arétouyap et al., 2019b*).

We propose in this paper a new practical technique based on the application of vertical electrical sounding (VES) and ANN techniques to estimate the aquifer hydraulic conductivity and transmissivity.

The application of VES technique offers different advantages in comparing with the traditional pumping tests technique. Accordingly, we do not need a ground perforation, where faster information regarding the hydraulic conductivity distribution is obtained with high resolution maps, by the use of dense VES sounding points.

The new proposed neural networks approach takes into consideration only the groundwater salinity, for characterizing the Quaternary aquifer hydraulic conductivity and transmissivity in the semi-arid Khanasser valley region, Northern Syria, Fig. 1.

The ability of ANN as universal function approximator is used in this paper to provide a data-driven approximation of the relation between hydraulic conductivity and hydraulic transmissivity and the saturated aquifer resistivity and the saturated thickness of the Quaternary aquifer. This requires the hydraulic conductivity and transmissivity measurements using pumping tests, which are expensive and complex to operate. Four pumping tests are only available in this work (*Asfahani, 2016*), which are not sufficient to train ANN. The recent computed values of hydraulic conductivity and transmissivity based on VES measurements (*Asfahani, 2016*), and the measured available four pumping test values are therefore used to train ANN.

Geophysical researches have been practiced in the Khanasser Valley through an international research program, directed by three scientific organizations; Bonne University, Germany, International Center for Agriculture Research in the Dry Areas (ICARDA), and Syrian Atomic Energy Commission (*Schweers et al., 2002*). The specific problems related to the marginal dry-land environments were solved by this research program.

Livelihoods, the diversity and dynamics of the natural resources, poverty and the relative easy accessibility made Khanasser as a prime candidate.

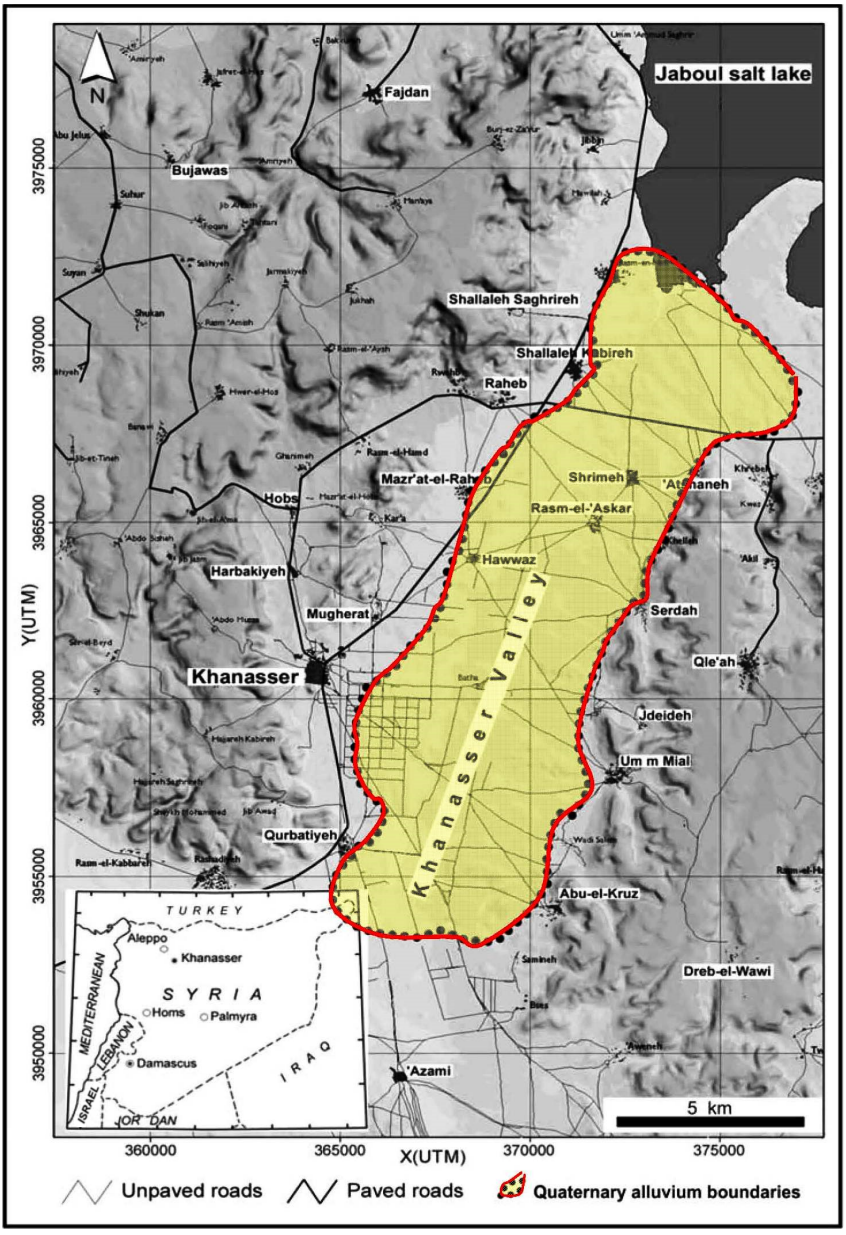

Fig. 1. Location of Khanasser valley, Northern Syria.

The rainfall in the Khanasser region is low and unpredictable, while the natural resources are quite poor and prone to degradation. Annual rainfall ranges between 200 and 250 mm/year, but the annual rainfall extremes between 1957 and 2001 were 93 and 393 mm (*Soumi, 1991*).

2. Hydrogeology of the Khanasser Valley

Khanasser Valley study area lies between two hill ranges; the Jabal Shbeith in the east and the Jabal Al Hoss in the west, and is located approximately 70 km southeast of Aleppo City. The drainage of the northern part of the valley is towards the Jaboul salt lake, while the drainage of the southern part is towards the Adami depression in the south, (Figs. 1 and 2). Fig. 3 shows a geological cross-section along the transverse geoelectrical profile TP5.

The groundwater extraction in the Khanasser Valley is achieved through three aquifers. The deepest one related to upper Cretaceous is at 400 m below ground level. The second one is the Paleocene-Lower Eocene limestone aquifer of a low productivity (*ACSAD, 1984*), its average hydraulic conductivity (k) is 0.0054 m/day as referred from the pumping test (*Schweers et al., 2002*). A hydraulic conductivity ranging between 0.008 m/day and 0.5 m/day for the Paleogene formation was already revealed by *Lengiprovodkhoz Institute (1987)*.

In the central part of Khanasser valley, the paleogene strata are not very thick; about 50 m of lower Eocene and Paleocene are found above the Maestrichtian. The most transmissive third aquifer in the region is the Quaternary water bearing formations, that are situated near the surface, and covered by some of 10 m of alluvial and proluvial soil. The direct recharge from rainwater as well as infiltrating runoff and subsurface flow from the slopes of Jabal Al Hoss and Jabal Shbeith are the main source for this aquifer. The substantial increase in groundwater withdrawal from the upper, unconfined aquifer system observed during the last two decades is due to the rapid development of motorized irrigation wells. Khanasser valley might be affected by salt water intrusion from the Jaboul salt lake as indicated by the analysis and the groundwater monitoring, where considerable changes in quality and water level are observed since 1998 (*Hoogeveen and Zobisch, 1999*).

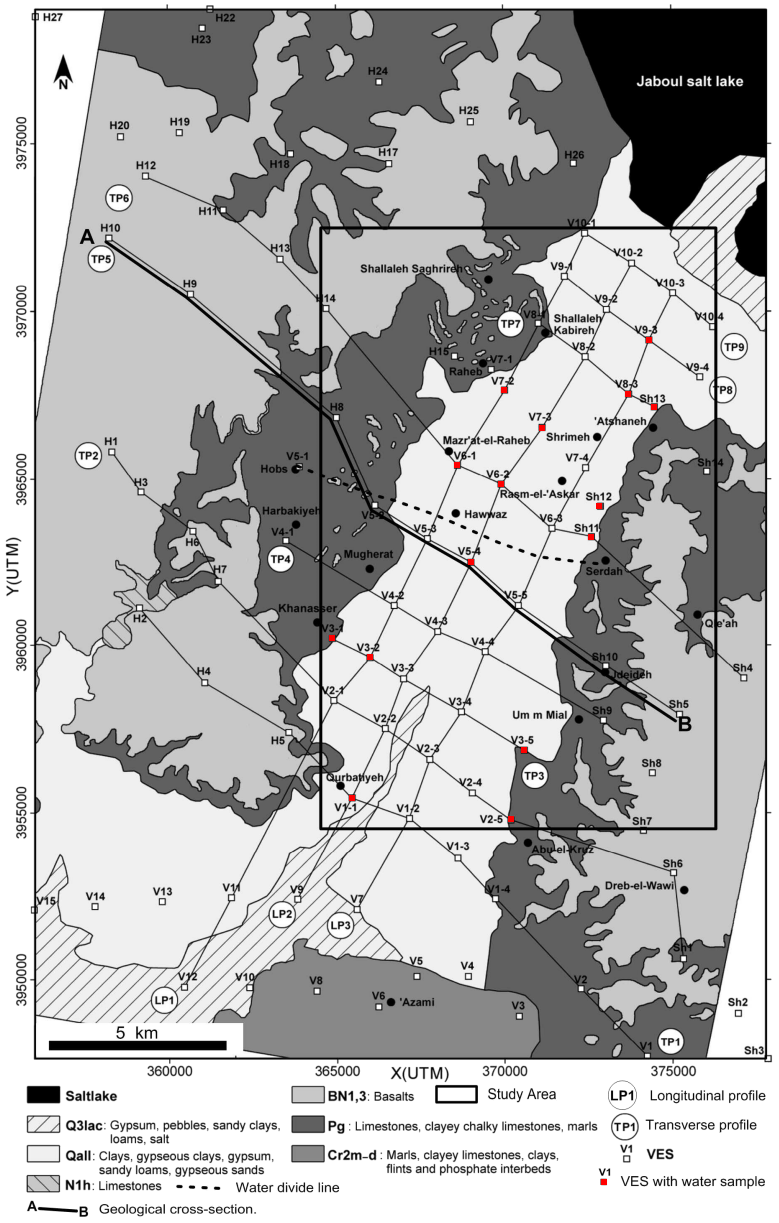

Fig. 2. Geological map of Khanasser valley and its surroundings (after *Ponikarov and Mikhailov, 1964*), with the locations of VES soundings (*Asfahani, 2016*).

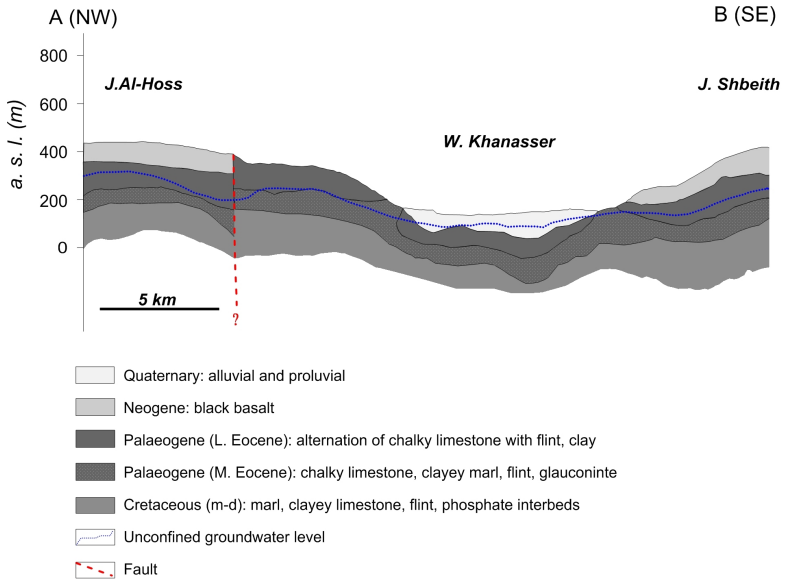

Fig. 3. Geological cross-section along the transverse geoelectrical profile TP5 (*Asfahani, 2013*).

3. VES measurements and interpretation

Schlumberger configuration was used during the Khanasser Valley research program to carry out ninety-six vertical electrical resistivity soundings VES, where their locations are shown on Fig. 2 (*Asfahani, 2010a*, and *Asfahani, 2007a*).

The AB/2 current electrode spacing was ranged for all the VES soundings between a minimum of 3 m and a maximum of 500 m.

The two current electrodes (A and B) are symmetrically expanded about the centre of the spread, while the potential electrodes (M and N) remain fixed. The apparent resistivity (ϱa) for a given position of the current and potential electrodes is written by the following equation:

$$\rho a = \frac{2\pi}{\frac{1}{AM} - \frac{1}{BM} - \frac{1}{AN} + \frac{1}{BN}} \frac{\Delta V}{I},$$

where I is the current introduced into the earth, ΔV is the potential dif-

ference between the potential electrodes, and AM, BN, AN and BN are interelectrodic spacing.

Curve matching technique with the use of master curves is practiced to interpret the field resistivity curves (*Orellana and Mooney, 1966*), and to get the initial determination of resistivities and thicknesses of corresponding layers (initial approximate model). An inverse technique program is thereafter used to correctly interpret the initial model parameters, until a goodness of fit between the resistivity field curve and the computed regenerated curve is obtained (*Zohdy, 1989; Zohdy and Bisdorf, 1989*). The one-dimensional medium 1D is assumed in the studied Khanasser region.

Fig. 4 shows a field VES example at the point V10-4 and its 1D interpretative model.

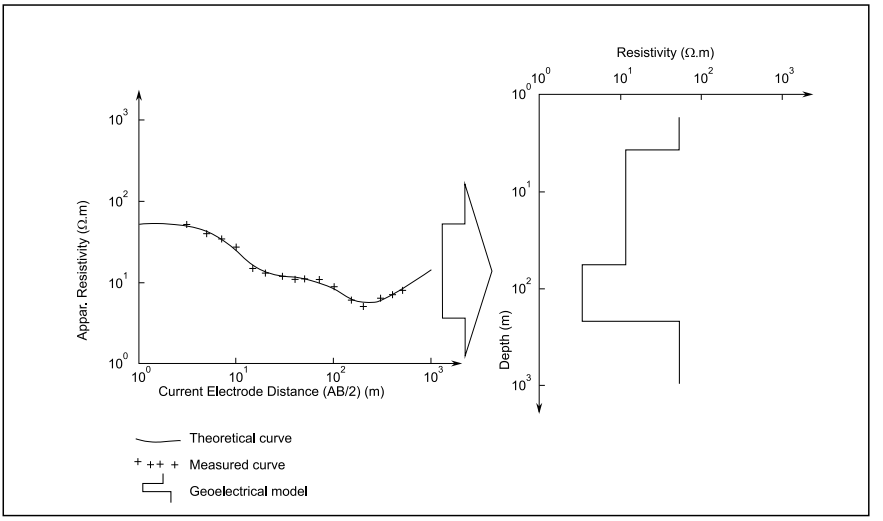

Fig. 4. Field VES example and its 1D interpretation at the location V10-4.

The 1D quantitative interpretations of these ninety six VES, distributed on the twelve profiles, (both transverse and longitudinal) enabled (*Asfahani, 2007a*) identification of both the geometry of the Khanasser Valley and the geoelectrical characteristics of Quaternary, Paleogene and Maistrechtian deposits. Fig. 5 presents the geoelectrical interpretative section established for the VES distribution along the TP5 transverse profile (TP5 corresponds to the geological section shown in Figs. 2 and 3), which shows the resistivity

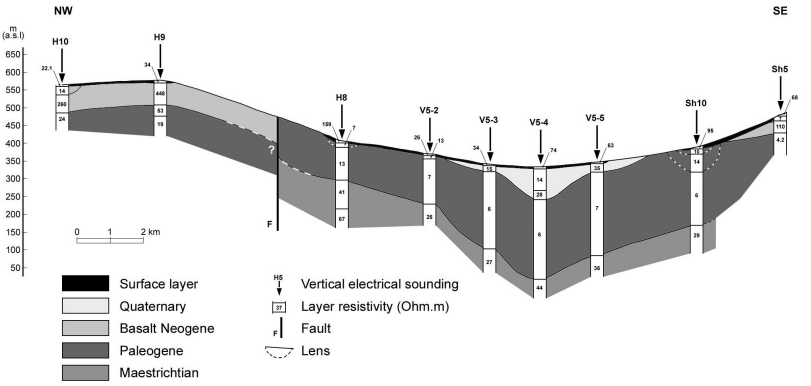

Fig. 5. Geoelectrical interpretation along TP5 (*Asfahani, 2013*).

and thickness values of the Quaternary and Paleogene aquifers.

Asfahani (2007a) has indicated to the presence of two main geological structures, one in the north and the other in the south of the line joining the towns of Hobs and Sirdah. This observation has been confirmed for all the geoelectrical maps corresponding to different spacings AB/2 (from 3 m to 500 m), revealing that a clear deep tectonic effect is present along this joining line.

4. Artificial Neural Networks

An Artificial Neural Network (ANN), like their biological analogues consists of a number of interconnected processing neurons, which are logically arranged in several layers that interact with each other through weighted connections. ANN can be used as mathematical tools that have found several applications in a wide range of research areas (*Basheer and Hajmeer, 2000*). Moreover, it has been proven theoretically that multilayer feedforward networks called Multi Layer perceptron (MLP) are universal approximators (*Hornik et al., 1989; Hornik, 1991*).

A MLP consists of an input layer, an output layer and several hidden layers. Node in a MLP network is called a neuron as shown in Fig. 6. It includes a summer and a nonlinear activation function g. The number of neurons in each layer and the number of layers in the network depend on the nature of the problem. The number of hidden nodes is a critical parameter

of any MLP. Too many nodes may cause over fitting the data, thus resulting in poor generalization on data not used for training. On the other hand, too few hidden nodes will cause under fitting of the model, which will therefore be insufficiently accurate. Most of the mathematics behind the connections and processing within the nodes are in fact linear combinations (*Basheer and Hajmeer, 2000*).

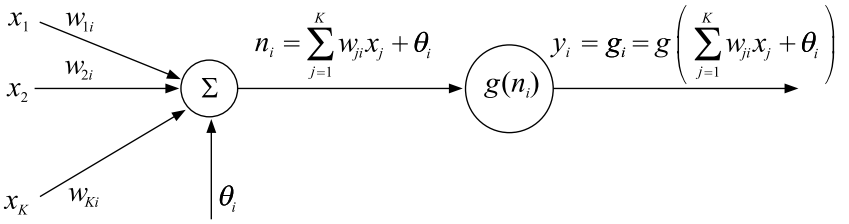

Fig. 6. Single neuron model.

The inputs x_k, $k = 1, \ldots, K$ to the neuron are multiplied by scalar weights w_{ki} and summed up together with the constant bias term θ_i. The scalar weights determine the nature and strength of the influence between the interconnected neurons. Each neuron is connected to all the neurons in the next layer. The resulting η_i is the input to the activation function g. The activation function was originally chosen to be a relay function, but for mathematical convenience a hyperbolic tangent (tanh) or a sigmoid function are most commonly used.

The output of node i becomes:

$$y_i = g\left(\sum_{j=1}^{K} w_{ji}x_j + \theta_i\right). \tag{1}$$

A MLP network is formed by connecting of several nodes in parallel and series, where a typical network is shown in Fig. 7.

The output y_i of the network becomes:

$$y_i = g\left(\sum_{j=1}^{3} w_{ji}^2 g\left(n_j^1\right) + \theta_j^2\right) = g\left(\sum_{j=1}^{3} w_{ji}^2 g\left(\sum_{k=1}^{K} w_{ji}^1 x_k + \theta_j^1\right) + \theta_j^2\right). \tag{2}$$

From (2) we can conclude that a MLP network is a nonlinear parameterized map from input space $\mathbf{X}$ to output space $\mathbf{Y}$. The parameters are the

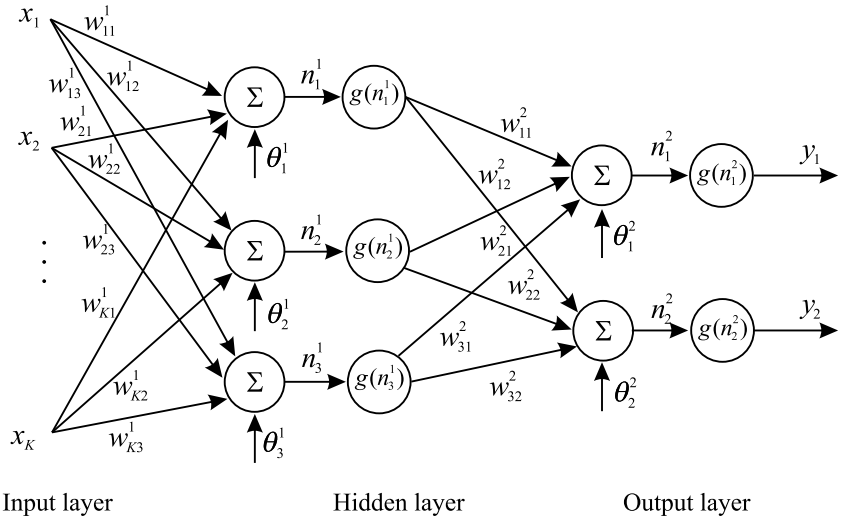

Fig. 7. A network with one hidden layer.

weights w_{ij}^k and the biases θ_j^k. Activation functions g are assumed to be the same in each layer and known in advance. The same activation function g in the figure is used in all layers.

Given input-output data (x_i, y_i), $i = 1, 2, \ldots, N$ finding the best MLP network is formulated as a data fitting problem. The parameters to be determined are (w_{ij}^k, θ_j^k).

The procedure functions as follows; the designer has to fix the structure of the MLP network architecture and the number of hidden layers and neurons (nodes) in each layer. The activation functions for each layer are selected and assumed to be known at this stage. The weights and biases are the unknown parameters to be estimated.

Several algorithms exist for determining the network parameters. The algorithms in neural network literature are called *learning* or *teaching* algorithms, and belong to *parameter estimation* algorithms in the system identification.

The most well-known are back-propagation and Levenberg-Marquardt algorithms. Back-propagation is a gradient based algorithm, which has many variants. Levenberg-Marquardt is usually more efficient, but needs more computer memory. We will concentrate herein only on using the teaching

algorithms. The procedure of teaching algorithms for multilayer perceptron networks is summarized as follows:

1. At first the structure of the network is defined. Activation functions are chosen in the network, where the network parameters of weights and biases are initialized.
2. The parameters associated with the training algorithm as error goal, maximum number of epochs (iterations), etc, are defined.
3. The training algorithm is called.

After determining the neural network, the result is first tested by simulating the output of the neural network with the measured input data. This is compared with the measured outputs. Final validation must be carried out with independent data.

5. Application to hydraulic parameters estimation

As mentioned in section 2, ANN act as universal function approximators. This makes them useful in modelling problems in which the relation between dependent and independent variables is poorly understood. The ability of ANN is used in this paper to provide a data-driven approximation of the relation between hydraulic conductivity K and the saturated aquifer resistivity ρ_{rock} and the saturated thickness of the Quaternary aquifer h and between transmissivity T and ρ_{rock} and h as illustrated in Fig. 8.

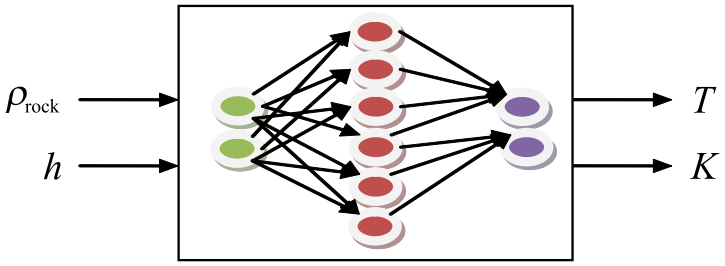

Fig. 8. Black box model of ANN used in this work.

Applying ANN requires the measurement of hydraulic conductivity and transmissivity using pumping tests which are expensive and complex to operate. Four pumping tests are only available in this work (*Asfahani, 2016*),

which are not sufficient to train ANN. The computed values of hydraulic conductivity and transmissivity based on VES measurements, recently obtained by *Asfahani (2016)* and additional four available pumping test measured values are therefore used to train ANN.

The proposed approach described herewith based on Artificial Neural Network is established as follows:

1. Firstly, carry out VES measurements in the locations where water samples related to Quaternary aquifer are available to evaluate the water resistivity ρ_w. Fifteen VES measurements have been measured and identified as close to the water sample locations. Those 15 VES soundings have been interpreted quantitatively, where the resulting resistivity and thickness of the saturated Quaternary aquifer (ρ_{rock} and h) are shown in Table 1 (*Asfahani, 2016*).
2. Determine the formation factor F used in Archie's law 1942 (*Archie, 1942*).
3. Compute the corresponding hydraulic conductivity K by using Salem's formula 2001 (*Salem, 2001; Asfahani, 2016*).
4. Compute the aquifer transmissivity T by knowing of the average $\bar{K}$ of hydraulic conductivity and h.
5. Train an artificial neural network using the data computed in step 2, 3, 4 and shown in Table 1.
6. Secondly, carry out VES measurements in the locations where no water samples exist.
7. Use the neural network trained in step 5 to extrapolate the hydraulic conductivity K and transmissivity T in VES locations, even where no water samples exist.

The formation factor F used in Archie's law in its general form is computed as the ratio of ρ_{rock} and ρ_w as follows:

$$F = \frac{\rho_{\text{rock}}}{\rho_w}\,, \tag{3}$$

where ρ_{rock} is the saturated aquifer resistivity estimated from the quantitative interpretation of (VES), and ρ_w is the pore fluid resistivity. Water resistivity ρ_w is obtained through converting water conductivity.

Salem's formula 2001 which takes only the groundwater salinity into consideration relates hydraulic conductivity K with formation factor F obtained by using VES method. It is applied to obtain the hydraulic conductivity K as follows:

$$K = 0.66528 * F^{2.09} . \tag{4}$$

The following equation is used to compute the transmissivity T for the interpreted fifteen VES as follows:

$$T = \bar{K} * h , \tag{5}$$

where $\bar{K}$ is the average of hydraulic conductivity of the available fifteen water samples shown in Table 1.

6. Results and discussion

MATLAB Neural Network Toolbox is used to create and train ANN with fitting capability to evaluate the hydraulic conductivity and transmissivity (*MATLAB, 2009*). The MATLAB commands used in the procedure are *newff*, *train* and *sim*. The *train* procedure requires measured input and measured outputs data. The measured inputs in this work are the resulting thickness and resistivity of the saturated Quaternary aquifer (ρ_{rock} and h) shown in Table 1, while the measured outputs are the computed values of K and T in the 15 VES locations, where water samples related to Quaternary aquifer are available.

Four available measured values of K using pumping test are used instead of the calculated K of VES ones at VES locations of V1-1 (at the locations of Qurbatieh), V3-1 (Khanasser), V5-4 (Batha), and V6-2 (Rasm Askar), where the hydraulic conductivity were 1.55 m/day, 4.4 m/day, 6.56 m/day, and 54.4 m/day respectively (*Schweers et al., 2002*).

The training error of the ANN is shown in Fig. 9. The goal error is reached after 600 training epoch and the performance is quite acceptable.

The results shown in Table 1 are used for applying the developed approach, and for training an ANN. The average aquifer water resistivity ρ_w of the 15 water samplings is 3.35 Ω.m. It is rather used for computing the formation factor F expressed in Eq. (3).

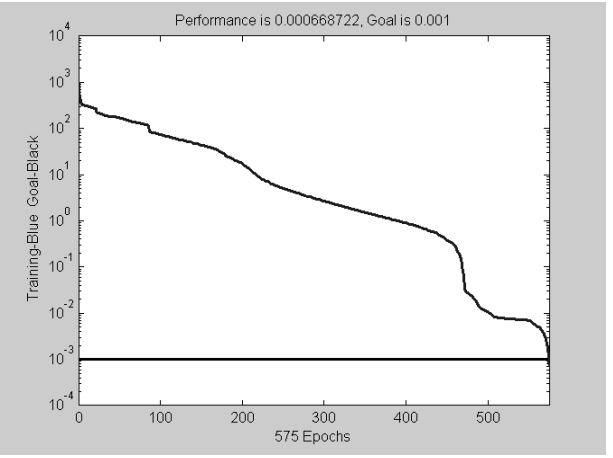

Fig. 9. Training error convergence.

Figs. 10a and 10b show the variations of both resistivity ρ and thickness h of the Quaternary aquifer for the 34 VES locations (15 VES with water samples and 19 VES without water samples) in the Khanasser valley.

Table 1. Data used to train ANN.

Location	$\boldsymbol{\rho_w}$ **(Ω.m)**	$\boldsymbol{\rho_{rock}}$ **(Ω.m)**	$\boldsymbol{h}$ **(m)**	$\boldsymbol{K}$ **(m/day)**	$\boldsymbol{K^*}$ **(m/day)**	$\boldsymbol{T}$ **(m²/day)**
V6-1	3.03	8.5	12	4.65		165.6
V9-3	1.3	11	22.5	7.98		310.5
V2-5	2.16	9.6	23.8	6		328.44
V1-1	1.79	6.5	31.4	2.65	1.55	433.32
Sh11	2.506	30	31.9			440.22
Sh12	7.44	15.5	25	16.3		345
Sh13	4.52	9	10	5.25		138
V8-3	3.47	17	11.5	19.82		158.7
V3-1	6.85	10	7.7	6.54	4.4	106.26
V3-2	6.02	15	25	15		345
V7-2	4.33	16	6	17.5		82.8
V7-3	3.03	16	5.7	17.5		78.66
V3-5	1.67	19	12.9	25		178.02
V5-4	1.2	14	59	13	6.56	814.2
V6-2	1	23	17.2	37	54.4	237.36

K^* is the pumping test value.

The hydraulic conductivity estimated according to Salem formula varies between a minimum of 2.65 m/day at VES location V1-1 and a maximum of 37 m/day at VES location V6-2 with an average of 13.8 m/day and a standard deviation of 9.4 m/day. The transmissivity is evaluated by using Eq. (5), and by using an average $\bar{K}$ of 13.8 m/day. It varies between a minimum of 79 m^2/day at the VES location V7-3 and a maximum of 814 m^2/day at the VES location V5-4 with an average of 277 m^2/day.

The application of the resulting trained ANN allows obtaining K and T in nineteen VES points, where no water samples exist. This is done to characterize as a first approximation the Quaternary aquifer in the Khanasser valley (Table 2). The conductivity and transmissivity values shown in Table 2 are directly obtained by using the trained ANN. E_K and E_T in the Table 2 are the absolute difference between $K$and T values computed using ANN and those computed using the approach proposed in (*Asfahani, 2016*). E_K

Table 2. Calculated hydraulic conductivity K and transmissivity T by ANN, in VES locations where no water samples exist.

Location	h **(m)**	$\rho_{\mathbf{rock}}$ **(Ω.m)**	K **(m/day)**	T **(m^2/day)**	E_K	E_T
V10-4	53	12	7.43	396.88	0.84	41.66
V10-3	18	7	10.67	207.74	0.03	15.05
V10-1	34	10	8.65	312.68	0.05	16.83
V10-2	40	15	10.52	386.57	0	34.61
V9-1	21	15	13.08	276.26	0.43	7.54
V9-2	50	4.3	5.22	207.60	0.51	27.99
V9-4	21	9	8.62	173.93	2.00	49.13
V8-2	16.7	11	13.76	242.24	0.56	21.74
V6-3	35	17	13.03	397.05	1.07	21.72
V5-3	15	15	17.19	248.28	1.17	7.87
V5-5	14	36	28.31	383.68	1.54	8.77
V4-3	4.5	22	40.08	180.05	0.16	0.38
V3-3	19	15	15.12	242.29	0.95	27.04
V3-4	11.8	26	25.05	253.33	1.34	26.51
V2-1	15	43	28.76	426.29	0.76	16.59
V2-2	9	6.6	17.16	141.53	0.68	19.05
V2-3	8.5	8	18.80	147.33	0.58	17.40
V2-4	14	11.5	12.75	240.41	2.21	30.85
V1-2	58	10	6.92	413.83	0.17	2.29

varies between a minimum of 0, and a maximum of 2.21 m/day, with an average of 0.97 m/day and a standard deviation of 0.64 m/day. E_T varies between a minimum of 0.38 m^2/day and a maximum of 49.13 m^2/day, with an average of 20.68 m^2/day and a standard deviation of 12.87 m^2/day.

The hydraulic conductivity values K for the 19 VES points vary between a minimum of 5.22 m/day at VES location V9-2, and a maximum of 40.08 m/day at VES location V4-3, with an average of 15.85 m/day and a standard deviation of 9.00 m/day.

The transmissivity values for the 19 VES vary between a minimum of 141.53 m^2/day at VES location V2-2, and a maximum of 426 m^2/day at VES location V2-1, with an average of 277.79 m^2/day and a standard deviation of 95.56 m^2/day. Table 3 shows the statistical results of K and T for the 19 VES points obtained by using ANN technique.

Table 3. statistical parameters using 19 VES points with no water samples.

	h (m)	ρ_{rock} (Ω.m)	K (m/day)	T (m^2/day)	E_K	E_T
Min	4.5	4.3	5.22	141.53	0	0.38
Max	59	43	40.08	426.29	2.21	49.13
Average	22	14.8	15.85	277.79	0.79	20.68
SD	15	8.5	9.00	95.56	0.64	12.87

The hydraulic conductivity values K for the total of thirty four VES points (15 VES with water samples, and 19 VES with no water samples) vary between a minimum of 1.55 m/day at the VES location V1-1, and a maximum of 54.4 m/day at the VES location V6-2, with an average of 15.24 m/day and a standard deviation of 11 m/day as shown in Fig. 10c.

The transmissivity values for the total of thirty four VES points (15 VES with water samples, and 19 VES with no water samples) vary between a minimum of 78.66 m^2/day at the VES location V7-3, and a maximum of 814.2 m^2/day at the VES location V5-4, with an average of 277.65 m^2/day and a standard deviation of 143.58 m^2/day as shown in Fig. 10d.

The established transmisivity map (Fig. 10d) clearly indicates a distinct transmissive structure at the south of Hobs-Sirdah joining line delineated by (*Asfahani, 2007a*). It is low at the north of this joining line and increases towards the Sabkha.

The geophysical and hydrogeological parameters computed for the Qua-

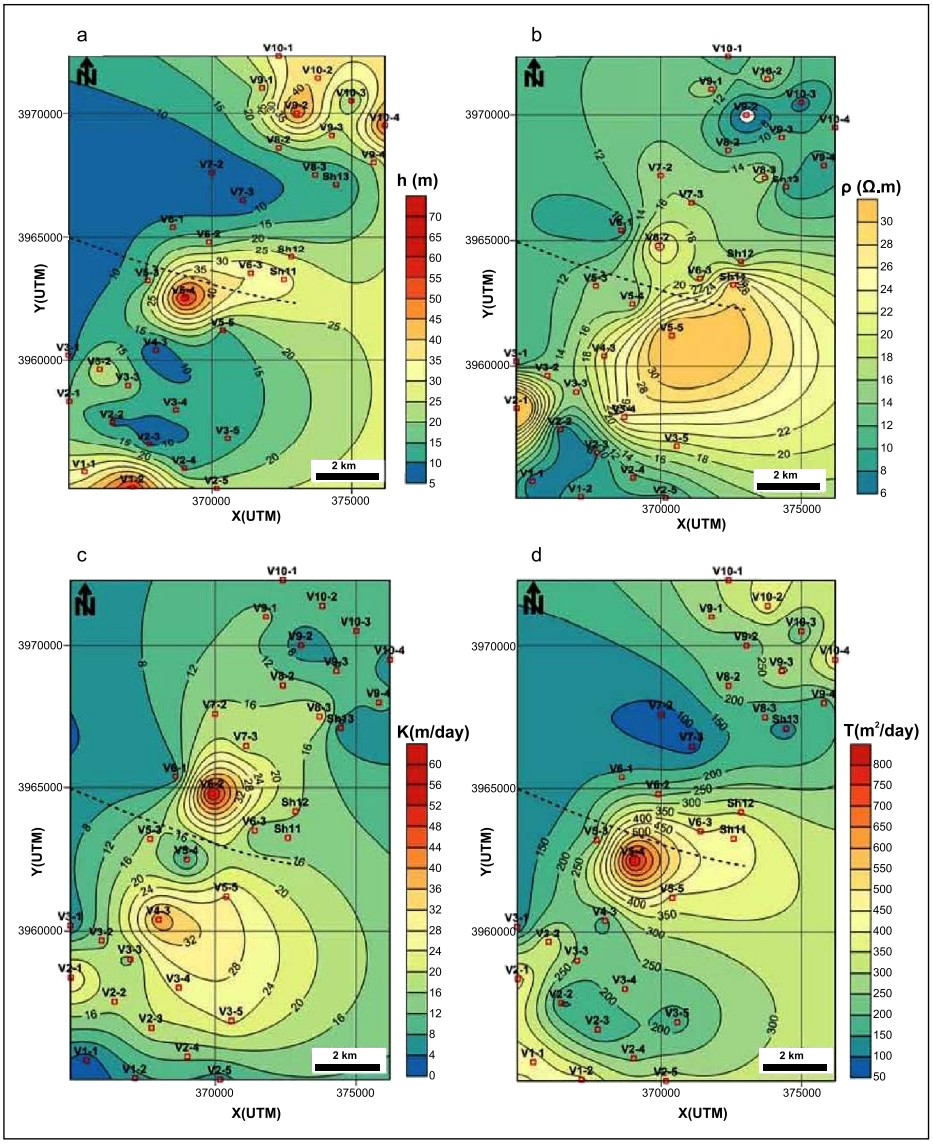

Fig. 10. a: Thickness of Quaternary aquifer h in 34 VES locations in the study area, b: Resistivity ρ of Quaternary aquifer in 34 VES locations in the study area, c: Hydraulic conductivity K of Quaternary aquifer in 34 VES locations in the study area, d: Transmissivity T of Quaternary aquifer in 34 VES locations in the study area.

ternary aquifer at the totality of thirty four VES points in the Khanasser valley are summarized in the Table 4.

Table 4. Geophysical and hydrological parameters at 34 VES points for Quaternary aquifer in the Khanasser valley, Syria.

	ρ_{rock} (Ω.m)	h (m)	K (m/day)	T (m²/day)
Min	4.3	4.5	1.55	78.66
Max	43	59	54	814.2
Average	14.8	22	15.24	277.65
SD	8.5	15	10.97	143.58

The high transmissivity and yields is related directly to the high thickness of alluvial gravels and sands, labelled as rammel aswad of the Quaternary aquifer in the Khanasser valley. The large differences and the drastic change in the productivity of wells is due to sharpen lateral and vertical variations of rammel aswad from place to place even in very short distances.

The transmissivity distribution obtained geophysically by applying the developed ANN approach for characterizing the Quaternary aquifer in the Khanasser valley is in a good agreement with the field hydrogeological observations. This proves the possibility of applying this technique to characterize the aquifer systems in the semi-arid regions worldwide.

7. Conclusion

A new alternative approach based on using both artificial neural network ANN technique and Vertical electrical sounding (VES) techniques is proposed to compute the hydraulic conductivity K and the transmissivity T of an aquifer.

We train a neural network in the VES locations, where available water samples exist to estimate the hydraulic conductivity and transmissivity. This trained neural network is required to extrapolate the hydraulic conductivity and transmissivity in the VES locations without water samples.

According to this ANN approach, the hydraulic conductivity and the transmissivity of the Quaternary aquifer in the Khanasser valley, Northern Syria are computed. We find an acceptable agreement between the hydraulic conductivity values obtained by the ANN approach and the real hydrolog-

ical situation, obtained by the pumping test, which range between 0.864 and 8.64 m/day. The main advantage of ANN approach is the possibility to integrate VES measurements and pumping test, and no intermediate empirical relations are needed. ANN approach can provide a greater accuracy in predicting K and T if more pumping test were available, and it can be easily extended using additional input parameters as soil porosity and density which could potentially further increase the performance. The easy ANN approach is recommended to be extended for treating other hydrogeological problems related to semi-arid regions worldwide.

Acknowledgements. Authors would like to thank Dr. I. Othman, General Director of Syrian Atomic Energy Commission for permission to publish this research work. Cordial thanks are to the anonymous reviewers, particularly Prof. Norbert Péter Szabó for their suggestions, remarks and critics that considerably improve the final version of this paper.

References

ACSAD, 1984: Water resources map of the Arab countries. The Arab Center for the Studies of Arid Zones and Dry Lands, Damascus, Syria.

Archie E., 1942: The electrical resistivity log as an aid in determining some reservoir characterestics. Technical Publication 1422, Petroleum Technology. American Institute of Mining and Metallurgical Engineer, New York, USA, 8.

Arétouyap Z., Nouayou R., Njandjock Nouck P., Asfahani J., 2015: Aquifers productivity in the Pan-African context. J. Earth Syst. Sci., **124**, 3, 527–539, Indian Academy of Sciences, doi: 10.1007/s12040-015-0561-1.

Arétouyap Z., Bisso D., Méli'i J. L., Njandjock Nouck P., Njoya A., Asfahani J., 2019a: Hydraulic parameters evaluation of the Pan-African aquifer by applying an alternative geoelectrical approach based on vertical electrical soundings. Geofís. Int., **58**, 2, 113–126, doi: 10.22201/igeof.00167169p.2018.58.2.1964.

Arétouyap Z., Bisso D., Njandjock Nouck P., Amougou Menkpa L. E., Asfahani J., 2019b: Hydrogeophysical Characteristics of Pan-African Aquifer Specified Through an Alternative Approach Based on the Interpretation of Vertical Electrical Sounding Data in the Adamawa Region, Central Africa. Nat. Resour. Res., **28**, 63–77, doi: 10.1007/s11053-018-9373-8.

Asfahani J., 2007a: Geoelectrical Investigation for Characterizing the Hydrogeological Conditions in Semi-arid Region in Khanasser Valley, Syria. J. Arid Environ., **68**, 1, 31–52, doi: 10.1016/j.jaridenv.2006.03.028.

Asfahani J., 2007b: Neogene aquifer properties specified through the interpretation of electrical sounding data, Sallamiyeh region, central Syria. Hydrol. Process., **21**, 21, 2934-2943, doi: 10.1002/hyp.6510.

Asfahani J., 2007c: Electrical Earth Resistivity surveying for delineating the characteristics of ground water in semiarid region in Khanaser Valley, Northern Syria. Hydrol. Process., **21**, 8, 1085–1097, doi: 10.1002/hyp.6290.

Asfahani J., 2010a: Application of surfacial geoelectrical resistivity technique in hydrogeology domain for characterizing saline groundwater in semi arid regions. In: Veress B., Szigethy J. (Eds.): Horizons in Earth Science Research Series, Volume 1, NOVA Science Publishers, 351–381.

Asfahani J., 2010b: Electrical resistivity investigations for guiding and controling fresh water well drilling in semi arid region in Khanasser valley, Northern Syria. Acta Geophys., **59**, 1, 139–154, doi: 10.2478/s11600-010-0031-8.

Asfahani J., 2013: Groundwater potential estimation using vertical electrical sounding measurements in the semi-arid Khanasser Valley region, Syria. Hydrol. Sci. J., **58**, 2, 468–482, doi: 10.1080/02626667.2012.751109.

Asfahani J., 2016: Hydraulic parameters estimation by using an approach based on vertical electrical soundings (VES) in the semi-arid Khanasser valley region, Syria. J. Afr. Earth Sci., **117**, 196–206, doi: 10.1016/j.jafrearsci.2016.01.018.

Basheer I. A., Hajmeer M., 2000: Artificial neural networks: Fundamentals computing design and application. J. Microbiol. Methods, **43**, 1, 3–31, doi: 10.1016/S0167-7012(00)00201-3.

Dhakate R., Singh V. S., 2005: Estimation of hydraulic parameters from surface geophysical methods, Kaliapani Ultramafic Complex, Orissa, India. J. Environ. Hydrol., **13**, paper 12.

De Lima O. A. L., Niwas S., 2000: Estimation of hydraulic parameters of shaly sandstone aquifers from geological measurements. J. Hydrol., **235**, 1-2, 12–26, doi: 10.1016/S0022-1694(00)00256-0.

Frohlich R. K., 1994: The electric-hydraulic relationship. A geophysical model. Trends in hydrogeology, **1**, 347–358.

Frohlich R. K., Fisher J., Summerly E., 1996: Electric-hydraulic conductivity correlation in fractured crystaline bedrock: Central Landfill, Islande, USA. J. Appl. Geoph., **35**, 4, 249–259, doi: 10.1016/0926-9851(96)00028-6.

Heigold P. C., Gilkeson R. H., Cartwright K., Reed P. C., 1979: Aquifer transmissivity from surfacial electrical methods. Groundwater, **17**, 4, 338–345, doi: 10.1111/j.1745-6584.1979.tb03326.x.

Hoogeveen R. J. A., Zobisch M., 1999: Decline of groundwater quality in Khanasser valley (Syria) due to salt-water intrusion. In: Paper Presented at International Dryland Conference, Cairo, Egypt, p. 16.

Hornik K., Stinchcombe M., White H., 1989: Multilayer feedforward networks are universal approximators. Neural Netw., **2**, 5, 359–366, doi: 10.1016/0893-6080(89)90020-8.

Hornik K., 1991: Approximation capabilities of multilayer feedforward networks. Neural Netw., **4**, 2, 251–257, doi: 10.1016/0893-6080(91)90009-T.

Lengiprovodkhoz Institute, 1987: Water resources in the Syrian desert, Syrian Arab Republic for pasture water supply. In: Hydrogeology. Moscow: USSR Ministry of Land Reclamation and Water Management, Volume 1, Book 2.

Lesmes D., Friedman S. P., 2005: Relationships between the electrical and hydrogeological properties of rocks and soils. In: Rubin Y, Hubbard S. (Eds.): Hydrogeophysics. Water science and technology library, chapter 4, **50**, 523, Springer, 87–128.

MATLAB, 2009: Neural Network Toolbox6 Users Guide.

Niwas S., De Lima O. A., 2003: Aquifer parameter estimation from surface resistivity data. Groundwater, **41**, 1, 94–99, doi: 10.1111/j.1745-6584.2003.tb02572.x.

Ponikarov V. P., Mikhailov I. A., 1964: The Geological Map of Syria, 1:200,000 and Explanatory Notes. Moscow, USSR: V.O. Technoexport, Syrian Arab Republic, Ministry of Industry, Department of Geological and Mineral Research, Damascus, Syria.

Orellana E., Mooney H. M., 1966: Master Tables and curves for vertical electrical sounding over layered structures. Interciencia, Madrid, Spain.

Schweers W., Rieser A., Bruggeman A., Abu-Zakhem B., Asfahani J., Kadkoy N., Kasmo B., 2002: Assessment of groundwater resources for sustainable management in the Khanasser valley, northwest Syria. Paper presented at ACSAD/BGR Workshop on Soil and Groundwater Quality: Monitoring Management and Protection, Amman, 23-25 June 2002.

Salem H. S., 1999: Determination of fluid transmissivity and electric transverse resistance for shallow aquifers and deep reservoirs from surface and well-log electric measurments. Hydrol. Earth Syst. Sci., **3**, 3, 421–427, doi: 10.5194/hess-3-421-1999.

Salem H. S., 2001: Modeling of lithology and hydraulic conductivity of shallow sediments from resistivity measurements using Schlumberger vertical electrical soundings. Energy Sources, **23**, 7, 599–618, doi: 10.1080/00908310119202.

Soumi G., 1991: Supplemental Irrigation Systems of the Syrian Arab Republic (SAR). In: Perrier E. R., Salkini, A. B. (Eds.): Supplemental Irrigation in the Near East and North Africa. Proceeding of a Workshop on Regional Consultation on Supplemental Irrigation. ICARDA and FAO, 7-9 December 1987, Rabat, Morocco, Kluwer Academic Publishers, Dordrecht, The Netherlands, 497–511.

Yadav G. S., Abolfazli H., 1998: Geoelectrical soundings and their relationship to hydraulic parameters in semi arid regions of Jalore, Northwestern India. J. Appl. Geoph., **39**, 1, 35–51, doi: 10.1016/S0926-9851(98)00003-2.

Zohdy A. A. R., 1989: A new method for the automatic interpretation of Schlumberger and Wenner sounding curves. Geophysics, **54**, 2, 245–253, doi: 10.1190/1.1442648.

Zohdy A. A. R., Bisdorf R. J., 1989: Schlumberger Sounding Data Processing and Interpretation Program. U.S. Geological Survey, Denver.

Contributions to Geophysics and Geodesy Vol. 50/1, 2020 (135–159)

Quantification of role of impedance contrast in site-city-interaction effects on the responses of buildings and basin

Jay Prakash NARAYAN[1,*], Prerna SINGH[2], Simran VERMA[1]

[1] Department of Earthquake Engineering, Indian Institute of Technology, Roorkee, India; e-mail: jp.narayan@eq.iitr.ac.in, vermarocks2610@gmail.com

[2] Department of Civil Engineering, Indian Institute of Technology, Delhi, India; e-mail: chhaya20singh@gmail.com

Abstract: This paper presents the role of impedance contrast (IC) at the base of 2D deep elliptical basin (shape-ratio > 0.25) in the site-city-interaction (SCI) effects on both the SH- and SV-wave responses of buildings and basin. The obtained SCI effects in the form of reduction of fundamental frequencies of building (F^{SB}_{02D}) and basin (F^{B}_{02D}), corresponding amplification and splitting of the bandwidth of fundamental mode of vibrations of both the building and basin corroborates with the findings in the past SCI studies. The F^{B}_{02D} of basin and F^{SB}_{02D} of building are unaffected by an increase of IC during site-city-interaction, even though, there is an increase of F^{B}_{02D} of basin with an increase of IC in the absence of city. A drastic increase of SCI effects on the basin response but only minor increase of SCI effects on the building response with an increase of IC is observed for both the polarizations of the S-wave. However, the rate of increase of SCI effects with IC is more in the case of SV-wave responses of buildings and basin. The obtained larger % reduction of F^{B}_{02D} and corresponding amplification in the case of SH-wave responses as compared to those in the case of SV-wave responses may be due to the larger height of B16-buildings compared to B12-buildings used in the SV-wave simulations or due to the buildings behaving as a shear beam for the SH-wave or may be due to both.

Key words: SCI effects on building and basin responses, impedance contrast, free field motion, double resonance condition and polarization of S-wave

1. Introduction

The concept of site-city-interaction (SCI) effects on the responses of building and basin was originated when the scientists were trying to find out the reasons responsible for the observed beating phenomenon along with longer duration of ground motion in the Mexico City during the 1985 Mex-

*corresponding author: e-mail: jp.narayan@eq.iitr.ac.in

doi: 10.31577/congeo.2020.50.1.7

ico earthquake (*Chávez-García and Bard, 1994; Wirgin and Bard, 1996; Stewart et al., 1999; Guéguen et al., 2002; Tsogka and Wirgin, 2003; Sahar et al., 2015; Guéguen and Colombi, 2016*). The SCI effects on both the building and basin responses are due to the combined effects of kinematic soil-structure interaction and inertial structure-soil interaction on a global scale (*Housner, 1954; Jennings, 1970; Wong and Trifunac, 1975; Kanamori et al., 1991; Stewart et al., 1999; Bard et al., 2005; 2008*). In most of the past SCI studies, the cities were considered on a sediment layer (1D basin) or in a 2D shallow basin (shape-ratio>0.25) under double-resonance condition and results were in the form of reduction of fundamental frequencies of building (F^{SB}_{02D}) and basin (F^{B}_{02D}), spectral amplification factors (SAF) at F^{SB}_{02D} and F^{B}_{02D}, as well as splitting of the bandwidth of the fundamental mode of vibrations of buildings and basin (*Guéguen and Bard, 2005; Kham et al., 2006; Groby and Wirgin, 2008; Semblat et al., 2008; Sahar and Narayan, 2016; Kumar and Narayan, 2018*). The shape-ratio of basin is the ratio of its maximum depth to half-width and double resonance is the matching of frequency of the incoming signal with the fundamental frequency of basin (F^{B}_{02D}) and further matching with the fundamental frequency of building on rock (F^{S}_{02D}). Some researchers have also studied SCI effects theoretically and have validated the outcomes with numerical and experimental results (*Schwan et al., 2016*).

The response of 2D-shallow basin is dominated with basin generated surface waves and there is a spatial variation of fundamental frequency of sediment deposit in the basin (*Narayan, 2005*). On the other hand, the response of 2D-deep basin (shape-ratio > 0.25) is dominated with a 2D-resonance phenomenon and entire basin vibrates with a single fundamental frequency (*Bard and Bouchon, 1985; Kumar and Narayan, 2018*). There is an increase of fundamental frequency of deep-basin with an increase of impedance contrast (IC) at its base (*Zhu et al., 2019*). The extensive literature review revealed that in most of the past SCI studies, the SH-wave responses of 2D-shallow basins (*Kham et al., 2006; Semblat et al., 2008; Sahar and Narayan, 2016*) and 2D-deep basins (*Kumar and Narayan, 2018; 2019*) are used. There are few studies in which SCI effects are studied using SV-wave responses (*Kumar and Narayan, 2018*). As far as we know, nobody has studied the role of impedance contrast (IC) in the SCI effects on the responses of buildings and basin. *Guéguen et al. (2019)* reported that the

fundamental frequency of the shear-beam buildings can be computed using simple relation $F^S_{02D} = V_S/4H$ (where 'H' is the height of building), but not that of bending-beam buildings. In the case of bending-beam model, the reduction of fundamental frequency with increase of height is non-linear in nature due to the reduction of bending-stiffness of the building. *Kumar and Narayan (2018)* stated that the computed fundamental frequency of 2D building block model (BBM) using SH- and SV-waves is like that of shear-beam and bending-beam models, respectively. So, there is need of quantification of polarization dependent role of IC at the base of deep-basin in the SCI effects on the responses of buildings and basin.

In order to fulfill the above identified scientific gaps, the SH- and SV-wave responses of the buildings of a city situated in a deep elliptical basin and free field motion were simulated under double-resonance condition for different IC at the base of basin. The IC has been increased by increasing the impedance of rock. The dimension and rheological parameters of the basin and building are same in all the considered site-city models for a particular polarization of the S-wave. To quantify the role of IC in the SCI effects on the responses of buildings of the city, the response of a standalone building at the centre of elliptical basin is considered as a reference one. Similarly, the role of IC in the SCI effects on the response of basin is quantified considering the response of basin in the absence of city as a reference one. The SH- and SV-wave responses of the various considered site-city models were simulated using recently developed fourth-order accurate visco-elastic staggered-grid SH- and SV-wave finite-difference (FD) programs by *Narayan and Kumar (2013)* and *Narayan and Kumar (2014)*, respectively.

2. Model parameters and salient features of FD programs

2.1. Parameters of building block model

In order to study the role of IC in the SCI effects on the SH- and SV-wave responses of buildings and basin under double resonance condition, homogenous cities made-up of 16-storey (B16) and 12-storey (B12) buildings, respectively, were considered. The height of one storey is taken as 3 m based on the prevailing Indian scenario of construction of buildings (*IS 1893-1, 2002*). Presently, it is impossible to implement the buildings

of the city in the numerical grid because of lack of computer memory and computational speed. However, the buildings can be incorporated in the numerical grid using BBM, as shown in Fig. 1, taking into account that the different modes of vibrations, dimensions, damping and weight of the BBM are same as that of the real building (*Wirgin and Bard, 1996; Bard at el., 2005; 2008; Sahar at el., 2015; Sahar and Narayan, 2016*). *Michel and Guéguen (2018)* stated that the equivalent S-wave velocity for the buildings fall in a range of 100m/s to 500m/s depending on the design and material used based seismic interferometry. The S-wave of the order of 120 m/s is taken for the BBM in the present study (*Sahar et al., 2015*). The computed fundamental frequency of B16-BBM of height 48 m for the SH-wave (SHF^{S}_{02D}) is 0.625 Hz (*Guéguen et al., 2019*). The effective density of the BBM was obtained as 350 kg/m^3 for a particular design and material property, using the weights of all the walls, beams, columns, slabs of building and the live load (*Sahar et al., 2015*). The damping in the BBM for both the P-wave and S-wave was taken as 5%. Table 1 depicts the rheological parameters for the considered building/BBM, sediment in basin and underlying rock.

Table 1. Rheological parameters for the building block model, sediment of basin and rock.

Materials	Seismic velocity (m/s)		Quality factors		Poisson's ratio (ν)	Density 'ρ' (kg/m^3)
	S-wave	P-wave	Qs	Qp		
Building	120.0	294.0	10	10.0	0.40	350
Basin	300.0	735.3	30	73.5	0.40	1800
Rock	1800.0	3117.7	180	311.0	0.25	2500

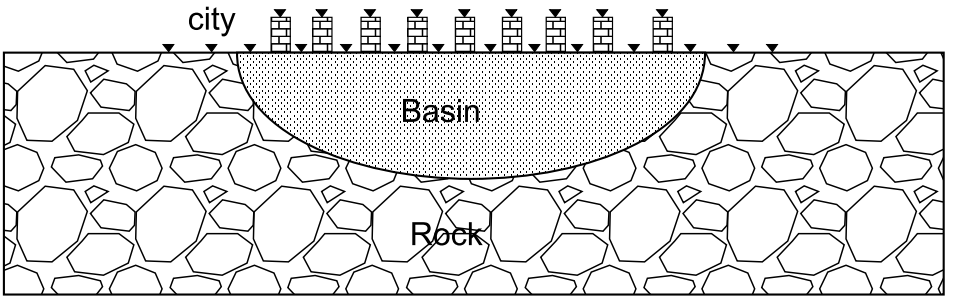

Fig. 1. Vertically exaggerated sketch for the various site-city models (Note: the considered number of buildings are nine and five in the cases of SV- and SH-wave simulations, respectively).

2.2. Salient features of FD programs

A frequency dependent damping in the time-domain simulations of the SH- and SV-wave responses of the site-city models is essential for the accurate prediction of SCI effects on the building and basin responses (*Emmerich and Korn, 1987; Kristek and Moczo, 2003*). A forth-order accurate time-domain SH- and SV-wave viscoelastic finite-difference (FD) programs were used for the simulations (*Narayan and Kumar, 2013; 2014*). These programs were written for the simulations to be carried out in the XZ-plane of the Cartesian coordinate system. The details of finalizing the input parameters like relaxation frequencies and the computation of anelastic coefficients and unrelaxed moduli are given in *Narayan and Kumar (2013; 2014)*. The centres of basin and city are collocated and are considered as a reference point for all the horizontal distance measurements. An improved vacuum formulation proposed by *Zeng et al. (2012)* is used as a free surface boundary condition. In order to avoid the edge reflections, sponge-absorbing boundary layers were used at the left, right and bottom edges of the model (*Israeli and Orszag 1981; Kumar and Narayan, 2008*).

A plane SH- and SV-wave front propagating vertically towards the free surface was generated at a desired depth in the respective FD program using various point sources at every 3 m distance along a horizontal line from left-edge to right-edge of the model. The envelops of the wave fronts of the individual point source generated a plane wave front propagating towards the free surface. The downward propagating plane wave front was absorbed by the implemented absorbing boundary condition at the bottom edge of the model. The shear stress σ_{yz} and σ_{xz} in the form of Gabor wavelet was used as a source time function (STF) to implement a point source in the cases of SH- and SV-wave simulations, respectively. The mathematical formulation for the Gabor wavelet is given below:

$$S(t) = \exp(-\alpha)\cos[\,\omega_P(t - t_S) + \varphi\,]\,, \tag{1}$$

where $\alpha = \left[\dfrac{\omega_P(t - t_S)}{\gamma}\right]^2$, ω_P is predominant frequency, γ controls the oscillatory character, t_S controls the duration and φ is phase shift. The value of parameters $f_P = 3$ Hz, $\gamma = 1.5$, $t_S = 0.33$ s and $\varphi = 0$ was used.

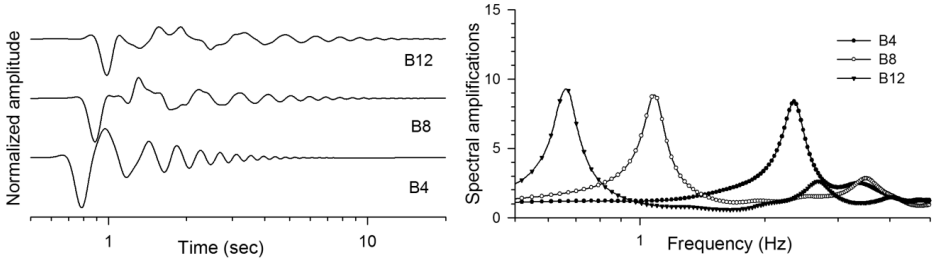

Fig. 2. The horizontal component of SV-wave responses (left) and spectral amplifications (right) at the top of B4, B8 and B12-buildings.

3. Response of standalone building on rock

In this subsection, the fundamental frequency of standalone BBM on rock is numerically computed for both the polarizations of S-wave and its variation with IC between the base of BBM and the underlying rock.

3.1. The SVF^{S}_{02D} of standalone BBM on rock

As discussed earlier, the fundamental frequency of BBM on rock for the SV-wave (SVF^{S}_{02D}) cannot be computed using simple relation $F^{S}_{02D} = V_S/4H$ since BBM behaves like a bending beam (*Kumar and Narayan, 2018*). So, to find out the SVF^{S}_{02D} of the BBM, the SV-wave responses of the considered standalone B4 (four-storey), B8 (eight-storey) and B12 (twelve-storey) buildings on rock were computed and analysed. The dimensions of B4, B8, B12-buildings are given in the Table 2. The left panel of Fig. 2 depicts the horizontal components of the SV-wave responses at the top of B4, B8 and B12-buildings. An increase of duration and decrease of amplitude of the SV-wave at the top of building can be inferred with an increase of height of

Table 2. Dimension of considered buildings, SVF^{S}_{02D} of standalone BBM on rock, SVF^{SB}_{02D} of standalone BBM in basin and corresponding SAFS.

Buildings	Height (m)	Width (m)	SVF^{S}_{02D} (Hz)	SAF at SVF^{S}_{02D}	SVF^{SB}_{02D} (Hz)	SAF at SVF^{SB}_{02D}
B12	36	60	0.66	9.18	0.64	67.27
B8	24	60	1.06	8.71	–	–
B4	12	60	2.34	8.38	–	–

building. The right panel of Fig. 2 reveals the spectral amplification factors (SAF) for the horizontal component of SV-wave at the top of B4, B8 and B12-buildings. The SAFs were computed using simply the ratio of spectra of the horizontal component of SV-wave at the top of building and that on the exposed rock. Analysis of Fig. 2 revealed a decrease of value of SVF^{S}_{02D} of the BBM on rock with an increase of height for a fixed dimension of base (*Kumar and Narayan, 2018*). The numerically obtained of the B12, B8 and B4-buildings for the SV-wave were 0.66 Hz, 1.06 Hz and 2.34 Hz, respectively (Table 2). The inferred increase of rate of decrease of of BBM with height may be due to decrease of bending stiffness of building.

3.2. Effects of IC on the response of standalone BBM on rock

In order to study the role of IC at base of basin in the SCI effects on the SH- and SV-wave responses of buildings and basin, four ICSH1–ICSH4 site-city models for the SH-wave and four ICSV1–ICSV4 site-city models for the SV-wave simulations were taken (Table 3). In all the IC models, only the impedance of rock is varied and the rheological parameters of the basin and buildings are same.

Table 3. The rheological parameters of rock for the ICSH1–ICSH4 and ICSV1–ICSV4 site-city models and impedance contrast at the base of basin and building situated on rock (Note: basin and BBM parameters are given in Table 1).

Site-city models	V_S (m/s)	V_P (m/s)	Density (g/cm^3)	Quality factor (Q_S)	Quality factor (Q_P)	IC at base of basin	IC at base of BBM
ICSH1/ICSV1	1800	3117.7	2.50	180	311	8.33	107.14
ICSH2/ICSV2	1600	2771.3	2.30	160	277	6.81	87.62
ICSH3/ICSV3	1400	2424.9	2.10	140	242	5.44	70.00
ICSH4/ICSV4	1200	2078.5	2.00	120	208	4.44	57.14

3.2.1. SH-wave responses

The SH-wave responses of the standalone B16-BBM on the rock were computed using the rheological parameters of the rock of the ICSH1–ICSH4 site-city models (Table 3). The computed SAFs of the SH-wave at the top of B16-BBM for different rock impedances are shown in the left panel of

Fig. 3a. There is an excellent match of numerically obtained SHF^S_{02D} of building as 0.62 Hz with that computed using simple relationship $F^S_{02D} = V_S/4H$, since the BBM is behaving as a shear beam model (*Guéguen et al., 2019; Kumar and Narayan, 2018; 2019*). The obtained SAFs at SHF^S_{02D} of the B16-BBM as 11.38, 11.33, 11.28 and 11.21 in the ICSH1–ICSH4 models, respectively revealed that SAF at SHF^S_{02D} was almost unaffected by the change of IC at the base of building, although corresponding ICs were 107.14, 87.62, 70.0 and 57.14, respectively (Table 3).

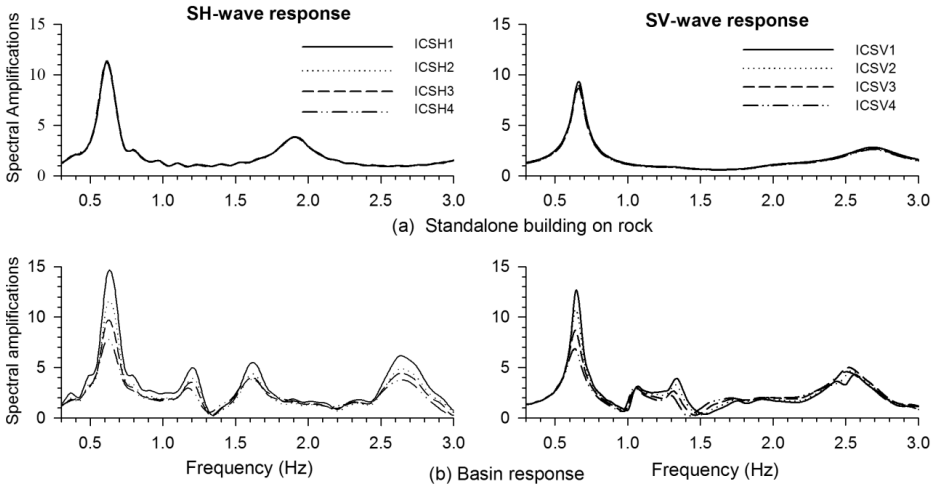

Fig. 3a-b. spectral amplifications at the top of standalone building on rock and free field motion in basin in the absence of city with impedances in the rock corresponding to the ICSH1/ICSV1–ICSH4/ICSV4, respectively.

3.2.2. SV-wave response

Similarly, the SV-wave responses of the standalone B12-BBM on the rock were computed using the rheological parameters of the rock of the ICSV1–ICSV4 site-city models (Table 3). The computed SAFs of the horizontal component of SV-wave at the top of B12-BBM for different rock impedances are shown in the right panel of Fig. 3a. A comparison of the numerically obtained SVF^S_{02D} of building (0.66 Hz) with that computed using simple relationship $F^S_{02D} = V_S/4H$ (0.83 Hz) reveals a drastic decrease of SVF^S_{02D} of the B12-BBM, since for the SV-wave, the BBM is behaving as a bending beam model (*Guéguen et al., 2019; Kumar and Narayan, 2018; 2019*). The

obtained SAFs at SVF^{S}_{02D} of the B12 building as 9.18, 8.97, 8.76 and 8.61 in the ICSV1–ICSV4 models, respectively revealed that SAF at SVF^{S}_{02D} was almost unaffected by the change of IC at the base of building (Table 3). These findings depicted that the 5% damping in the BBM has controlled the SAF at fundamental frequency and not the IC between the BBM and the underlying rock. Further, the obtained fundamental frequency of the BBM for the SH-wave (0.62 Hz) and SV-wave (0.66 Hz) were same in all the respective IC models.

4. Response of elliptical basin

The computed SHF^{S}_{02D} of the B16-BBM as 0.62Hz and SHF^{S}_{02D} of B12-BBM as 0.66 Hz in the case of all the IC models depict that the fundamental frequency of elliptical basin for the SH-wave (SHF^{B}_{02D}) and SV-wave (SVF^{B}_{02D}) should also be 0.62 Hz and 0.66 Hz, respectively to preserve the double resonance condition. *Bard and Bouchon (1985)* reported that the fundamental frequency of deep-elliptical basin for the SH-wave is lesser than for the SV-wave for a particular dimension of basin. In case of deep-basin, the entire basin vibrates with a single fundamental frequency and there is an increase of F^{B}_{02D} of basin with an increase of IC (*Bard and Bouchon, 1985; Kumar and Narayan, 2018; Zhu et al., 2019*).

4.1. SH-wave response of basin

Kumar and Narayan (2018) have given an empirical relation to predict the SHF^{B}_{02D} of deep-basin in terms of lowest 1D fundamental frequency (F^{B}_{01D}) and maximum depth 'h' for the SH-wave.

$$SHF^{B}_{02D} = F^{B}_{01D}\sqrt{1 + 1.6\left(\frac{h}{w}\right)^{2}}, \tag{2}$$

where $F^{B}_{01D} = V_S/4h$, 'h' and 'w' are the 1D lowest fundamental frequency, maximum depth and half-width of the elliptical basin, respectively. The estimated maximum depth and width ($2w$) of elliptical basin for $SHF^{B}_{02D} =$ 0.62 Hz are 150 m and 492 m, respectively, using Eq. (2). In order to find out the variation of SHF^{B}_{02D} of basin with IC, the SH-wave responses of the elliptical basin with depth 150 m and width 492 m were computed for

all the IC models. The left panel of Fig. 3b show the SAFs at a distance of 39 m from the centre of elliptical basin with ICs corresponding to the ICSH1–ICSH4 site-city models. An analysis of Fig. 3b revealed that there is minor increase of SHF^B_{02D} of basin with an increase of IC at its base (*Zhu et al., 2019; Kumar and Narayan, 2018*). For example, the obtained SHF^B_{02D} of elliptical basin are 0.638Hz, 0.627Hz, 0.626Hz and 0.621Hz in the ICSH1–ICSH4 models, respectively. There is minor mismatch of SHF^S_{02D} of building with SHF^B_{02D} of basin in the case of larger IC values.

4.2. SV-wave response of basin

Bard and Bouchon (1985) have given an empirical relation to predict the SVF^B_{02D} of deep-basin in terms of lowest 1D fundamental frequency (F^B_{01D}) for the SV-wave (*Zhu et al., 2019*).

$$SVF^B_{02D} = F^B_{01D}\sqrt{1+\left(\frac{2.9h}{w_e}\right)^2}, \tag{3}$$

where '$2w_e$' is the effective width of basin (effective width is the span over which the depth (h) is $\geq h/2$). The inferred depth, width and effective width of the elliptical basin for $SVF^B_{02D} = 0.66$ Hz are 150 m, 660 m and 505 m, respectively, using Eq. (3). To infer the variation of SVF^B_{02D} with IC, the SV-wave responses of the elliptical basin with maximum depth 150 m and width 660 m were computed for all the IC models. The right panel of Fig. 3b shows the SAFs at a distance of 36 m from the centre of elliptical basin with IC corresponding to the ICSV1–ICSV4 site-city models. Fig. 3b also revealed an increase of SVF^B_{02D} of the elliptical basin with an increase of IC (*Zhu et al., 2019; Kumar and Narayan, 2018*). The numerically obtained SVF^B_{02D} of elliptical basin as 0.662 Hz, 0.658 Hz, 0.655 Hz and 0.651 Hz in the ICSV1–ICSV4 models, respectively revealed a minor mismatch with the SVF^S_{02D} of structure (0.66 Hz) in the case of lower IC models.

5. Role of IC in SCI effects on SH-wave responses

In all the considered ICSH1–ICSH4 site-city models, five-B16 buildings of width 60 m are situated at an equal spacing of 15m in the elliptical basin.

The centre of 3rd building is at the centre of basin and the width of city is 360 m. The SH-wave responses of a standalone building at the centre of elliptical basin are used as a reference one to quantify the SCI effects on the response of buildings of the city. Similarly, the response of basin at some selected locations in the absence of city were considered as a reference one to quantify the SCI effects on the response of basin.

5.1. Standalone building at the centre of elliptical basin

The left and right panels of Fig. 4a depict the SH-wave responses at the top of standalone building situated at centre of elliptical basin and corresponding spectral amplifications, respectively in the case of ICSH1–ICSH4 site-city models. Analysis of Fig. 4a illustrated an increase of amplitude of the SH-wave with a decrease of impedance in the rock. This may be due to use of the same stress drop to generate point sources in all the IC models. The computed fundamental frequency of standalone building in basin (SHF^{SB}_{02D}) as 0.61Hz in all the IC models depicts that SHF^{SB}_{02D} of building is not affected by IC. The achieved SAF at SHF^{SB}_{02D} of building as 51.89, 48.92, 44.85 and 40.95 were 4.5, 4.3, 3.9 and 3.6 times larger than that on F^{S}_{02D} of standalone building on rock in the ICSH1–ICSH4 site-city models, respectively. The

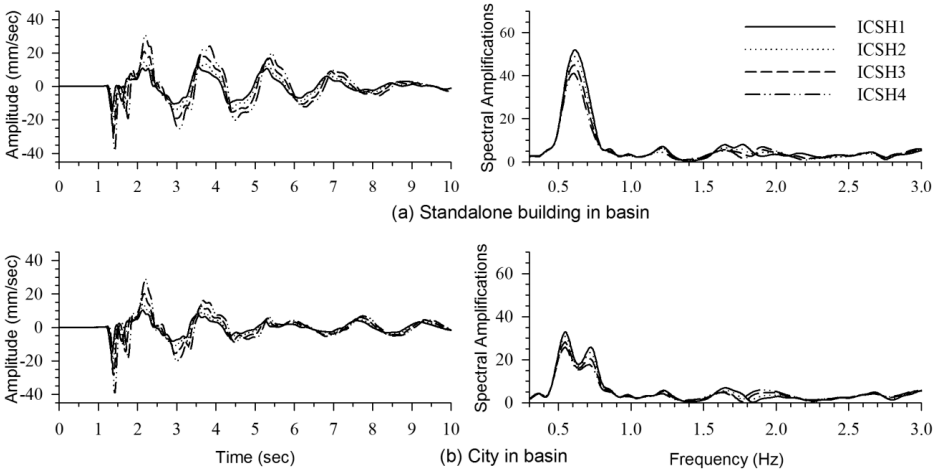

Fig. 4a-b. The SH-wave responses (left panels) and spectral amplifications (right panels) at the top of standalone building situated at the centre of elliptical basin and at the top of the building situated at the centre of city, respectively.

observed very large amplification at the top of standalone building in basin as compared to the standalone building on rock revealed effect of occurrence of double resonance phenomenon.

5.2. City situated in the elliptical basin

In this numerical experiment, the SH-wave responses of buildings of the ICSH1–ICSH4 site-city models as well as free field motion have been simulated and analysed.

5.2.1. SCI effects on the response of buildings

The SH-wave responses and corresponding SAFs at the top of 3$^{\rm rd}$ building of the ICSH1–ICSH4 site-city models is shown in the left and right panels of Fig. 4b. It is very much clear that the SCI has caused reduction of the amplitude of SH-wave, particularly in the case of later phases as compared to the respective response of standalone building in basin. The obtained SHF^{SB}_{02D} of the 3$^{\rm rd}$ building as 0.55 Hz in all the IC models revealed that SHF^{SB}_{02D} of building is almost not affected by IC. However, there is 9.8% reduction of SHF^{SB}_{02D} due to the SCI effects. The obtained SAFs at SHF^{SB}_{02D} of 3$^{\rm rd}$ building as 33.23, 31.41, 28.85 and 26.67 in the case of ICSH1–ICSH4 site-city models, respectively, revealed an increase of SAFs at SHF^{SB}_{02D} of building with an increase of IC. Table 4 reveals that SCI effects due to only 5-buildings have caused 35.96%, 35.79%, 35.67% and 34.87% reduction of SAF at SHF^{SB}_{02D} of building in the ICSH1–ICSH4 site-city models, respectively.

Similarly, the observed % reduction of SAF at F^{S}_{02D} of 3$^{\rm rd}$ building as 60.37%, 59.95%, 59.21% and 57.60% in the ICSH1–ICSH4 site-city models, respectively revealed that the reduction of SAF at SHF^{S}_{02D} was larger than that at SHF^{SB}_{02D} of the 3$^{\rm rd}$ building of the respective site-city model (Table 4). The larger % reduction of SAF at frequency SHF^{S}_{02D} may be due to the additional reduction of SAF at SHF^{S}_{02D} caused by the seismic waves emanated by the buildings during their inertial vibrations. The emanated seismic waves during inertial vibrations were out of phase to that of the incident SH-wave. There is only minor increase in % reduction of SAFs at SHF^{SB}_{02D} and SHF^{S}_{02D} with an increase of IC (Table 4). Further, the effects of minor mismatch of SHF^{S}_{02D} with SHF^{B}_{02D} has no considerable effects on the response of buildings.

Table 4. A comparisons of SAFs at F^{SB}_{02D} and F^{S}_{02D} in the case of standalone building and 3rd building of city in basin and corresponding % reduction of SAFs at F^{SB}_{02D} and F^{S}_{02D} due to the SCI effects in the ICSH1–ICSH4 and ICSV1–ICSV4 site-city models.

Site-city models	ICSH1	ICSH2	ICSH3	ICSH4
SAF at SHF^{SB}_{02D} of standalone building in basin	51.89	48.92	44.85	40.95
SAF at SHF^{SB}_{02D} of 3rd building of city	33.23	31.41	28.85	26.67
% reduction of SAF at SHF^{SB}_{02D} of 3rd building	35.96	35.79	35.69	34.87
SAF at SHF^{S}_{02D} of standalone building in basin	51.78	48.64	44.37	40.38
SAF at SHF^{S}_{02D} of 3rd building of city	20.56	19.59	18.29	17.36
% reduction of SAF at SHF^{S}_{02D} of 3rd building	60.37	59.95	59.21	57.60
Site-city models	ICSV1	ICSV2	ICSV3	ICSV4
SAF at SVF^{SB}_{02D} standalone building in basin	67.27	59.69	50.61	41.82
SAF at SVF^{SB}_{02D} of 5th building of city	34.41	31.02	26.90	22.65
% reduction of SAF at SVF^{SB}_{02D} of 5th building	48.84	48.03	46.84	45.83
SAF at SVF^{S}_{02D} standalone building in basin	61.50	54.20	45.80	37.63
SAF at SVF^{S}_{02D} of 5th building of city	20.04	18.81	17.18	15.31
% reduction of SAF at SVF^{S}_{02D} of 5th building	67.41	65.29	62.48	59.31

The left and right panels of Fig. 5a-d depict the SH-wave responses and the spectral amplifications at the top of 1st, 2nd and 3rd buildings of the ICSH1–ICSH4 site-city models, respectively. As expected, a decrease of amplitude of the SH-wave at the top of 1st, 2nd and 3rd buildings can be inferred due to an increase of impedance in the rock. Relatively larger decrease of amplitude of the SH-wave at the top of buildings situated away from the centre of city can be observed. This may be due to the decrease of basin response at its fundamental frequency (*Bard and Bouchon, 1985; Kumar and Narayan, 2018*). An increase of spectral amplifications at the top of buildings with the increase of IC can be inferred. Fig. 5 also depicts the decrease of SAF at SHF^{SB}_{02D} of building towards the edge of city. However, this decrease was very large in case of the 1st building. For example, the largest SAF obtained at SHF^{SB}_{02D} of building at the top of 1st, 2nd and 3rd buildings of the ICSH3 site-city model as 12.31, 23.86 and 28.85, respectively were 72.55%, 46.80 and 35.69% lesser as compared to the SAF obtained at the top of standalone building at the centre of the ICB3 model. Further, in the case of ICSH3 model, the obtained % reduction of SAF at

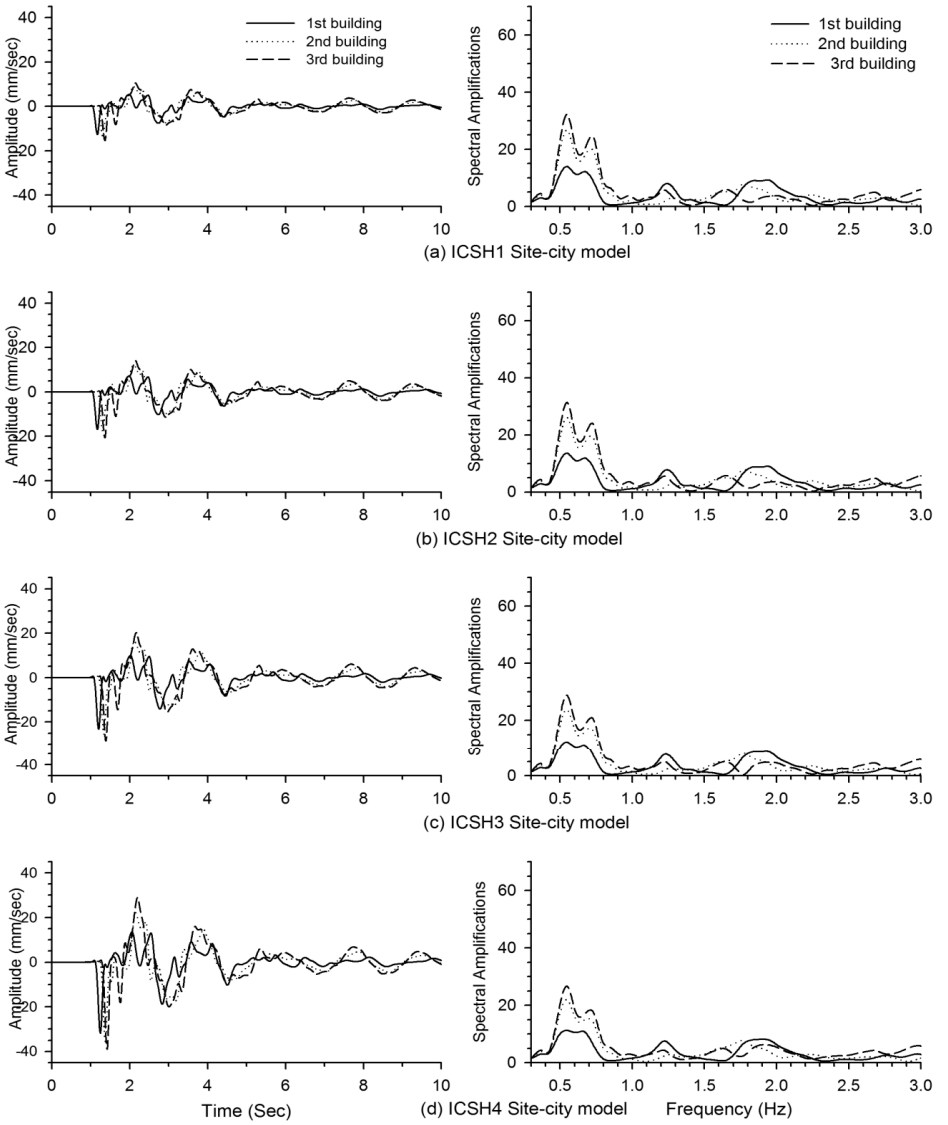

Fig. 5a-d. The SH-wave responses at the top of 1st, 2nd and 3rd buildings of the ICSH1–ICSH4 site-city models, respectively (left panels) and corresponding spectral amplifications (right panels).

SHF^{S}_{02D} at the top of 1st, 2nd and 3rd buildings as 76.17%, 64.93 and 59.21% were larger as compared to the % reduction of SAF at SHF^{SB}_{02D} of the respective building (Table 4). But, it may not be concluded that there were larger SCI effects on the responses of 1st and 2nd buildings as compared to the 3rd building. This was due to the computation of % reduction of SAF at SHF^{SB}_{02D} with respect to the reference standalone building situated at the centre of basin.

5.2.2. SCI effects on free field motion

To quantify the role of IC in the SCI effects on the response of basin, the SH-wave responses at different locations in the elliptical basin for without and with city in basin were computed for the ICSH1–ICSH4 site-city models. The selected locations in the basin were at a distance of 39 m, 114 m and 189 m towards the right of centre of basin (third receiver point was 9 m away from the edge of city). Fig. 6a-d depicts the comparison of spectral amplifications computed for with and without ICSH1–ICSH4 site-city models at different locations. Analysis of Fig. 6 revealed a decrease of spectral amplifications due to the SCI effects. The basin was vibrating with a single resonance frequency (0.53 Hz) in the presence of city in all the IC models. In contrast to this, there was minor increase of SHF^{B}_{02D} of basin with an increase of IC in the absence of city. Further, the obtained decrease of SAF at SHF^{B}_{02D} towards the edge of basin corroborates with the finding of *Bard and Bouchon (1985)*. It was interesting to note the decrease of SHF^{B}_{02D} of basin due to the SCI effects. The obtained SHF^{B}_{02D} of basin (0.53 Hz) due to SCI effects was somewhat lesser than SHF^{SB}_{02D} of building (0.55 Hz) of city.

Table 5 shows that the % age reduction of SAF at SHF^{B}_{02D} of basin as compared to that in the absence of city is increasing with increase of IC. Further, the % age reduction of SAF at SHF^{B}_{02D} of basin was decreasing towards the edge of city. For example, the obtained SAF at SHF^{B}_{02D} as 7.31, 6.22, 2.30 at 39 m, 114 m and 189 m distance from the centre of basin in the ICSH1 model was 50.40%, 35.27% and 33.90% lesser than that obtained in the absence of city. The computed % reduction of average spectral amplification (ASA) at a distance of 39 m as 11.4%, 10.11%, 9.42% and 8.26% as well as at a distance of 189 m (outside city) as 5.38%, 5.23%, 4.90% and 4.00% in the ICSH1–ICSH4 site-city models, respectively was also an

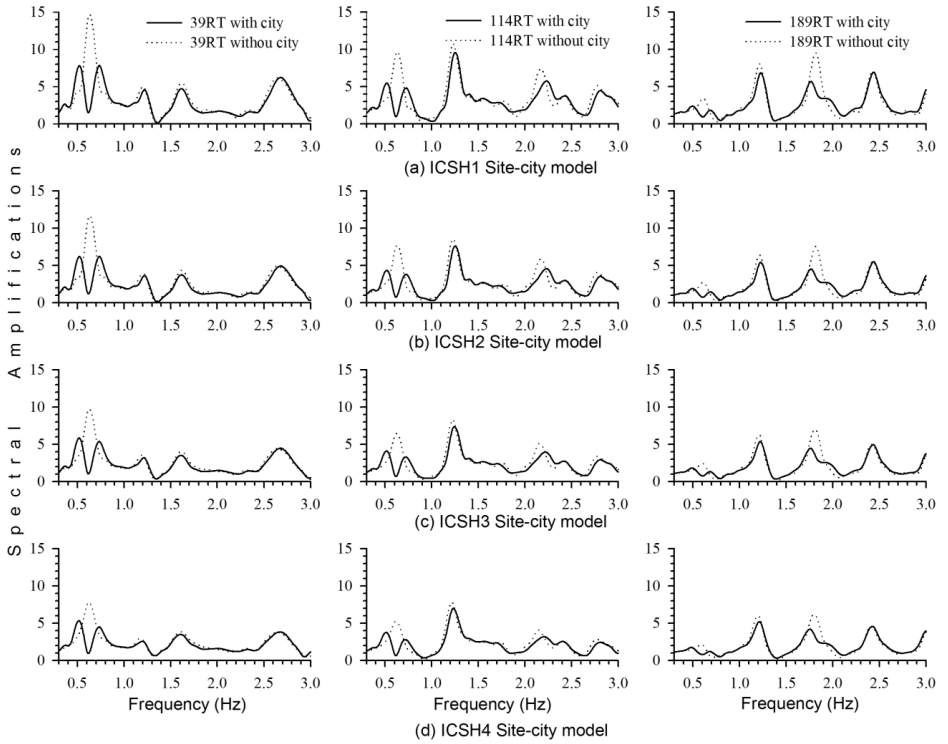

Fig. 6a-d. A comparison of spectral amplifications at different locations in the elliptical basin corresponding to with and without city in basin in the ICSH1–ICSH4 site-city models, respectively.

indicator that SCI effect was largest at the centre of city and decreasing towards the edge or outside the city (ASA is simply the average of spectral amplifications in the considered frequency bandwidth). The larger reduction of SAF at frequency SHF^{S}_{02D} was responsible for the splitting of the bandwidth of the fundamental mode of vibration of basin as was inferred in the case of building's response. The % reduction of SAF at SHF^{S}_{02D} is also increasing with increase of IC.

6. Role of IC in SCI effects on SV-wave responses

To quantify the role of IC in the SCI effects on the SV-wave responses of buildings and the basin, four ICSV1–ICSV4 site-city models were consid-

Table 5. A comparison of SAFs at F^B_{02D} of basin as well as ASA of free field motion for without and with city in basin and corresponding % reductions due to the SCI effects in the ICSH1–ICSH4 and ICSV1–ICSV4 site-city models.

Site-city models	ICSH1	ICSH2	ICSH3	ICSH4
SAF at SHF^B_{02D} for without city at 39 m	13.74	11.58	9.51	7.71
SAF at SHF^B_{02D} for with city at 39 m	7.31	6.23	5.24	4.82
% reduction in SAF at SHF^B_{02D} at 39 m	50.40	46.20	44.84	37.48
ASA at 39 m for without city	3.24	2.57	2.44	2.30
ASA at 39 m for with city	2.87	2.31	2.21	2.11
% Decrease in ASA at 39 m	11.40	10.11	9.42	8.26
Site-city models	ICSV1	ICSV2	ICSV3	ICSV4
SAF at SVF^B_{02D} for without city at 36 m	12.54	10.76	8.69	6.82
SAF at SVF^B_{02D} for with city at 36 m	7.62	7.44	6.46	5.45
% reduction in SAF at SVF^B_{02D} at 36 m	39.23	30.85	25.43	20.08
ASA at 36 m for without city	2.46	2.43	2.41	2.27
ASA at 36 m for with city	2.06	2.07	2.09	2.01
% Decrease in ASA at 36 m	16.26	14.81	13.27	11.45

ered (Tables 1–3). Fig. 1 illustrates the sketch for the vertically exaggerated site-city model with nine B12-buildings situated in the elliptical basin. The maximum depth and width of the elliptical basin were taken as 150 m and 660 m, respectively. The width of B12 buildings was taken as 60 m and spacing between two consecutive buildings was 12 m. The buildings of the city were numbered as 1st, 2nd and 9th building from left to right edge of the city. The centre of 5th building was at the centre of elliptical basin. The free field motions were computed on a horizontal array with 14-equidistant (72 m apart) receiver points, extending from 486 m left to 468 m right of the centre of elliptical basin.

6.1. Standalone building at the centre of basin

To quantify the SCI effects on the response of B12-buildings of the city, the SV-wave response of standalone B12-building at the centre of elliptical basin is considered as a reference one. Fig. 7a shows a comparison of horizontal component of the SV-wave responses at the top of standalone B12-building situated at the centre of basin (left panel) and corresponding

SAFs (right panel) in the ICSV1–ICSV4 impedance models. The double resonance phenomenon was responsible for many fold increase in spectral amplifications. For example, the obtained SAFs at SVF^{SB}_{02D} as 67.27, 59.69, 50.61 and 41.82 in the ICSV1–ICSV4 models were 7.32, 6.65, 5.77 and 4.91 times larger than those obtained at SVF^{S}_{02D} of building on rock, respectively (Table 4). Although, there was no increase of SVF^{SB}_{02D} of building with an increase of IC, but, the interaction of standalone building with basin has caused a minor reduction of SVF^{SB}_{02D} of building (0.64 Hz) as compared to the SVF^{S}_{02D} of standalone building on rock (0.66 Hz). There is no splitting of the spectral bandwidth of the fundamental mode of vibration of building.

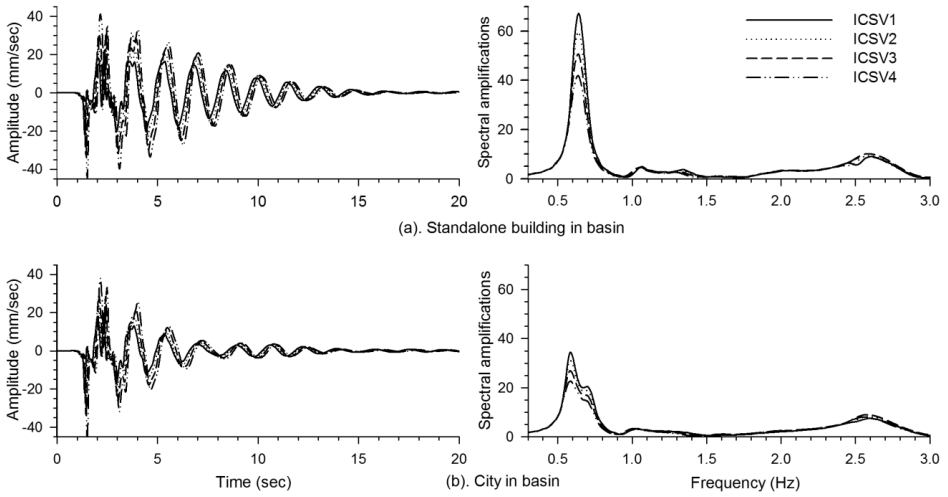

Fig. 7a-b. A comparison of the SV-wave responses (left) and spectral amplifications (right) at the top of standalone building on the exposed rock, at the top of a standalone building at the centre of basin and at the top of a building situated at the centre of ICSV1–ICSV4 site-city models, respectively.

6.2. SCI effects on building response

The left panel of Fig. 7b shows the SV-wave responses at the top of 5^{th} building of the ICSV1–ICSV4 site-city models. Fig. 7b revealed a decrease of amplitude and duration of the SV-wave at the top of building with an increase of IC. In contrast to this, the right panel of Fig. 7b showed that the SAFs at the top of building were increasing with the increase of IC. The

interaction of city with basin has further reduced the SVF_{02D}^{SB} of building to 0.58 Hz, but, this reduction was not affected by the change of IC. The obtained SAF at SVF_{02D}^{SB} of 5$^{\text{th}}$ building as 34.41, 31.02, 26.90 and 22.65 in the ICSV1–ICSV4 site-city models, respectively were 48.84%, 48.03%, 46.84% and 45.43% lesser than those obtained in the respective case of the standalone building (Table 4).

On the other hand, the observed reduction of SAF at SVF_{02D}^{S} of building as 67.41%, 65.29%, 62.48% and 59.31% in the ICSV1–ICSV4 site-city models, respectively revealed that reduction of SAF at SVF_{02D}^{S} was larger than that at SVF_{02D}^{SB} (Table 4). There was also an increase of % reduction in ASA in the horizontal component of SV-wave response of 5$^{\text{th}}$ building with an increase of IC as compared to that in the case of standalone building. So, it may be inferred that the role of IC in the SCI effects on the building response is considerable but not on the reduction of SVF_{02D}^{SB} of buildings.

The left and right panels of Fig. 8a-d depict a comparison of the SV-wave responses and SAFs at the top of 5$^{\text{th}}$, 7$^{\text{th}}$ and 9$^{\text{th}}$ buildings of the ICSV1–ICSV4 site-city models, respectively. A decrease of the SV-wave amplitude and duration at the top of buildings towards the edge of city can be inferred. A decrease of SAFs at the top of building with the decrease of impedance in rock as well as towards the edge of city can be seen in the right panels of Fig. 8a-d. Fig. 8 also showed a decrease of SAF at frequency SVF_{02D}^{SB} towards the edge of city, but this decrease was very large in the case of 9$^{\text{th}}$ building. This may be due to decrease of SAF at towards the edge (*Bard and Bouchon, 1985; Kumar and Narayan, 2018*).

6.3. SCI effects on basin response

The SV-wave responses of the ICSV1–ICSV4 site-city models for without and with city in basin were computed on the horizontal array in between the buildings to quantify the role of IC in SCI effects on the SV-wave response of basin. A considerable decrease in the SV-wave response of basin was inferred due to the presence of city (result not shown here). Fig. 9a-d depicts the comparison of SAFs of the horizontal component of the SV-wave for without and with city in the basin at a distance of 36 m (left panel), 108 m (middle panel), and 252 m (right panel) from the centre of basin for the ICSV1–ICSV4 site-city models, respectively. The analysis of Fig. 9 revealed that

in the absence of city, the deep elliptical basin was vibrating with a single fundamental frequency and the amplification at this frequency was largest at the centre of basin and reduced to one towards the edge of basin, as was observed in the case of SH-wave responses (*Bard and Bouchon, 1985; Kumar and Narayan, 2018*).

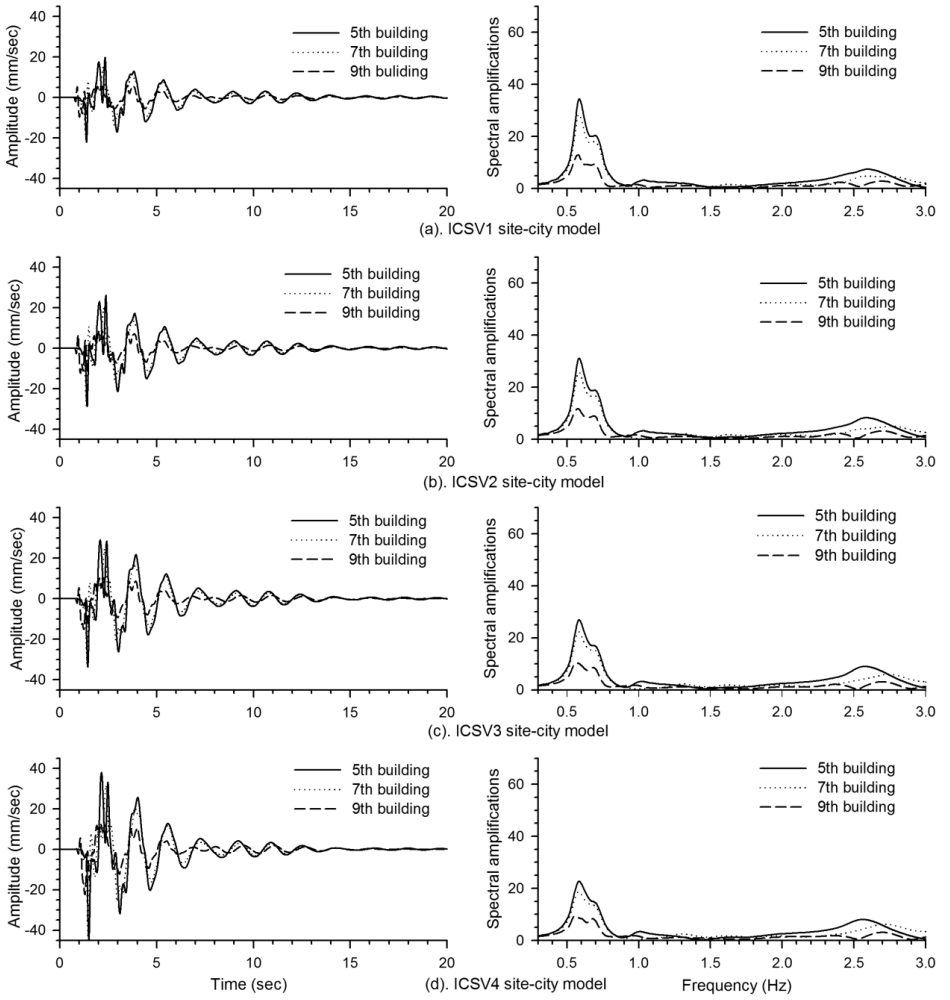

Fig. 8a-d. A comparison of the SV-wave responses (left) and spectral amplifications (right) at the top of different buildings of the ICSV1–ICSV4 site-city models, respectively.

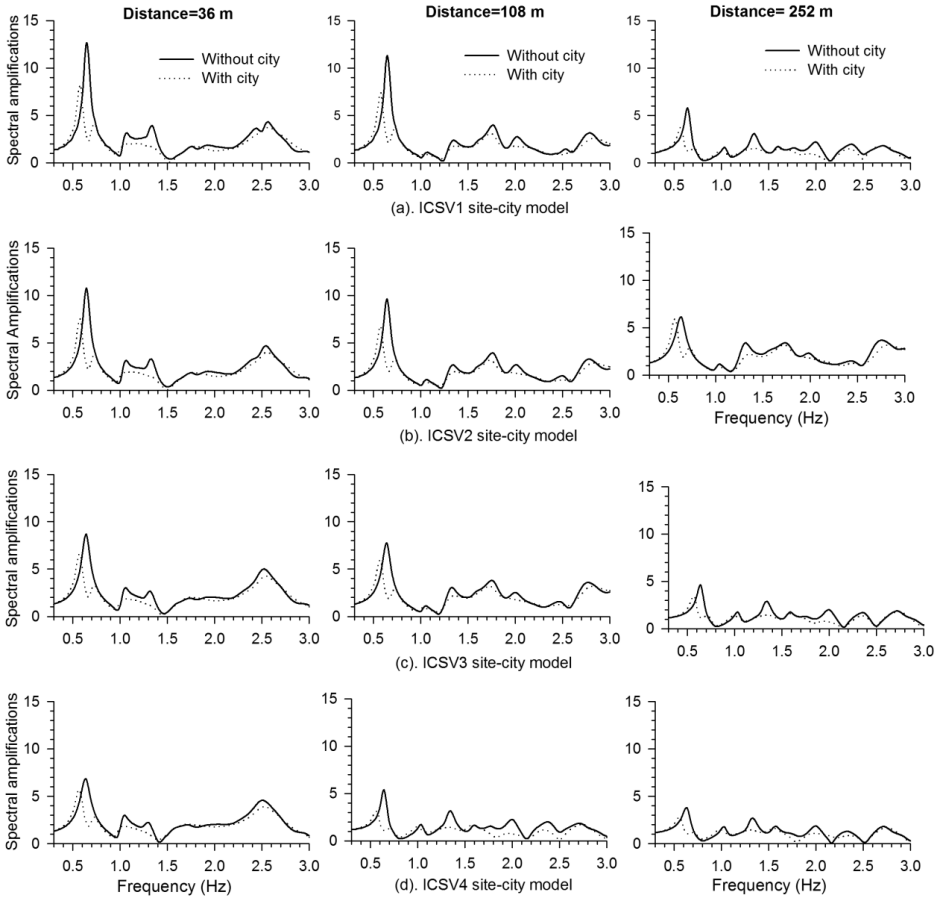

Fig. 9a-d. A comparison of spectral amplifications of free field motion at different locations in the absence and presence of city in the ICSV1–ICSV4 site-city models, respectively.

Minor increase of SVF^{B}_{02D} of basin with an increase of IC in the absence of city can be inferred (*Zhu et al., 2019*). However, the interaction of city with the basin has reduced the SVF^{B}_{02D} of basin to around 0.58 Hz in all the IC model. This reduction of SVF^{B}_{02D} of basin due to SCI was for the entire elliptical basin and was not limited to the area covered by the city. It was interesting to note that the fundamental frequency of buildings and the basin were matching, even after interaction. Table 5 depicts that SCI has caused a

reduction of SAF at SVF^{B}_{02D} of basin of the order of 39.23%, 30.85%, 25.43% and 20.08% in the ICSV1–ICSV4 site-city models, respectively, at a distance of 36 m. But, the obtained % reduction of SAF at frequency SVF^{S}_{02D} as 79.83%, 75.99%, 70.49% and 66.67% in the ICSV1–ICSV4 site-city models, respectively, reveals that the % reduction of SAF at SVF^{S}_{02D} is larger than that at SVF^{SB}_{02D}. Table 5 also revealed an increase of % reduction of ASA in the free field motion with an increase of IC. The SCI effect on the free field motion was largest at the centre of city and decreasing towards the edge of city.

7. Discussion and conclusions

The analysis of simulated SH- and SV-wave responses of the various considered site-city models revealed that the obtained reduction of F^{SB}_{02D} of building, F^{B}_{02D} of basin, corresponding SAFs as well as splitting of bandwidth of fundamental mode of vibrations of both the basin and buildings corroborate with the findings in the past SCI studies (*Guéguen and Bard, 2005; Kham et al., 2006; Semblat et al., 2008; Kumar and Narayan, 2018*). The observed splitting of fundamental mode of vibrations of both the buildings and basin is due to an additional drop of SAF at F^{S}_{02D} of building on rock since the emanated seismic waves by the buildings at this frequency were out of phase to that of the incident S-wave (*Jennings, 1970; Kanamori et al., 1991*). The obtained larger % reduction of SHF^{B}_{02D} of basin and corresponding SAF in the case of SH-wave responses, even though the number of buildings were lesser, may be due to larger height of B16-building as compared to B12-building used in the SV-wave simulations or due to buildings behaving as a shear beam for the SH-wave or may be due to both. The increase of F^{B}_{02D} of basin with an increase of IC in the absence of city corroborates with the finding of *Zhu et al. (2019)*. It was appealing to note that reduction of F^{SB}_{02D} of building and F^{B}_{02D} of basin due to SCI effects were unaffected by the increase of IC for both the polarizations of S-wave. The drastic increase of SCI effects on the responses of basin but only minor increase on response of building were obtained with an increase of IC for both the polarizations of S-wave. Although, the % reduction of SAF at SVF^{B}_{02D} of basin was lesser than that at SHF^{B}_{02D}, but, the role of IC in the SCI effects on the responses of buildings and basin was lager in the case of SV-wave responses.

Acknowledgements. The second and third authors of this paper are thankful to Indian Institute of Technology Roorkee, India for providing MHRD scholarship during M.Tech. Programme.

References

Bard P.-Y., Bouchon M., 1985: The two-dimensional resonance of sediment-filled valleys. Bull. Seismol. Soc. Am., **75**, 2, 519–541.

Bard P.-Y., Chazelas J. L., Guéguen Ph., Kham M., Semblat J. F., 2005: Site-City Interaction. Chapter 5 of the book "Oliveira C. S., Roca A., Goula X. (Eds.): Assessing and Managing Earthquake Risk (Geo-Scientific and Engineering Knowledge for Earthquake Risk Mitigation: Developments, Tools and Techniques)", Springer (new book series on Geotechnical, Geological and Earthquake Engineering). Hardcover ISBN 1-4020-3524-1, 91–114.

Bard P.-Y., Chazelas J. L., Guéguen Ph., Kham M., Semblat J. F., 2008: Site-City Interaction. In: Oliveira C. S., Roca A., Goula X. (Eds.): Assessing and Managing Earthquake Risk. Springer, The Netherlands, 91-114, doi: 10.1007/978-1-4020-3608-8_5.

Chávez-García F. J., Bard P.-Y., 1994: Site effects in Mexico City eight years after the September 1985 Michoacan earthquakes. Soil Dyn. Earthq. Eng., **13**, 4, 229–247, doi: 10.1016/0267-7261(94)90028-0.

Emmerich H., Korn M., 1987: Incorporation of attenuation into time-domain computations of seismic wave fields. Geophysics, **52**, 9, 1252–1264, doi: 10.1190/1.1442386.

Groby J.-P., Wirgin A., 2008: Seismic motion in urban site consisting of blocks in welded contact with a soft layer overlying a hard half-space. Geophys. J. Int., **172**, 2, 725–758, doi: 10.1111/j.1365-246X.2007.03678.x.

Guéguen P., Bard P.-Y., Chávez-García F. J., 2002: Site-City Interaction in Mexico City-Like environments: An Analytical Study. Bull. Seismol. Soc. Am., **92**, 2, 794–811, doi: 10.1785/0120000306.

Guéguen P., Bard P.-Y., 2005: Soil-structure and soil-structure-soil interaction: experimental evidence at the Volvi test site. J. Earthq. Eng., **9**, 5, 657–693, doi: 10.1080/13632460509350561.

Guéguen P., Colombi A., 2016: Experimental and numerical evidence of the clustering effect of structures on their response during an earthquake: A case study of three identical towers in the city of Grenoble, France. Bull. Seismol. Soc. Am., **106**, 6, 2855–2864, doi: 10.1785/0120160057.

Guéguen P., Mercerat E. D., Singaucho J. C., Aubert C., Barros J. G., Bonilla L. F., Cripstyani M. P., Douste-Bacqué I., Langlaude P., Mercier S., Pacheco D. A., Pernoud M., Perrault M., Pondaven I., Wolyniec D., 2019: METACity-Quito: A Semi-Dense Urban Seismic Network Deployed to Analyze the Concept of Metamaterial for the Future Design of Seismic-Proof Cities. Seismol. Res. Lett., **90**, 6, 2318–2326, doi: 10.1785/0220190044.

Merritt R. G., Housner G. W., 1954: Effect of foundation compliance on earthquake stresses in multi-story buildings. Bull. Seismol. Soc. Am., **44**, 4, 551–569.

Israeli M., Orszag S. A., 1981: Approximation of radiation boundary conditions. J. Comput. Phys., **41**, 1, 115–135, doi: 10.1016/0021-9991(81)90082-6.

IS 1893-1, 2002: Criteria for earthquake resistant design of structures – Part 1: General provision and buildings. Bureau of Indian Standards, https://law.resource.org/pub/in/bis/S03/is.1893.1.2002.pdf.

Jennings P. C., 1970: Distant motion from a building vibration test. Bull. Seismol. Soc. Am., **60**, 6, 2037–2043.

Kanamori H., Mori J., Anderson D. L., Heaton T. H., 1991: Seismic excitation by the space shuttle Columbia. Nature, **349**, 6312, 781–782, doi: 10.1038/349781a0.

Kham M., Semblat J.-F., Bard P.-Y., Dangla P., 2006: Seismic site–city interaction: main governing phenomena through simplified numerical models. Bull. Seismol. Soc. Am., **96**, 5, 1934–1951, doi: 10.1785/0120050143.

Kristek J., Moczo P., 2003: Seismic wave propagation in viscoelastic media with material disconuties- a 3 D 4th order staggered grid finite difference modeling. Bull. Seismol. Soc. Am., **93**, 5, 2273–2280, doi: 10.1785/0120030023.

Kumar S., Narayan J. P., 2008: Absorbing boundary conditions in a fourth-order accurate SH-wave staggered grid finite difference algorithm. Acta Geophys., **56**, 4, 1090–1108, doi: 10.2478/s11600-008-0043-9.

Kumar N., Narayan J. P., 2018: Quantification of site-city-interaction effects on the response of structure under double resonance condition. Geophys. J. Int., **212**, 1, 422–441, doi: 10.1093/gji/ggx397.

Kumar N., Narayan J. P., 2019: Effects of site–city interaction and polarisation of the incident S-wave on the transfer function and fundamental frequency of structures. Nat. Hazards, **97**, 2, 747–774, doi: 10.1007/s11069-019-03671-8.

Michel C., Guéguen P., 2018: Interpretation of the velocity measured in buildings by seismic interferometry based on Timoshenko beam theory under weak and moderate motion. Soil Dyn. Earthq. Eng., **104**, 131–142, doi: 10.1016/j.soildyn.2017.09.031.

Narayan J. P., 2005: Study of basin-edge effects on the ground motion characteristics using 2.5-D modeling. Pure Appl. Geophys., **162**, 2, 273–289, doi: 10.1007/s00024-004-2600-8.

Narayan J. P., Kumar V., 2013: A fourth-order accurate finite-difference program for the simulation of SH-wave propagation in heterogeneous viscoelastic medium. Geofizika, **30**, 2, 173–189.

Narayan J. P., Kumar V., 2014: Study of combined effects of sediment rheology and basement focusing in an unbounded viscoelastic medium using P-SV-wave finite-difference modelling. Acta Geophys., **62**, 6, 1214–1245, doi: 10.2478/s11600-013-0199-9.

Sahar D., Narayan J. P., Kumar N., 2015: Study of role of basin shape in the site–city interaction effects on the ground motion characteristics. Nat. Hazards, **75**, 2, 1167–1186, doi: 10.1007/s11069-014-1366-2.

Sahar D., Narayan J. P., 2016: Quantification of modification of ground motion due to urbanization in a 3D basin using viscoelastic finite difference modeling. Nat. Hazards, **81**, 2, 779–806, doi: 10.1007/s11069-015-2105-z.

Schwan L., Boutin C., Padron L. A., Dietz M. S., Bard P.-Y., Taylor C., 2016: Site-city interaction: theoretical, numerical and experimental crossed-analysis. Geophys. J. Int., **205**, 2, 1006–1031, doi: 10.1093/gji/ggw049.

Semblat J.-F., Kham M., Bard P.-Y., 2008: Seismic-wave propagation in alluvial basins and influence of site-city interaction. Bull. Seismol. Soc. Am., **98**, 6, 2665–2678, doi: 10.1785/0120080093.

Stewart J. P., Seed R. B., Fenves G. L., 1999: Seismic soil-structure interaction in buildings. II: Empirical findings. J. Geotech. Geoenviron. Eng., **125**, 1, 38–48, doi: 10.1061/(ASCE)1090-0241(1999)125:1(38).

Tsogka C., Wirgin A., 2003: Simulation of seismic response in an idealized city. Soil Dyn. Earthq. Eng., **23**, 5, 391–402, doi: 10.1016/S0267-7261(03)00017-4.

Wirgin A., Bard P.-Y., 1996: Effects of building on the duration and amplitude of ground motion in Mexico City. Bull. Seismol. Soc. Am., **86**, 3, 914–920.

Wong H. L., Trifunac M. D., 1975: Two-dimensional anti-plane building-soil-building interaction for two or more buildings and for incident plane SH waves. Bull. Seismol. Soc. Am., **65**, 6, 1863–1885.

Zeng C., Xia J., Miller R. D., Tsoflias G. P., 2012: An improved vacuum formulation for 2D finite-difference modeling of Rayleigh waves including surface topography and internal discontinuities. Geophysics, **77**, 1, T1–T9, doi: 10.1190/geo2011-0067.1.

Zhu C., Thambiratnam D., Gallage C., 2019: Inherent characteristics of 2D alluvial formations subjected to in-plane motion. J. Earthq. Eng., **23**, 9, 1512–1530, doi: 10.1080/13632469.2017.1387199.